Magnetless Nonreciprocity in Optically Pumped and Strained Graphene

By

XU HAN

DISSERTATION

Submitted in partial satisfaction of the requirements for the degree of

DOCTOR OF PHILOSOPHY

in

Electrical and Computer Engineering

in the

OFFICE OF GRADUATE STUDIES

of the

UNIVERSITY OF CALIFORNIA

DAVIS

Approved:

Juan Sebastian Gomez-Diaz

Joshua Hihath

William Putnam

Committee in Charge

2024

Acknowledge

As my years of graduate life are about to conclude, I am profoundly moved when I reflect on the dedication, achievements, challenges, and successes, as well as the sorrows and joys I've experienced. Five years ago, I entered UC Davis with dreams for the future and expectations for myself. During these years, I've gained much, and now as this chapter closes, I am ready to embark on a new journey in life without any regrets. Along the way, my teachers, co-worker and friends have provided me with immense care and support. It is because of you all that these years have been so enriching and educational, not only helping me to understand the world better but also leaving me with the most beautiful memories of my life.

First, I want to express my gratitude to UC Davis. Over the past five years, I have had the privilege of experiencing the university's spirit of intellectual freedom and inclusiveness. It is this spirit that has enabled me to understand myself and the world, to clarify who I want to become, and to understand how to strive for my ideals. If these years were not spent at UC Davis but elsewhere, I couldn’t have gained as much.

As a PhD student under the guidance of Professor Juan Sebastian Gomez-Diaz, I have experienced firsthand and tremendous impact of his mentoring. From the moment I joined his group, he has consistently gone above and beyond to provide guidance, support, and invaluable insights. His mentorship extends beyond the academic realm, as he genuinely cares about my professional development. He takes the time to understand our individual aspirations and tailors his advice accordingly.

What truly sets Professor Gomez-Diaz apart is his ability to foster a nurturing and inclusive environment. He creates a space where students feel comfortable to voice their opinions, ask

questions, and engage in thoughtful discussions. He encourages us to challenge ourselves, pushing us to reach our full potential while offering support along the way.

I would also like to thank my master's supervisor, Professor Zhaoyu Zhang. You have provided me with full support and assistance in both academics and life, teaching me not only scientific methods of work but also how to identify, analyze, and solve problems. You have also greatly fostered my abilities in teamwork, leadership, and time management—qualities extremely crucial for my future. Your broad research vision, profound theoretical knowledge, rigorous academic attitude, and noble character have been both instructive and beneficial to me, offering lasting support for my future life.

I also want to thank Dr. Nayan Kumar Paul, who is a year ahead in my group. When I first arrived in Davis, unsure of the future, he guided me through life and study. During the first year, we were roommate and whenever I faced setbacks in my studies and life, he encouraged me. Whenever I reach out to him for assistance, he was always there willing to share his valuable knowledge and insights. I really appreciate that he provided me with his understanding and perspective of the society as an international student. The conversations we had equipped me with a more multidimensional and pragmatic attitude towards life and the future.

Last but not the least, I want to express my deepest gratitude to my parents. They raised and taught me, allowing me to become a good person. Thank you for the unconditional support, especially during the hard time of the pandemic.

Abstract

Breaking reciprocity lies in the heart of modern electromagnetic devices such as circulators, isolators, filters, and antennas. Generally, breaking reciprocity can be realized by biasing the device with a physical quantity that is odd symmetric under time-reversal. Conventionally, such response has been achieved by magnetically biasing ferromagnetic compounds and garnets. In the past decade, magnetless approaches based on nonlinear responses, spatiotemporal modulation, drifting electrons, and opto-mechanical effects have been explored across the electromagnetic spectrum. Recently, circular dichroism has been demonstrated to be an efficient tool to break reciprocity in 2D materials due to the optically-driven non-degenerate valleys.

In this thesis, I propose a novel method to break reciprocity in 2D materials based on the use of circularly polarized light and strain engineering. To this purpose, I review and calculate the optical conductivity of graphene under uniform strain and discussed the impact of non-uniform strain on graphene. The results show a close resemblance between pseudomagnetic field and the effect of non-uniform strain. The utilization of non-uniform strain gives rise to energy level quantization in graphene and thus provides easily addressable optical transition between discrete energy levels using optical pump. I review the formalism and algorithm of a rigorous theoretical framework able to deal with Bloch equations regarding the population of different energy levels. The incorporation of some scattering mechanisms also closely reproduces what happens to the carrier population in picosecond time scale after the presence of an optical pump. The results show the population imbalance in the two non-degenerate valleys in graphene which indicates the broken reciprocity. This approach of breaking reciprocity unleashes large non-reciprocal response in graphene using magnetless implementations.

In a related context, the field of plasmonics has opened new possibilities to control and manipulate light beyond the diffraction limit and has enabled countless applications in areas such as sensing, spectroscopy, and healthcare. The emerge of ultrathin metasurfaces and 2D materials have provided new knobs to excite, process, and route SPPs, while also enabling unexpected possibilities to manipulate and enhance nonreciprocal responses. Unfortunately, the design of quasi-optimal nonreciprocal metasurfaces is usually quite challenging and require significant computational resources.

This thesis unveils the fundamental limits of linear and nonreciprocal plasmonic metasurfaces in terms of isolation and loss. The proposed bounds are related to surface waves and only depend on the nonreciprocal material employed within the metasurface, thus being independent of geometrical considerations and the presence of other materials. We apply these fundamental limits to explore two different platforms, namely drift-biased and magnetically-biased graphene metasurfaces. For each platform, we first analytically derive the upper bounds in terms of graphene conductivity. Then, we explore devices proposed in the literature and benchmark their response against their upper bounds. Results highlight that drift-biased hyperbolic metasurfaces exhibit outstanding performance in the mid-infrared region, whereas magnetically-biased devices are better suited for the low terahertz band. More broadly, our bounds allow to quickly assess the performance of nonreciprocal plasmonic metasurfaces with respect to their fundamental limit, thus streamlining the device design process and preventing that significant efforts are dedicated to marginal performance improvements. The proposed bounds pave the way toward the development of quasi-optimal nonreciprocal metasurfaces, with important applications in sensing, imaging, communications, and nonlinear optics, among many others.

Contents

1. Introduction 1

1.1 Breaking electromagnetic reciprocity 1

1.2 Optical pump & strain engineering in 2D materials 5

1.3 Fundamental limits of nonreciprocal plasmonics 7

1.4 Scope of this thesis 9

1.5 Chapter references 11

2. Optically-pumped gapped 2D materials 22

2.1 Graphene and 2D materials 23

2.1.1 Hamiltonian 24

2.1.2 Kubo formalism and optical conductivity 28

2.1.3 Magnetic-biased graphene 34

2.2 Negative dynamic conductivity 39

2.3 Light-induced Faraday rotation 41

2.3.1. Valley-dependent optical selection 42

2.3.2 Quantum Liouville's theorem 44

2.3.3 Berry curvature and Faraday rotation. 47

2.4 Graphene devices 50

2.5 Conclusions and future work 53

2.5.1 Future work: Theory 54

2.5.2 Future work: Experiments 56
2.6 Chapter references 59
3. Graphene in strain fields 67
3.1 Introduction 67
3.2 Graphene in uniform strain fields 68
3.2.1 Lattice distortion 68
3.2.2 Optical conductivity of uniformly strained graphene 71
3.3 Graphene in non-uniform strain 74
3.3.1 Strain-induced pseudomagnetic fields 75
3.3.2 Electronic band structure of graphene under non-uniform strain 82
3.4 Exploiting pseudo-magnetic fields with low-B 84
3.5 Conclusions and future work 86
3.6 Chapter references 87
4. Optically pumped strained graphene 90
4.1 Tight-binding model for Landau-quantized graphene 91
4.2 Optical matrix element 95
4.3 Optical pump 97
4.4 Light-carrier interactions 103
4.5 Rabi oscillations in the Rotating Wave Approximation (RWA) 104
4.6 The initial states 109

4.7 Carrier-carrier scattering 111

4.7.1 Coulomb screening 113

4.7.2 Scattering rates 116

4.8 Numerical investigation of microscopic Bloch equations 119

4.8.1 Bloch equations without dephasing and damping 119

4.8.2 Bloch equations with finite dephasing 122

4.8.3 Bloch equations with carrier-carrier scattering 124

4.9 Chapter conclusions 127

4.9 Chapter references 128

5. Fundamental limits of nonreciprocal plasmonic metasurfaces 130

5.1 Isolation inequality 131

5.2 Application to drift-biased graphene plasmonics 134

5.4 Application to magnetically-baised graphene plasmonics 143

5.5 Conclusions 146

5.6 Chapter references 147

6. Conclusions 153

Chapter references 155

1. Introduction

1.1 Breaking electromagnetic reciprocity

The propagation of electromagnetic (EM) waves, from radio frequencies to the visible, is governed by the Lorentz reciprocity theorem based on the invariance of Maxwell's equations under time-reversal. It dictates that if EM waves can travel from point A to point B, they can also travel from point B to point A with the same properties [1]. This law prohibits nonreciprocal propagation of EM waves in linear platforms, which in turn limits various possibilities to manipulating waves hence the functionality of numerous photonic devices. For instance, breaking reciprocity allows transmitting a signal without worrying about the interference with incoming signals or back reflections. Therefore, breaking reciprocity has been lying in the heart of modern photonic devices such as circulators [2]-[5], isolators [6]-[8], filters [9], [10], and antennas [11]-[13].

For decades, there has been tremendous efforts seeking ways to break reciprocity in the propagation of EM waves. Generally, breaking reciprocity can be realized by biasing the transmission channel with a physical quantity that is odd-symmetric under time-reversal [1]. The most common approach in such a scheme is based on magneto-optical phenomena by magnetically biasing ferromagnetic compounds and garnets [14], [15]. Although this method is effective in several scenarios, it has important disadvantages because such systems tend to be bulky, lossy, and incompatible with integrated circuits due to the lattice mismatch between ferrite crystals and most semiconductor materials [1]. Another drawback lies in the fact that magneto-optical phenomena fade at higher frequencies, making it less effective in photonic technologies [16]. Those issues hence trigger the interests in magnetless nonreciprocity, i.e., nonreciprocity with no magnets nor ferromagnetic materials. This is why alternative approaches such as nonlinearity [17]-[19],

optomechanical interactions [20]-[21], and spatiotemporal modulation [22]-[27] have attracted enormous attention in the last decades. Among these approaches, nonlinearity is potentially useful and has been extensively studied in optical applications [28], [29]. However, it can only be employed under certain power levels and in devices excited only through one port at a time, hence exhibits limited possibilities in those scenarios when the linearity of the signals is required, such as RF [30] and full-duplex communications [31]. Although passive, bias-free nonreciprocal devices based on $\chi^{(3)}$ nonlinearity may overcome the power range constraints, however they are mostly restricted to pulsed and periodic source applications due to the restrictions imposed by dynamic reciprocity on passive nonlinear devices [32], [33]. Nonreciprocal responses provided by opto-mechanical resonators are complex to implement, somewhat narrowband, and relatively weak [34], [35]. The latter approach, spatiotemporal modulation, is very well suited for RF and microwave frequencies [36], [37]. However, as frequency increases toward the terahertz (THz) and far-infrared (IR) bands, it requires hundreds of gating pads to impart high modulation frequencies able to impart linear or angular momentum to the devices, thus demanding very complicated fabrication process and feeding networks [38], [39]. In addition, as frequency further increases, the challenges to modify the properties of materials operating with enough speed also increase [22].

In a related context, graphene has emerged as an promising candidate to manipulate THz and IR plasmonics, enabling graphene-based nanophotonic devices with unusual properties of strong field confinement, relatively low propagation loss, high mobility, and reconfigurability through a gate bias [40], [41], [42]. The tunable plasmons supported by graphene at THz have indeed shined light on the so-called THz gap because for a long time there has been a lack of practical technologies to generate, manipulate, and detect THz radiation [43]. Such characteristics have

trigger new venues to develop THz and IR sources, components, and detectors based on graphene plasmonics [44], [45]. Additionally, there has been an increasing interest to manipulate and boost the graphene electromagnetic behavior by enforcing the interaction of this 2D material with external agents such as magnetic fields, optical pumps, and mechanical strain [40]. From a more theoretical perspective, the electromagnetic response of graphene has usually been modelled by applying the Kubo formalism [46]. Briefly, the Kubo formula accounts for all possible electron transitions and contributions in the electronic momentum space that will give rise to the electromagnetic conductivity. This formalism brings a powerful link between microscopy (i.e., electrons behavior in graphene, modelled through quantum mechanics) and macroscopy (i.e., electric conductivity tensor employed in Maxwell's equations) worlds, provided that accurate Hamiltonian are available to describe graphene perturbated with external fields.

The very first application of graphene to break electromagnetic reciprocity occurred in 2011, when Faraday rotation (FR) at THz was experimentally demonstrated in magnetically-biased graphene [47], [51]-[53]. Faraday rotation is one of the most important phenomena arising from breaking time–reversal symmetry (TRS). It is the nonreciprocal rotation of EM waves' polarization after passing through a media. The media is commonly subjected to a magnetic field along the direction of light propagation, which causes a polarization rotation of the propagating waves. The rotation handedness flips sign when changing direction of propagation and thus can be utilized in optical isolation. Faraday rotation in graphene was enhanced soon after by nanopatterning the material [53]-[55]. The reason for such studies being so important is that graphene is the thinnest material ever to show Faraday rotation. The record high angle exceeding 0.1 rad ($\sim 6^{\circ}$) was achieved in single layer graphene in lab environment with magnetic field of 7 T [47]. Graphene's strong nonreciprocal responses under magnetic bias appears due to the cyclotron effect and inter-

Landau level transitions, and it is a very promising building block for the development of magneto-optical devices [47]. Despite such promising response, it still requires large magnetic field which is not practical without sophisticate lab setups.

Electromagnetic nonreciprocity based on spatio-temporal modulation can be implemented using 2D materials at terahertz and infrared frequencies by modulating their conductivity in space and time. To this purpose, a single graphene layer can be loaded with various gating pads underneath. The pads are biased with time-dependent voltages with different phases. Spatio-temporally modulated graphene has been proposed to enable a large number of nonreciprocal electromagnetic functionalities and devices, ranging from plasmonic isolators and leaky-wave antennas [60] to nanophotonic devices based on different types of photonic transitions [61]. The main challenge of this technology relies on its somewhat complex configuration, as it requires the patterning of many pads that should be biased and independently controlled. Even though edge effects close to the pads are expected to have a small influence [62], fabrication challenges have hindered the development of this approach in practice.

Despite these advances, there is still a clear need to achieve nonreciprocal responses at terahertz and infrared frequencies without relying on magnetic fields. This thesis explores different approaches base on 2D materials, with emphasis on optical pumping and strain engineering, to meet this technological challenge. Another scope of this thesis is to explore the fundamental limit that can be achieved in practice using nonreciprocal devices. Specifically, we noticed that while the fundamental limit of nonreciprocal components operating in the far-field has been clearly determined [63],[64], this limit remains unsolved for plasmonics. This thesis will set up a metric for evaluating plasmonic nonreciprocal metasurfaces in the near field, which will help benchmark the isolation and loss performance of such devices.

1.2 Optical pump & strain engineering in 2D materials

Circularly polarized (CP) optical pumps have provided an alternative venue to induce Hall conductivity in gapped graphene and other 2D materials [71]-[74], and thus to break TRS. 2D materials such as gapped graphene and transition metal dichalcogenides (TMDs) −which lack inversion symmetry− have opposite Berry curvature in their two valleys ensured by TRS [40], [75], [76]. In such systems, TRS also imposes the spin splitting to have different sign on these valleys [77]-[78], leading to valley-dependent optical selection rules, in which RHCP light couples to interband transitions in one valley, and LHCP light couples to the other one. This all-optical approach can give rise to valley-Hall conductivity in the absence of external magnetic field. The light-induced Hall effect has already been observed in graphene at DC [79] and somewhat weak all-optical nonreciprocity have been demonstrated in TMDs at visible [80]. Additionally, several studies have suggested that amplification (i.e., optical gain) at THz and IR frequencies is possible in graphene subjected to linearly polarized laser beams [69], [70]. Such optical amplification effect (optical gain) is due to the interband population inversion arising from optical pumping. With sufficient large pump intensity, the interband transitions may prevail to intraband transitions. This behavior has recently been exploited to manipulate the THz and IR properties of graphene with optical beams [81]. THz wave amplifiers could be disruptive components to contribute closing the terahertz gap. Unfortunately, optical gain using graphene has not yet been demonstrated. In all cases, the main challenge is that very high-power optical beams are required to modify graphene's properties without leading to optical damage, which is not realistic in practical applications.

Another interesting possibility worth to explore in aid of enhancing nonreciprocal responses in graphene is strain engineering. When a uniform mechanical strain acts on graphene, it does not break the sublattice symmetry but rather shifts the two distinct valleys of graphene in opposite

directions [40],[82]. Such shift is analogous to the momentum shift of graphene under external magnetic fields. The existence of pseudomagnetic field in graphene has been demonstrated to have a bearing on non-uniform strain fields [83],[84]. However, unlike uniform magnetic field acting on graphene in the physical space, pseudomagnetic fields induced by non-uniform strains have opposite sign but same modulus for the two valleys. The combination of these responses cancels out and, as a result, elastic deformations do not violate TRS in graphene [82]-[88]. Similar conclusions can also be drawn for other 2D materials [89]. The experimental demonstration of Landau quantization and pseudo–magnetic fields equivalent to bias fields larger than 300 Teslas in graphene nanobubbles [84] has triggered intense research in this field, aiming to study carriers dynamics in previously inaccessible high magnetic field regimes and to break reciprocity through non-uniform strain engineering.

During the development of this project, a theoretical work appeared suggesting that large Faraday rotation can be obtained by applying small magnetic fields on strained graphene [90]. It shows that by applying a sub-Tesla external magnetic field to uniformly strained graphene, it yields giant FR which is impossible to obtain only by external magnetic field. It points out the role of non-uniform strain as being a huge pseudomagnetic field acting in reciprocal space. This work shows the possibility of lifting the restrictions of using magnetic field to achieve Faraday rotation. It also proposes a practical method to realize scalable uniform pseudomagnetic field in graphene by placing it on periodically nanohole array in dielectric substrate and provides a theory to effectively correlate the dimensions and periodicity of it with the magnitude of the pseudomagnetic field.

In this context, one of the main goals of the thesis is to assess these two mechanisms and merge them to optimize nonreciprocal responses using a magnet-less platform. It is also important

to find a mutual theoretical framework under which both mechanisms can be formulated, evaluated, and combined. This would be very critical for the future development of integrated, nonreciprocal platform based on 2D materials.

1.3 Fundamental limits of nonreciprocal plasmonics

In a related context, the field of plasmonics has opened new possibilities to control and manipulate light beyond the diffraction limit [90] and has enabled countless applications in areas such as sensing, spectroscopy, and healthcare [92]-[94]. Surface plasmon polaritons (SPPs) are electromagnetic modes confined to two-dimensional (2D) interfaces that possess evanescent fields in the direction perpendicular to the interface. For instance, SPPs are supported by dielectric-metal interfaces at infrared (IR) and visible frequencies [95] and by graphene and other 2D materials [96]-[99] in the terahertz (THz) and IR bands. The emerge of ultrathin metasurfaces [100] and 2D materials [101] have provided new knobs to excite, process, and route SPPs, while also enabling unexpected possibilities to manipulate and enhance nonreciprocal responses [102]-[104] Nonreciprocal plasmonics lead to strong light-matter interactions [105], useful in areas as nonlinear wave generation, sensing, and communications, among others. Unfortunately, the design of quasi-optimal nonreciprocal metasurfaces is usually quite challenging and require significant computational resources. Given the abundant choice of materials and large degree of freedoms for geometrical shapes and dimensions, it would be highly desirable to determine the optimal response that can be achieved by a metasurface loaded with a specific nonreciprocal material. This would allow to (i) streamline the design process, by assessing the performance of a given device with respect to the fundamental bounds; and (ii) prevent that significant efforts are dedicated to marginally improve the device performance while leading to unnecessarily complex structures.

The fundamental limits and trade-offs between isolation and loss of a waveguide junction filled with an arbitrary dielectric was derived in the 50s [63]. More specifically, when a two-port network containing a nonreciprocal magnetic material is magnetized by an external field, there are upper bounds only associated with the magnetic material. Such bounds determine a figure of merit (FoM) for the entire device performance, are independent of geometrical considerations and the presence of other materials, and lead to a clear trade-off between isolation and loss. This elegant result is readily applicable to modulators and can easily be extended to nonreciprocal devices working with propagative waves. Based on this work, the fundamental limits of a realistic optical switching device showed that its dynamic performance is only subjected to the tunable material employed within the device [63]. In 2014, this approach was applied to determine the fundamental limits of magnetically-biased graphene-based devices interacting with waves propagating in free-space [64]. Several configurations, including isolators and Kerr rotators, were investigated for random planar device geometries within a large parametric space. It was shown that some specific devices, with tailored nanostructures made of graphene and metals, can reach performances very close to the upper fundamental limits offered by magnetically-biased graphene. To date, fundamental bounds of nonreciprocal devices are limited to *propagative* waves and cannot be applied within the field of plasmonics.

The emerge of vast variety of metasurface structures and nonreciprocal plasmonic devices associated with them have demanded significant computational resources. Therefore, it would be highly desirable to determine the optimal performance of a nonreciprocal plasmonic devices in the near field. As a result, extending the above mentioned FoM for propagative waves to the field of plasmonics is critical and can pave the way to the development of plasmonic nonreciprocal devices with optimal isolation and minimal loss.

1.4 Scope of this thesis

This thesis is divided into two main goals. The first one aims to sets the foundations of a transformative magnetless nonreciprocal paradigm through unexplored approaches that combine optical pumping and strain engineering in 2D materials. The schematic of the proposed approach is shown in Fig. 1.1. To this purpose, Chapter 2 starts with calculating the conductivity of pristine graphene as well as magnetically-biased graphene using Kubo formalism. The vanishing off-diagonal term of the conductivity tensor of pristine graphene indicates its close bound to the unbroken time reversal symmetry. The discussion focuses next on the calculation of the Hall conductivity of optically-pumped gapped Dirac systems, specifically graphene with a fixed energy gap which guarantees a broken inversion symmetry and thus leading to finite Hall conductivity. Then, Chapter 3 discusses the band structure, conductivity and pseudo-magnetic field induced by different kind of strain field, mainly focusing on uniform and non-uniform strain. This chapter concludes with that only non-uniform can generate pseudomagnetic field which would quantize graphene band structure, allowing opposite optical transitions within the two valleys. This would lift the restriction of using gapped graphene to create broken inversion symmetry, which in practice is very difficult to obtain. Finally, Chapter 4 conceptualizes a novel approach to magnetless nonreciprocity by starting with formulating optical pumping, carrier-carrier scattering mechanism under a common density matrix formalism. By assuming pseudomagnetic field with same magnitude but opposite signs induced by some unknown non-uniform strain field, the resulting distinct optical selection rules lead to different carrier dynamics and as a result imbalanced population of same energy levels within the two valleys. The possibility of a transient nonreciprocal response and the feasibility of achieving magnetless nonreciprocity combining optical pump and strain engineering in 2D materials will be discussed.

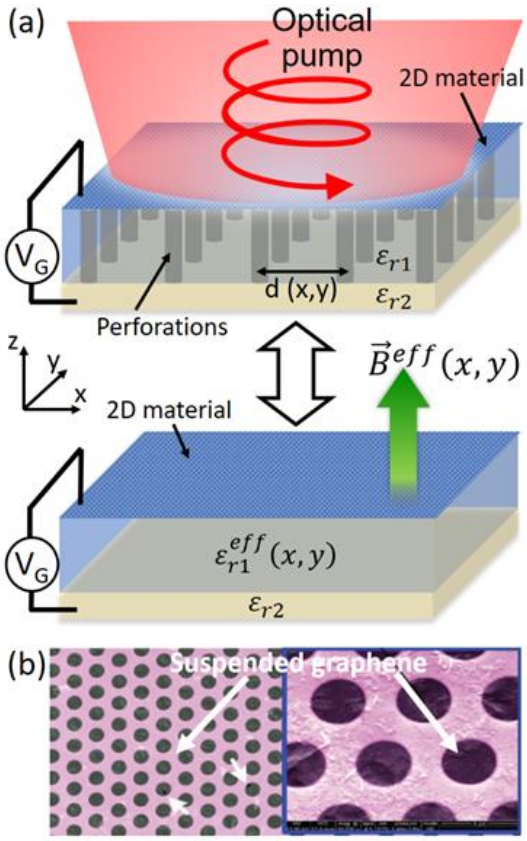

Figure 1.1 Breaking time-reversal symmetry by pumping circularly polarized light to strained 2D materials. (a) Equivalence between the proposed platform and magnetically-biased 2D materials. (b) SEM image of graphene transferred onto a perforated dielectric [106].

The second main goal of this thesis is to unveil the fundamental bounds and trade-offs between isolation and loss of linear, nonreciprocal plasmonic devices. To this purpose, Chapter 5 proposes to define a new metric to evaluate the performance of nonreciprocal plasmonic metasurfaces in terms of isolation and loss. Without loss of generality, we focus on two types of nonreciprocal plasmonic platforms, i.e., drift- and magnetically- biased graphene metasurfaces, and we analytically derived their fundamental bounds. This information is of paramount importance for the development of quasi-optimal nonreciprocal devices. Finally, conclusions and future work are described in Chapter 6.

1.5 Chapter references

[1] Caloz, Christophe, et al. "Electromagnetic nonreciprocity." Physical Review Applied 10.4 (2018): 047001.

[2] Vani, Divya, et al. "Design And Development of A 6-Port Optical Circulator Using Silicon Photonic Crystals." (2021).

[3] Portela, Gianni, et al. "Photonic integrated circulators based on iron garnets without external magnetization." Smart Photonic and Optoelectronic Integrated Circuits XXIII. Vol. 11690. International Society for Optics and Photonics, 2021.

[4] Wang, Zheng, and Shanhui Fan. "Optical circulators in two-dimensional magneto-optical photonic crystals." Optics letters 30.15 (2005): 1989-1991.

[5] Huang, Duanni, et al. "Dynamically reconfigurable integrated optical circulators." Optica 4.1 (2017): 23-30.

[6] Aplet, L. J., and J. Wo Carson. "A Faraday effect optical isolator." Applied Optics 3.4 (1964): 544-545.

[7] Wang, Chen, Xiao-Lan Zhong, and Zhi-Yuan Li. "Linear and passive silicon optical isolator." Scientific reports 2.1 (2012): 1-6.

[8] Kawaguchi, Yuma, et al. "Optical isolator based on chiral light-matter interactions in a ring resonator integrating a dichroic magneto-optical material." Applied Physics Letters 118.24 (2021): 241104.

[9] Wu, X., et al. "Non-reciprocal bandpass filters using time-modulated resonators." IEEE Trans. Microw. Theory Tech (2018).

[10] Alvarez-Melcon, Alejandro, et al. "Coupling matrix representation of nonreciprocal filters based on time-modulated resonators." IEEE Transactions on Microwave Theory and Techniques 67.12 (2019): 4751-4763.

[11] Hadad, Yakir, Jason C. Soric, and Andrea Alu. "Breaking temporal symmetries for emission and absorption." Proceedings of the National Academy of Sciences 113.13 (2016): 3471-3475.

[12] Zang, Joachim Werner, et al. "Nonreciprocal wavefront engineering with time-modulated gradient metasurfaces." Physical Review Applied 11.5 (2019): 054054.

[13] Cheng, Lin, et al. "Superscattering, superabsorption, and nonreciprocity in nonlinear antennas." ACS Photonics 8.2 (2021): 585-591.

[14] Kahn, Frederic J., P. S. Pershan, and J. P. Remeika. "Ultraviolet magneto-optical properties of single-crystal orthoferrites, garnets, and other ferric oxide compounds." Physical review 186.3 (1969): 891.

[15] Adachi, Nobuyasu, et al. "Magneto-optical effect and ferromagnetic resonance of Bi–Fe garnet for high frequency electromagnetic sensor." Journal of Applied Physics 109.7 (2011): 07A506.

[16] Alù, Andrea. "Magnet-Free Nonreciprocity." Proceedings of the IEEE 108.10 (2020): 1682-1683.

[17] Cotrufo, Michele, et al. "Nonlinearity-Induced Nonreciprocity--Part I." IEEE Transactions on Microwave Theory and Techniques (2021).

[18] Soljačić, Marin, et al. "Nonlinear photonic crystal microdevices for optical integration." Optics letters 28.8 (2003): 637-639.

[19] Gallo, Katia, et al. "All-optical diode in a periodically poled lithium niobate waveguide." Applied Physics Letters 79.3 (2001): 314-316.

[20] Fleury, Romain, et al. "Sound isolation and giant linear nonreciprocity in a compact acoustic circulator." Science 343.6170 (2014): 516-519.

[21] Weis, Stefan, et al. "Optomechanically induced transparency." Science 330.6010 (2010): 1520-1523.

[22] Correas-Serrano, Diego, N. K. Paul, and J. Sebastian Gomez-Diaz. "Plasmonic and photonic isolators based on the spatiotemporal modulation of graphene." Micro-and Nanotechnology Sensors, Systems, and Applications XI. Vol. 10982. International Society for Optics and Photonics, 2019.

[23] Correas-Serrano, D., Andrea Alù, and Juan Sebastian Gomez-Diaz. "Magnetic-free nonreciprocal photonic platform based on time-modulated graphene capacitors." Physical Review B 98.16 (2018): 165428.

[24] Yu, Zongfu, and Shanhui Fan. "Complete optical isolation created by indirect interband photonic transitions." Nature photonics 3.2 (2009): 91-94.

[25] Lira, Hugo, et al. "Electrically driven nonreciprocity induced by interband photonic transition on a silicon chip." Physical review letters 109.3 (2012): 033901.

[26] Sounas, Dimitrios L., Christophe Caloz, and Andrea Alu. "Giant non-reciprocity at the subwavelength scale using angular momentum-biased metamaterials." Nature communications 4.1 (2013): 1-7.

[27] Estep, Nicholas A., et al. "Magnetic-free non-reciprocity and isolation based on parametrically modulated coupled-resonator loops." Nature Physics 10.12 (2014): 923-927.

[28] Nazari, F., et al. "Optical isolation via $\mathcal{PT}$-symmetric nonlinear Fano resonances." Optics express 22.8 (2014): 9574-9584.

[29] Zhou, Xin, and Y. D. Chong. "PT symmetry breaking and nonlinear optical isolation in coupled microcavities." Optics express 24.7 (2016): 6916-6930.

[30] Reiskarimian, Negar, and Harish Krishnaswamy. "Magnetic-free non-reciprocity based on staggered commutation." Nature communications 7.1 (2016): 1-10.

[31] Mund, J., et al. "Toroidal nonreciprocity of optical second harmonic generation." Physical Review B 103.18 (2021): L180410.

[32] Yang, Ki Youl, et al. "Inverse-designed non-reciprocal pulse router for chip-based LiDAR." Nature Photonics 14.6 (2020): 369-374.

[33] Shi, Yu, Zongfu Yu, and Shanhui Fan. "Limitations of nonlinear optical isolators due to dynamic reciprocity." Nature photonics 9.6 (2015): 388-392.

[34] Fang, Kejie, et al. "Generalized non-reciprocity in an optomechanical circuit via synthetic magnetism and reservoir engineering." Nature Physics 13.5 (2017): 465-471.

[35] Aspelmeyer, Markus, Tobias J. Kippenberg, and Florian Marquardt. "Cavity optomechanics." Reviews of Modern Physics 86.4 (2014): 1391.

[36] Kord, Ahmed, et al. "CMOS integrated magnetless circulators based on spatiotemporal modulation angular-momentum biasing." IEEE Transactions on Microwave Theory and Techniques 67.7 (2019): 2649-2662.

[37] Alvarez-Melcon, Alejandro, et al. "Coupling matrix representation of nonreciprocal filters based on time-modulated resonators." IEEE Transactions on Microwave Theory and Techniques 67.12 (2019): 4751-4763.

[38] Correas-Serrano, D., Andrea Alù, and Juan Sebastian Gomez-Diaz. "Magnetic-free nonreciprocal photonic platform based on time-modulated graphene capacitors." Physical Review B 98.16 (2018): 165428.

[39] Correas-Serrano, D., et al. "Nonreciprocal graphene devices and antennas based on spatiotemporal modulation." IEEE Antennas and Wireless Propagation Letters 15 (2015): 1529-1532.

[40] Castro Neto, Antonio H., et al. "The electronic properties of graphene." *RvMP* 81.1 (2009): 109-162.

[41] Grigorenko, Alexander N., Marco Polini, and K. S. Novoselov. "Graphene plasmonics." Nature photonics 6.11 (2012): 749-758.

[42] Geim, Andre K., and Konstantin S. Novoselov. "The rise of graphene." Nanoscience and technology: a collection of reviews from nature journals. 2010. 11-19.

[43] Köhler, Rüdeger, et al. "Terahertz semiconductor-heterostructure laser." Nature 417.6885 (2002): 156-159.

[44] Sun, Zhipei, et al. "Graphene mode-locked ultrafast laser." ACS nano 4.2 (2010): 803-810.

[45] Vicarelli, L., et al. "Graphene field-effect transistors as room-temperature terahertz detectors." Nature materials 11.10 (2012): 865-871.

[46] Correas-Serrano, D., et al. "Black phosphorus plasmonics: anisotropic elliptical propagation and nonlocality-induced canalization." Journal of Optics 18.10 (2016): 104006.

[47] Crassee, Iris, et al. "Giant Faraday rotation in single-and multilayer graphene." Nature Physics 7.1 (2011): 48-51.

[48] Schaibley, John R., et al. "Valleytronics in 2D materials." Nature Reviews Materials 1.11 (2016): 1-15.

[49] Xiao, Di, et al. "Coupled spin and valley physics in monolayers of MoS 2 and other group-VI dichalcogenides." Physical review letters 108.19 (2012): 196802.

[50] Si, Chen, Zhimei Sun, and Feng Liu. "Strain engineering of graphene: a review." Nanoscale 8.6 (2016): 3207-3217.

[51] Sounas, D. L., et al. "Faraday rotation in magnetically biased graphene at microwave frequencies." Applied Physics Letters 102.19 (2013): 191901.

[52] Tamagnone, Michele, et al. "Near optimal graphene terahertz non-reciprocal isolator." Nature communications 7.1 (2016): 1-6.

[53] Poumirol, Jean-Marie, et al. "Electrically controlled terahertz magneto-optical phenomena in continuous and patterned graphene." Nature communications 8.1 (2017): 1-6.

[54] Fallahi, Arya, and Julien Perruisseau-Carrier. "Manipulation of giant Faraday rotation in graphene metasurfaces." Applied Physics Letters 101.23 (2012): 231605.

[55] Crassee, Iris, et al. "Intrinsic terahertz plasmons and magnetoplasmons in large scale monolayer graphene." Nano letters 12.5 (2012): 2470-2474.

[56] Ryzhii, Victor, M. Ryzhii, and Taiichi Otsuji. "Negative dynamic conductivity of graphene with optical pumping." *Journal of Applied Physics* 101.8 (2007).

[57] Dubinov, Alexander A., et al. "Terahertz surface plasmons in optically pumped graphene structures." *Journal of Physics: Condensed Matter* 23.14 (2011): 145302.

[58] Chen, P. Y., et al. "Infrared beam-steering using acoustically modulated surface plasmons over a graphene monolayer." *Journal of Optics* 16.9 (2014): 094008.

[59] Neto, AH Castro, et al. "The electronic properties of graphene." *Reviews of modern physics* 81.1 (2009): 109.

[60] Correas-Serrano, D., et al. "Nonreciprocal graphene devices and antennas based on spatiotemporal modulation." *IEEE Antennas and Wireless Propagation Letters* 15 (2015): 1529-1532.

[61] Correas-Serrano, D., Andrea Alù, and Juan Sebastian Gomez-Diaz. "Magnetic-free nonreciprocal photonic platform based on time-modulated graphene capacitors." *Physical Review B* 98.16 (2018): 165428.

[62] Correas-Serrano, Diego, Juan Sebastian Gomez-Diaz, and Alejandro Alvarez-Melcon. "On the influence of spatial dispersion on the performance of graphene-based plasmonic devices." *IEEE Antennas and Wireless Propagation Letters* 13 (2014): 345-348.

[63] Schaug-Pettersen, T., and A. Tonning. "On the optimum performance of variable and nonreciprocal networks." *IRE Transactions on Circuit Theory* 6.2 (1959): 150-158.

[64] Tamagnone, Michele, et al. "Fundamental limits and near-optimal design of graphene modulators and non-reciprocal devices." *Nature photonics* 8.7 (2014): 556-563.

[65] Zhang, Xi-Cheng, and Jingzhou Xu. Introduction to THz wave photonics. Vol. 29. New York: Springer, 2010.

[66] Tonouchi, Masayoshi. "Cutting-edge terahertz technology." Nature photonics 1.2 (2007): 97-105.

[67] Sensale-Rodriguez, Berardi, et al. "Broadband graphene terahertz modulators enabled by intraband transitions." Nature communications 3.1 (2012): 1-7.

[68] Luryi, Serge, Jimmy Xu, and Alexander Zaslavsky, eds. Future trends in microelectronics. New York: Wiley, 1999.

[69] Ryzhii, Victor, M. Ryzhii, and Taiichi Otsuji. "Negative dynamic conductivity of graphene with optical pumping." *Journal of Applied Physics* 101.8 (2007): 083114.

[70] Svintsov, Dmitry, Victor Ryzhii, and Taiichi Otsuji. "Negative dynamic Drude conductivity in pumped graphene." *Applied Physics Express* 7.11 (2014): 115101.

[71] Kumar, Anshuman, et al. "Chiral plasmon in gapped Dirac systems." *Physical Review B* 93.4 (2016): 041413.

[72] Song, Justin CW, and Mark S. Rudner. "Chiral plasmons without magnetic field." Proceedings of the National Academy of Sciences 113.17 (2016): 4658-4663.

[73] Friedlan, Alex, and Marc M. Dignam. "Valley polarization in biased bilayer graphene using circularly polarized light." Physical Review B 103.7 (2021): 075414.

[74] Xiao, Di, Wang Yao, and Qian Niu. "Valley-contrasting physics in graphene: magnetic moment and topological transport." Physical review letters 99.23 (2007): 236809.

[75] Gosselin, Pierre, et al. "Berry curvature in graphene: a new approach." The European Physical Journal C 59.4 (2009): 883-889.

[76] You, Jhih-Shih, et al. "Berry curvature dipole current in the transition metal dichalcogenides family." Physical Review B 98.12 (2018): 121109.

[77] Xu, Xiaodong, et al. "Spin and pseudospins in layered transition metal dichalcogenides." Nature Physics 10.5 (2014): 343-350.

[78] Rivera, Pasqual, et al. "Valley-polarized exciton dynamics in a 2D semiconductor heterostructure." Science 351.6274 (2016): 688-691.

[79] McIver, James W., et al. "Light-induced anomalous Hall effect in graphene." *Nature physics* 16.1 (2020): 38-41.

[80] Guddala, Sriram, et al. "All-optical nonreciprocity due to valley polarization pumping in transition metal dichalcogenides." Nature Communications 12.1 (2021): 1-9.

[81] Tasolamprou, Anna C., et al. "Experimental demonstration of ultrafast THz modulation in a graphene-based thin film absorber through negative photoinduced conductivity." ACS photonics 6.3 (2019): 720-727.

[82] Guinea, F. "Strain engineering in graphene." Solid State Communications 152.15 (2012): 1437-1441.

[83] Guinea, Francisco, M. I. Katsnelson, and A. K. Geim. "Energy gaps and a zero-field quantum Hall effect in graphene by strain engineering." *Nature Physics* 6.1 (2010): 30-33.

[84] Levy, N., et al. "Strain-induced pseudo–magnetic fields greater than 300 tesla in graphene nanobubbles." *Science* 329.5991 (2010): 544-547. Low, Tony, and F. Guinea. "Strain-induced pseudomagnetic field for novel graphene electronics." Nano letters 10.9 (2010): 3551-3554.

[85] Oliva-Leyva, M., and Gerardo G. Naumis. "Anisotropic AC conductivity of strained graphene." Journal of Physics: Condensed Matter 26.12 (2014): 125302.

[86] Nguyen, V. Hung, Aurélien Lherbier, and Jean-Christophe Charlier. "Optical Hall effect in strained graphene." 2D Materials 4.2 (2017): 025041.

[87] Kim, Kyung-Joong, Ya M. Blanter, and Kang-Hun Ahn. "Interplay between real and pseudomagnetic field in graphene with strain." Physical Review B 84.8 (2011): 081401.

[88] Liu, Yanpeng, et al. "Tailoring sample-wide pseudo-magnetic fields on a graphene–black phosphorus heterostructure." Nature nanotechnology 13.9 (2018): 828-834.

[89] Amorim, Bruno, et al. "Novel effects of strains in graphene and other two dimensional materials." Physics Reports 617 (2016): 1-54.

[90] Slipchenko, Tetiana M., et al. "H." *Physical Review Research* 1.3 (2019): 033049.

[91] Maier, Stefan A., ed. *World Scientific Handbook Of Metamaterials And Plasmonics (In 4 Volumes)*. Vol. 16. World scientific, 2017.

[92] Stewart, Matthew E., et al. "Nanostructured plasmonic sensors." *Chemical reviews* 108.2 (2008): 494-521.

[93] Le Ru, Eric, and Pablo Etchegoin. *Principles of Surface-Enhanced Raman Spectroscopy: and related plasmonic effects*. Elsevier, 2008.

[94] Tokel, Onur, Fatih Inci, and Utkan Demirci. "Advances in plasmonic technologies for point of care applications." *Chemical reviews* 114.11 (2014): 5728-5752.

[95] Novotny, Lukas, and Bert Hecht. *Principles of nano-optics*. Cambridge university press, 2012.

[96] Grigorenko, Alexander N., Marco Polini, and K. S. Novoselov. "Graphene plasmonics." *Nature photonics* 6.11 (2012): 749-758.

[97] Tamagnone, Michele, et al. "Reconfigurable terahertz plasmonic antenna concept using a graphene stack." *Applied Physics Letters* 101.21 (2012).

[98] Gómez-Díaz, Juan-Sebastian, and Julien Perruisseau-Carrier. "Graphene-based plasmonic switches at near infrared frequencies." *Optics express* 21.13 (2013): 15490-15504.

[99] Nemilentsau, Andrei, Tony Low, and George Hanson. "Anisotropic 2D materials for tunable hyperbolic plasmonics." *Physical review letters* 116.6 (2016): 066804.

[100] Chen, Wei Ting, Alexander Y. Zhu, and Federico Capasso. "Flat optics with dispersion-engineered metasurfaces." *Nature Reviews Materials* 5.8 (2020): 604-620.

[101] Manzeli, Sajedeh, et al. "2D transition metal dichalcogenides." *Nature Reviews Materials* 2.8 (2017): 1-15.

[102] Li, Guixin, Shuang Zhang, and Thomas Zentgraf. "Nonlinear photonic metasurfaces." *Nature Reviews Materials* 2.5 (2017): 1-14.

[103] Meinzer, Nina, William L. Barnes, and Ian R. Hooper. "Plasmonic meta-atoms and metasurfaces." *Nature photonics* 8.12 (2014): 889-898.

[104] Xia, Fengnian, et al. "Two-dimensional material nanophotonics." *Nature Photonics* 8.12 (2014): 899-907.

[105] Hassani Gangaraj, S. Ali, et al. "Enhanced Nonlinear Optical Effects in Drift-Biased Nonreciprocal Graphene Plasmonics." *ACS Photonics* (2023).

[106] Wang, Qiugu, Wei Hong, and Liang Dong. "Graphene “microdrums” on a freestanding perforated thin membrane for high sensitivity MEMS pressure sensors." Nanoscale 8.14 (2016): 7663-7671.

2. Optically-pumped gapped 2D materials

The objective of this chapter is to calculate the optical conductivity of *gapped* graphene when it is optically pumped with linearly- and circularly-polarized (LP/CP) laser beams, aiming to demonstrate nonreciprocal responses at THz and IR frequencies. To this end, we will first describe the microscopy electronic properties of pristine graphene using the Hamiltonian of this 2D material and then connect it with a tensorial conductivity that models the macroscopy electromagnetic behavior of graphene. This link is provided by the Kubo formalism [5] and the resulting conductivity can be directly employed within the Maxwell's equations to design and model photonic and plasmonic devices. The essential components in Kubo formula, such as the electron wavefunctions and energy, can be determined solving the Dirac-like Schrodinger equation (Dirac equation). As described in further detail below, this approach opens the door to modelling graphene's response when it is subjected to external factors, such as optical pumps. Next, we review the conductivity tensor of graphene under magnetic field and elaborate how off-diagonal conductivity terms give rise to common nonreciprocal responses and Faraday rotation. We introduce then the concept of negative dynamic conductivity and how it is potentially possible to achieve optical amplification (optical gain) in optically-pumped graphene using linearly polarized laser beams.

Our next step focuses on optical valley selection rule in *gapped* graphene, and studies the imbalanced population in different valleys of the gapped 2D material under circularly polarized light by solving the steady state solution of von Neumann equation. We remark that the approach followed here focused on gapped graphene can only be extended to gapped Dirac systems, such as monolayer transition metal dichalcogenides (TMDCs). The broken inversion symmetry of gapped graphene is essential for some exotic phenomena. One of the most notable properties of gapped

graphene is a topological resonance, which produces non-vanishing valley polarization upon optical exciation of circularly polarization, which is absent in pristine graphene [6]. This chapter will calculate the conductivity tensor of gapped graphene following a previous work on chiral plasmons in gapped Dirac systems as well as using the Kubo formalism and compare these results for a good match. The limits of the previous method will be pointed out and the Kubo formalism is proven to be a comprehensive approach to evaluate the conductivity tensor for both pristine and gapped graphene.

This chapter will conclude by describing the details of the fabrication process and characterization of graphene transistors, future experiment set-up of pump-probe THz time-domain spectroscopy (THz-TD) system, as well as the approach employed to calculate Faraday rotation using Malus's law. One has to notice that it is practically very challenging to engineer bandgap in graphene with a desired value. Even though several methods can be used to generate a band gap though, for example, by placing graphene on hexagonal boron nitride or silicon carbide substrates [7],[8], still the presence of the gap significantly limits the feasibility of this approach in practice. Chapter 4 will propose a different technique to overcome this challenge and achieve nonreciprocity combining optically-pumped and strained graphene and other gapless 2D materials.

2.1 Graphene and 2D materials

The findings of fullerene and carbon nanotubes (CNTs) led to the research advancement of 2D materials. Physicists had predicted the unprecedented optoelectronic, magneto-optical, and mechanical properties of graphene. However, it was not until the early 21st century that scientists exfoliated the first flake of one-atom thick graphene from graphite successfully in laboratory [4]. Since then, this methodology of isolation has been applied intensively to other bulk materials to acquire their 2D counterparts. Following the discovery of graphene, scientists have unveiled the

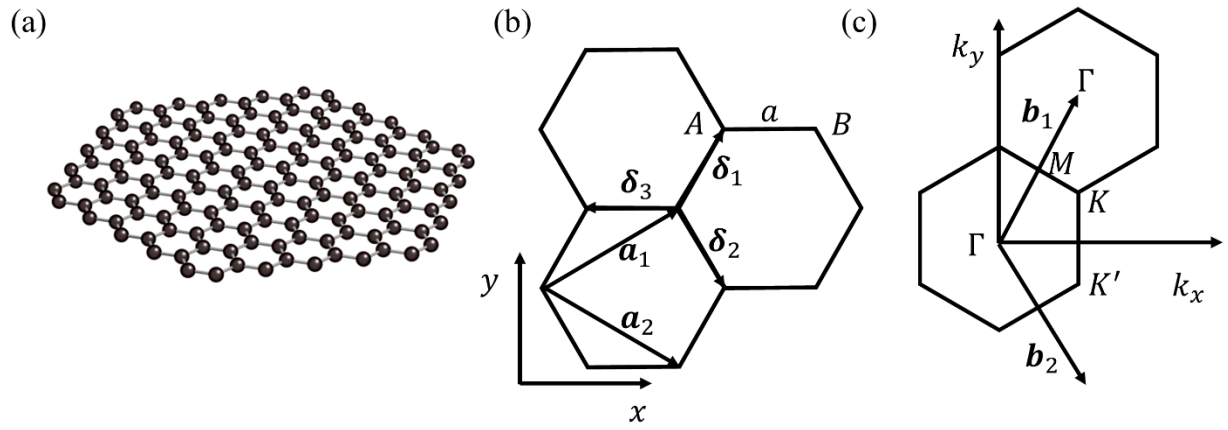

Figure 2.1 (a) A single layer graphene sheet. (b) Two-unit cells of graphene with lattice constant a = 1.42 Å (*x* axis pointed along the zigzag direction) in the physical space. (c) Reciprocal lattice (momentum space) showing the first Brillouin zone with high symmetry points.

existence and fabricated the graphene family, 2D dichalcogenides, and 2D oxides one after another, opening door to a great variety of new physics and the emergence of nanodevices based on 2D materials [9], [10].

In this section, we will introduce the quantum mechanical formulations of graphene needed to calculate its optical conductivity. The magneto-optical responses of graphene will also be presented and discussed.

2.1.1 Hamiltonian

Graphene is the 2D version of graphite and can be isolated from it, as shown in Fig. 2.1(a) for a single layer of graphene. Layers of graphene within graphite are bonded by van der Waals forces originated from the σ bond [40]. Graphene is comprised of two triangular sublattices of carbon atom A and B which reside in different surroundings (see Fig. 2.1(b)). Graphene's electronic properties are mainly determined by the π and π^* bands originated from sp^2 hybridization which can bond with the neighboring atoms thus accounting most of the electronic properties of graphene, whereas the σ bands are irresponsible for the majority of the low energy

effects due to a large energy gap exceeding 10 eV [11]. To study the electronic properties, it is important to acquire the band structure of graphene in the reciprocal space. To construct the reciprocal space, the physical lattice unit vectors are given first to form the physical lattice (as depicted in Fig. 2.1(b)):

$$\boldsymbol{a}_1 = \frac{a}{2}\left(3, \sqrt{3}\right), \qquad \boldsymbol{a}_2 = \frac{a}{2}\left(3, -\sqrt{3}\right), \tag{2.1}$$

where the *x* axis is along armchair direction and *y* axis along zigzag direction. The unit vectors in the reciprocal space satisfy the relation $\boldsymbol{a}_i \cdot \boldsymbol{b}_j = 2\pi\delta_{ij}$ where δ_{ij} represents the Kronecker delta. The reciprocal lattice is bounded by the lines bisecting the reciprocal unit vectors $\boldsymbol{b}_j$. Specifically, the one that is bounded by the lines bisecting the vectors to the nearest reciprocal lattice points is usually called the First Brillouin Zone (FBZ). The FBZ (see Fig. 2.1(c)) contains all the possible electron momenta. There are also second, third, etc. Brillouin zones which are just the replica of the FBZ in the momentum space that do not provide additional information. The six vertices of FBZ are called the Dirac points and denoted by and K and K'. These points are placed alternately on the six vertices of the hexagon in the reciprocal lattice. The center point between K and K' is called the M point and the point where $\boldsymbol{k} = \boldsymbol{0}$ is called the Γ point where $\boldsymbol{k}$ is the electron momentum. In Fig. 2.1 the *x* axis in the physical space is pointed along the armchair direction, and as a result the k_x axis aligns with the zigzag direction in the reciprocal lattice. The choice of a given coordinate is a matter of simplicity and does not change the physical properties of graphene. The single-particle energy is calculated within the tight-binding approximation approach [40]. The Hamiltonian for a pristine graphene layer considers only the nearest-neighbor hopping. Such an approximation is sufficient to characterize the low energy properties [12]. The Hamiltonian can be expressed as [13]:

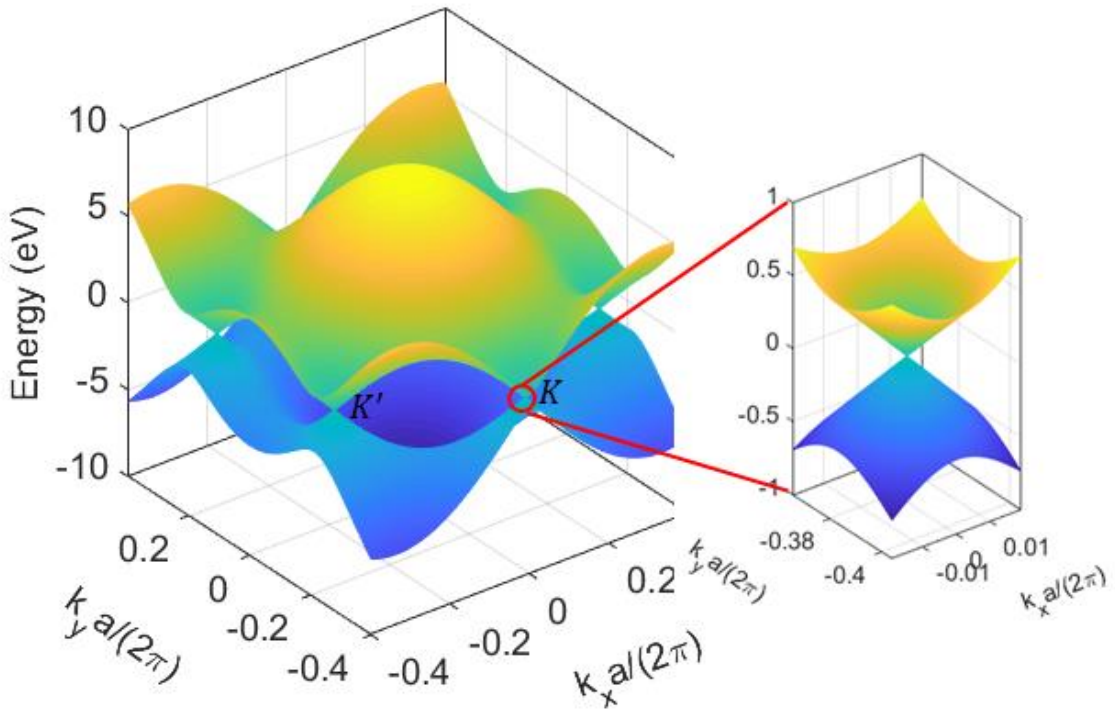

Figure 2.2 Band structure of gapless pristine graphene. The inset shows the linear dispersion close to Dirac points.

$$\widehat{H} = \begin{pmatrix} 0 & \Delta_{\boldsymbol{k}} \\ \Delta_{\boldsymbol{k}}^{*} & 0 \end{pmatrix}, \tag{2.2}$$

where $\Delta_{\boldsymbol{k}} = -t\sum_{l=1}^{3} e^{i\boldsymbol{k}\cdot\boldsymbol{\delta}_l}$ stems from the nearest-neighbor hopping and t is the hopping integral and typically set to 3.09 eV [14]. The kinetic energy of the electron allows the hopping between neighboring sites. $\boldsymbol{\delta}_l$ represent the hopping vectors connecting a carbon atom to its three nearest neighbors. By solving the graphene Hamiltonian, one can obtain the eigen energy:

$$\mathcal{E}_{\boldsymbol{k}} = \pm\sqrt{3 + 2\cos\left(\sqrt{3}k_y a\right) + 4\cos\left(\frac{\sqrt{3}k_y a}{2}\right)\cos\left(\frac{3k_y a}{2}\right)}, \tag{2.3}$$

where the $+$ sign represents the energy for conduciton band (π^* band, c band) and the $-$ sign the energy for valence band (π band, v band). The two bands are plotted in Fig. 2.2. In the hexagonal unit cell, there are 6 atoms with each shared by 3 neighboring cells, which equals to 2 atoms in

one cell. Each atom will provide one valence electron so there are two valence electron in one cell. Here, we will restrict our analysis with electrons with low/moderate energy less than 1 eV. In this scenario, it is meaningful to address graphene's unique band structure near a Dirac point $\boldsymbol{K}$. A Dirac points is where the conduction and valence bands touch. By a change of variable $\boldsymbol{k} - \boldsymbol{K} \rightarrow \boldsymbol{k}$ and making a Taylor expansion [40] around $\boldsymbol{k}$, we can obtain a linear form of Hamiltonian for grahene as:

$$\widehat{H} = \hbar v_f \begin{pmatrix} 0 & e^{i\varphi}\left(k_x - i\tau k_y\right) \\ e^{-i\varphi}\left(k_x + i\tau k_y\right) & 0 \end{pmatrix}, \tag{2.4}$$

where we have chosen the x axis along the zigzag direction, $\hbar$ is the reduced Planck constant, $v_f \approx c/300 \sim 10^6\ m \cdot s^{-1}$ is the Fermi velocity of graphene whose value is associated with the electron kinetic energy which equals the Fermi energy E_F (chemical potential μ_c) by solving $E_F = \frac{1}{2} m v_f^2$, and φ is a geometric phase. This phase stems from the Taylor expansion of the Hamiltonian and is different for the six Dirac points. Besides, $\tau = 1$ for K and $\tau = -1$ for K'. From Eq. 2.4, it can be observed that particles near K and K' possess different chirality. Additional insights about the significance of K and K' Dirac points for optical selection will be discussed later in this thesis. By solving the eigen problem, we get the low energy band structure of graphene:

$$\mathcal{E}_{\boldsymbol{k}} \approx \pm \hbar v_f |\boldsymbol{k}|. \tag{2.5}$$

The dispersionless band structure is shown by the inset of Fig. 2.2. According to this energy-momentum relation, carriers in gapless pristine graphene are usually called massless Dirac Fermions because they travel at a constant speed same as Fermi velocity regardless of their momentum. The wavefunctions can be obtained from the eigenvectors [13] as

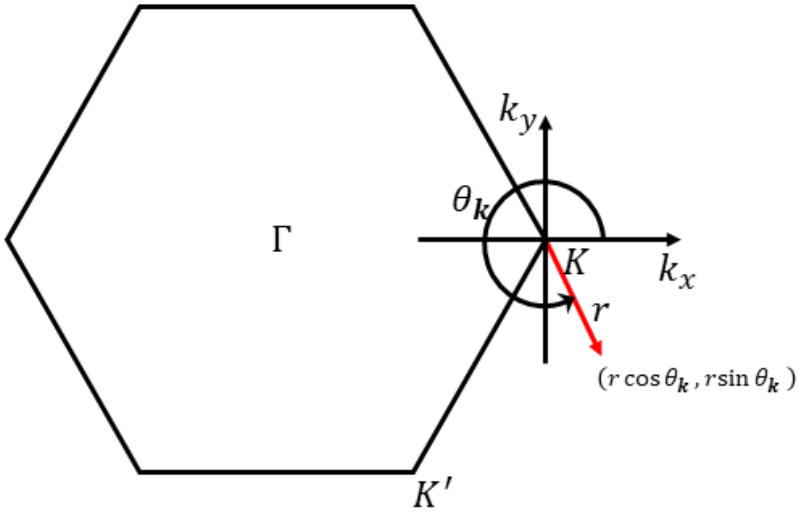

Figure 2.3 Polar coordinate configuration at one Dirac point.

$$\psi_{vk} = \frac{1}{\sqrt{2}}\begin{pmatrix} 1 \\ \frac{ve^{-i\varphi}(k_x + i\tau k_y)}{|\boldsymbol{k}|} \end{pmatrix}, \tag{2.6}$$

where $v = c, v$ denotes the band index for conduction and valence bands. To facilitate the analysis and numerical calculations, we introduce here a polar coordinate system to simplify the form of the wavefunction. The polar coordinate is set with the origin sitting at each of the six Dirac points respectively and we plot one of such configurations in Fig. 2.3. In that case, the wavefunction for pristine graphene takes the form:

$$\psi_{vk} = \frac{1}{\sqrt{2}}\begin{pmatrix} 1 \\ ve^{-i\varphi}e^{i\theta_k} \end{pmatrix}, \tag{2.7}$$

where θ_k is the polar angle of a wavevector with respect to the Dirac point and the φ is a geometric phase resulting from Taylor expansion of the Hamiltonian.

2.1.2 Kubo formalism and optical conductivity

Let us study the optical responses of graphene dictated by its optical conductivity, which can be modeled by 2×2 conductivity tensor [15]

$$\bar{\boldsymbol{\sigma}} = \begin{pmatrix} \sigma_{xx} & \sigma_{xy} \\ \sigma_{yx} & \sigma_{yy} \end{pmatrix}. \tag{2.8}$$

The induced surface current $\boldsymbol{J}$ still obeys Ohm's law but with the conductivity tensor replacing the commonly used scalar conductivity, i.e.,

$$\boldsymbol{J} = \bar{\boldsymbol{\sigma}} \cdot \boldsymbol{E}. \tag{2.9}$$

In the absence of external factors such as magnetic bias, optical pumps, etc., the off-diagonal elements vanish adopting an appropriate coordinate system. The conductivity tensor elements can be calculated using a wavenumber-resolved Kubo formula [18]:

$$\begin{aligned} \sigma_{\alpha\beta} = -i\frac{g_s \hbar e^2}{(2\pi)^2}\sum_{ss'}\int d\boldsymbol{k}\frac{f(\mathcal{E}_{s\boldsymbol{k}}) - f(\mathcal{E}_{s'\boldsymbol{k}'})}{\mathcal{E}_{s\boldsymbol{k}} - \mathcal{E}_{s'\boldsymbol{k}'}} \\ \times \frac{\langle \psi_{s\boldsymbol{k}}|\hat{v}_\alpha|\psi_{s'\boldsymbol{k}'}\rangle\langle\psi_{s'\boldsymbol{k}'}|\hat{v}_\beta|\psi_{s\boldsymbol{k}}\rangle}{\mathcal{E}_{s\boldsymbol{k}} - \mathcal{E}_{s'\boldsymbol{k}'} + \hbar\omega + i\eta}, \end{aligned} \tag{2.10}$$

where $g_s = 2$ accounts for the spin degeneracy, $s, s' = c, v$ denotes the band index, $\eta = \hbar\tau^{-1}$ is the damping energy with τ being the scattering time and $f(E) = 1/\left(1 + e^{\frac{\varepsilon - \mu_c}{k_B T}}\right)$ is the Fermi-Dirac (FD) distribution with k_B being the Boltzmann constant. The electron wavefunction $\psi_{s\boldsymbol{k}}$, the velocity operator $\hat{v}_\alpha = \hbar^{-1}\partial_{k_\alpha}\hat{H}$ with $\alpha, \beta = x, y$ and the electron energy $\mathcal{E}_{s\boldsymbol{k}}$ can be acquired from the graphene Hamiltonian. In this expression, we have not taken into account nonlocal phenomena so that $\boldsymbol{k}' = \boldsymbol{k}$. Nonlocal extensions are indeed possible [18] but are out of the context of this work. Note that the conductivity is generally complex-valued due to damping effects. The integral of Eq. (2.10) is numerically calculated within the FBZ, taking into account interband and intraband transitions shown schematically in Fig. 2.4. The incoming light excites one electron in

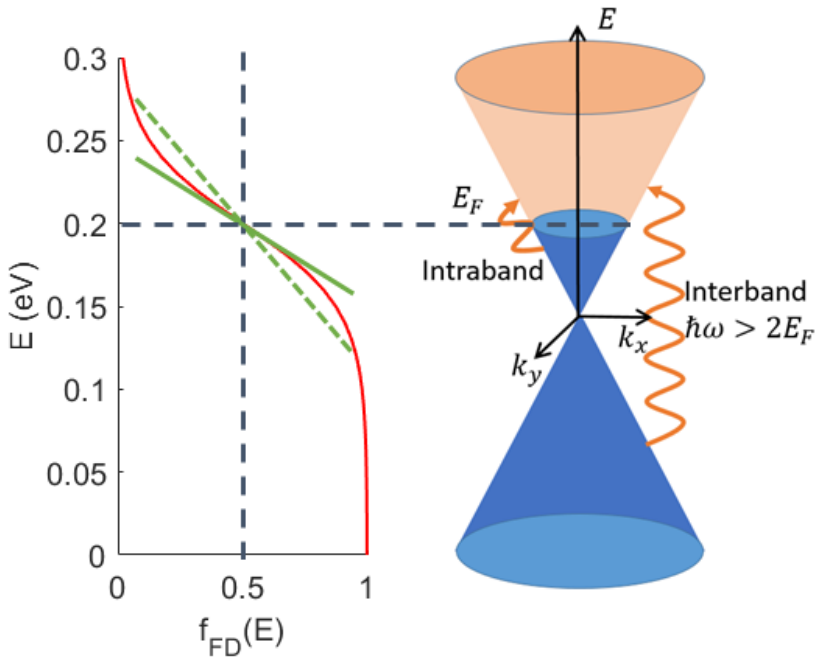

Figure 2.4 Intraband and interband transitions in graphene. The Fermi distribution is also shown and aligned with the Dirac cone. The chemical potential is set to $\mu_c = 0.2\ eV$.

the occupying state and into a vacant state either in the same band or different band, creating an electron-hole pair which contributes to the conducting current. That is the physical origin of the electrical conductivity of graphene. In the Kubo formula, $\langle\psi_{s\boldsymbol{k}}|\hat{v}_\alpha|\psi_{s'\boldsymbol{k}'}\rangle\langle\psi_{s'\boldsymbol{k}'}|\hat{v}_\beta|\psi_{s\boldsymbol{k}}\rangle$ is the contribution from the electron velocity in different directions. An interpretation of the first term within the integral is also shown in Fig. 2.4. With large incoming photon energy, this term is inversely proportional to the slope of the dashed green line in the Fermi distribution plot. When the photon energy is small, this term grows large because the green line becomes less steep, and it reaches maximum at the Fermi energy. The first term turns into a derivative $\partial f(E)/\partial E$ associated with the tangential solid green line. This explains why the selection rules only allow most of the intraband transitions happen near the Fermi energy and the interband transitions become negligible. It is important to use the momentum-resolved Kubo formula to obtain the conductivity because in the presence of external fields, the electron wavefunction and eigenstates are modified, and the

perturbed Hamiltonian will allow us to incorporate these changes into the Kubo formula. This will enable us to calculate the conductivity under different external perturbation such as magnetic fields, optical pumps, or mechanical deformations, etc.

From Eq. 2.5 and the band structure plotted in Fig. 2.2, it is clear that the linear dispersion between the energy and the momentum of electrons is conical when this relation is plotted in $\boldsymbol{k}$ space, that is why it is called the Dirac cone. The rotational symmetry of this dispersion allows us to rewrite the Kubo formula with respect to the energy [15]:

$$\sigma(\omega,\mu_c,\tau,T) = \frac{-ie^2(\omega+i\tau^{-1})}{\pi\hbar^2}\left[\frac{1}{(\omega+i\tau^{-1})^2}\int_0^{\infty}\varepsilon\left(\frac{\partial f(\varepsilon)}{\partial\varepsilon}-\frac{\partial f(-\varepsilon)}{\partial\varepsilon}\right)d\varepsilon - \int_0^{\infty}\frac{f(-\varepsilon)-f(\varepsilon)}{(\omega+i\tau^{-1})^2-4(\varepsilon/\hbar)^2}d\varepsilon\right], \tag{2.11}$$

where ω is the angular frequency of the incoming light, μ_c is the chemical potential, τ is the phenomenological relaxation time which generally account for the average time between two consecutive scattering events, and e is the electron charge. The conductivity is a function of temperature, and it is set to 300 K in all calculations shown here for simplicity. Qualitatively, an intuitive way to understand and identify each term in this equation can be provided. Since the conductivity describes the collective behaviors of carriers, the first term in the square bracket which evaluates two derivatives with respect to energy are related to *intraband* contributions to the current. $\partial f(\varepsilon)$ characterizes the probability of an electron with energy ε within the energy range of $\partial\varepsilon$ to contribute to an electron current, if multiplied by electron charge and velocity within one band. Hence, the $\partial f(-\varepsilon)$ term is the corresponding hole current in valence band with the same kinetic energy, but having a negative sign due to the negative charge of electron. The second term in the square bracket is the *interband* contribution. Supposing the optical frequency to be

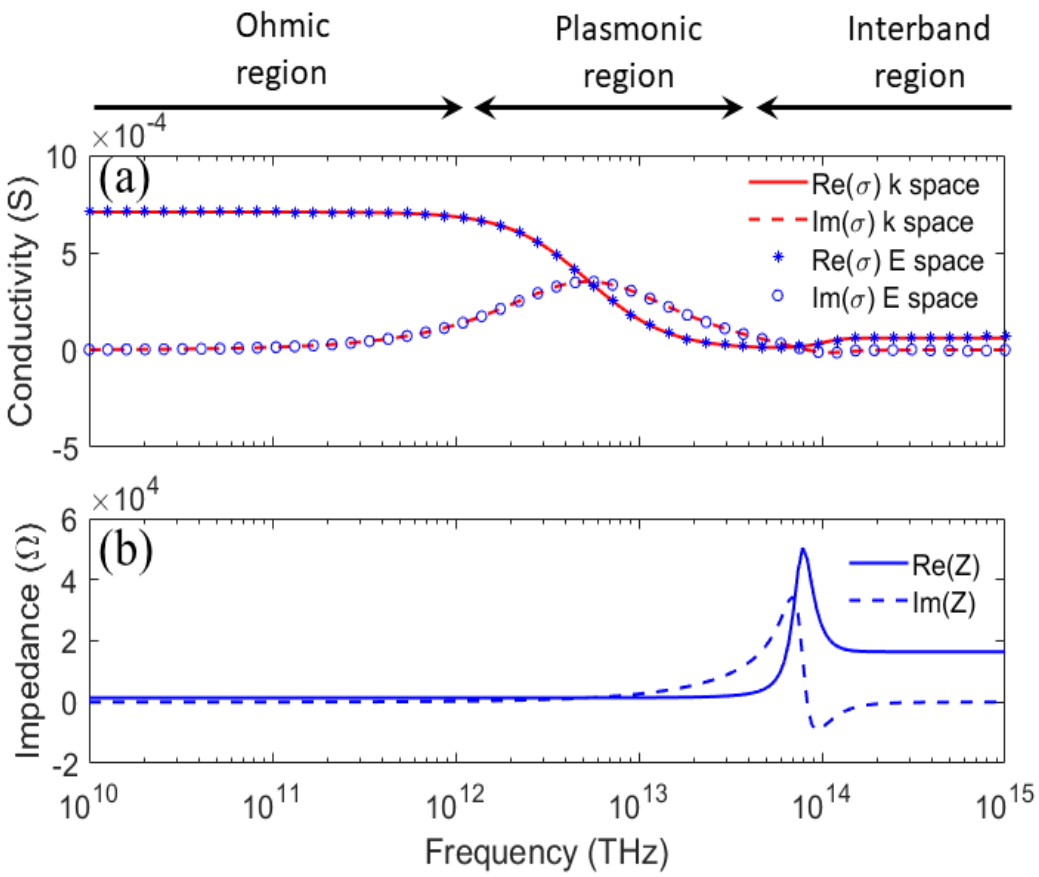

Figure 2.5 The conductivity of pristine graphene computed from Kubo formula with respect to momentum (Eq. 2.10) and energy (Eq. 2.11). Other parameters are $\mu_c = 0.2\ eV$ and $\tau = 30\ fs$.

$2\varepsilon/\hbar$, the interband transition probability for this energy would be $[f(-\varepsilon) - f(\varepsilon)]$ due to Pauling blocking. The intraband and interband transitions are schematically shown in Fig. 2.4. Fig. 2.5a shows the conductivity of pristine graphene versus frequency computed from Kubo formula with respect to the momentum and the energy respectively. The associated impedance can be calculated by $Z = \sigma^{-1}$ and is shown in Fig. 2.5(b). We can see that at frequencies much lower than τ^{-1}, graphene behaves mostly like a resistor because of a nearly real conductivity. This range extends from DC to microwaves. From THz to IR regions, the imaginary becomes larger and gradually dominates while the interband transition is still negligible. This region is typically called plasmonic region due to fact that graphene acts like a plasma. When the optical frequency grows larger such

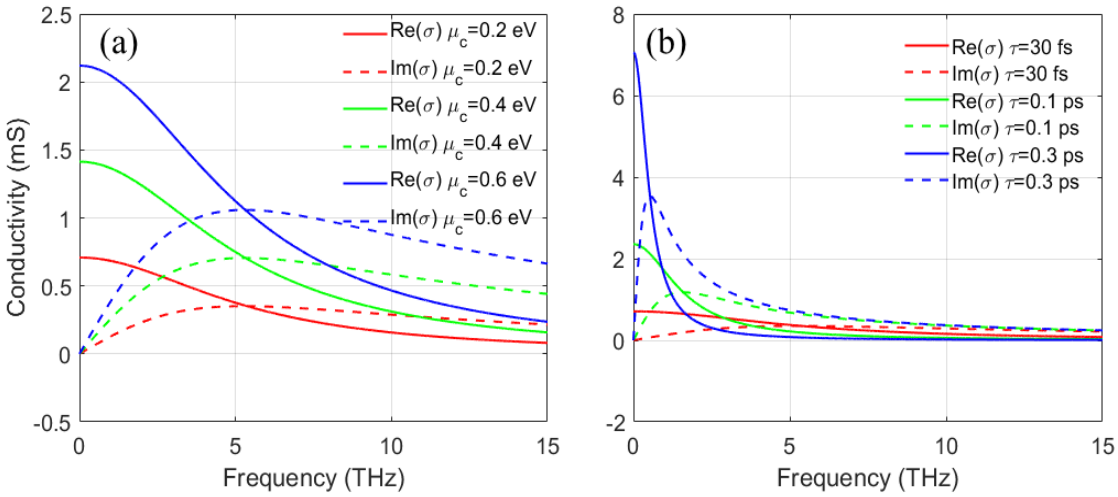

Figure 2.6 Dependence of graphene conductivity on various (a) chemical potential μ_c with $\tau = 30\ fs$ and (b) scattering time τ with $\mu_c = 0.2\ eV$.

that $\hbar\omega > 2\mu_c$, the Fermi distribution guarantees a larger possibility of interband transitions thus it is called the interband region.

The two integrals in the Kubo formula can be evaluated individually to obtain the intraband and interband conductivity. The former has an analytical expression:

$$\sigma_{intra} = \frac{ie^2kT}{\pi\hbar^2(\omega + i\tau^{-1})} ln\left(2 + 2\cosh\left(\frac{\mu_c}{kT}\right)\right). \tag{2.12}$$

The interband integral can have a closed-form expression when $\mu_c \gg kT$. Under this approximation, the interband contribution becomes:

$$\sigma_{intra} \approx \frac{e^2|\mu_c|}{\pi\hbar^2(\omega + i\tau^{-1})}, \tag{2.13}$$

which agrees well with the classical Drude model [15]. Here, we also study the dependence of graphene conductivity on chemical potential and scattering time in terahertz regime. The Drude model of Eq. 2.12 is used to account for the intraband transitions which is accurate enough to characterize the optical responses at THz and far/mid-IR frequencies because interband transitions

are negligible there. As shown in Fig. 2.6, an increased chemical potential leads to larger carrier density. An increased scattering time causes lower transition frequency to plasmonic region. These facts imply a wide tunability in graphene conductivity. In experiments, electrostatic biasing can change graphene's chemical potential while impurity doping can modify its scattering time.

2.1.3 Magnetic-biased graphene

When a graphene layer is biased by a perpendicular magnetic field, the Hamiltonian is modified in a way that the momentum $\boldsymbol{p}$ is replaced with $\boldsymbol{p} - e\boldsymbol{A}$, where $\boldsymbol{A}$ is the magnetic vector

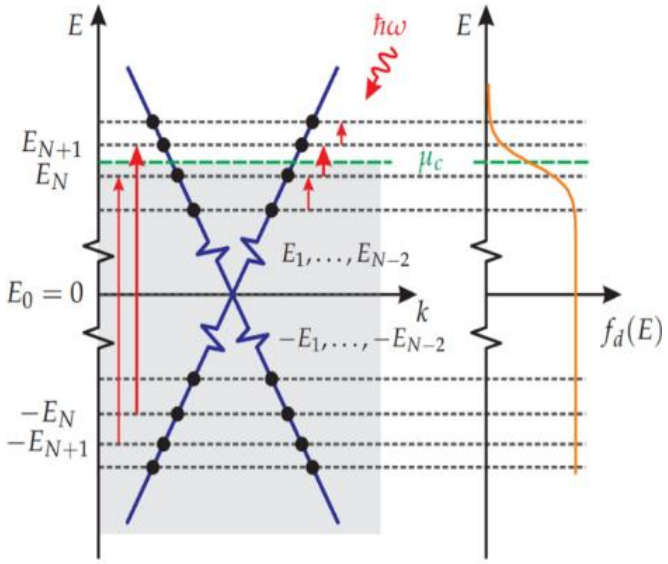

Figure 2.7 Landau levels under magnetic field with the Fermi distribution showing the selection rules [21].

potential. Solving the resulting Hamiltonian is a relatively standard process as with that of a quantum harmonic oscillator [19]. Therefore, the energy will be quantized rather than being continuous due to the quantization of cyclotron orbits of electron under magnetic field. The resulting quantized energy levels are called Landau levels [20] which are schematically shown in Fig. 2.7 [21]. The optical selection rules will only favor those transitions with the quantum number satisfying $n_i - n_f = \pm 1$ [21], as denoted by red arrowheads in Fig. 2.7.

Electrons will acquire a transverse velocity by virtue of the presence of the magnetic field, thus leading to non-vanishing values of the off-diagonal elements in the conductivity tensor. In this case, the diagonal and off-diagonal terms are given by [21]:

$$\sigma_{xx}(\omega, B_0) = \frac{e^2 v_f^2 |eB_0|}{i\pi} \sum_{n=0}^{\infty} \left\{ \frac{1}{E_{n+1} - E_n} \times \frac{f(E_n) - f(E_{n+1}) + f(-E_{n+1}) - f(-E_n)}{(E_{n+1} - E_n)^2 - \hbar^2(\omega + i\tau^{-1})^2} + (E_n \to -E_n) \right\},$$

$$\sigma_{yx}(\omega, B_0) = -\frac{e^2 v_f^2 eB_0}{\pi} \sum_{n=0}^{\infty} \left\{ [f(E_n) - f(E_{n+1}) - f(-E_{n+1}) + f(-E_n)] \times \left[\frac{1}{(E_{n+1} - E_n)^2 - \hbar^2(\omega + i\tau^{-1})^2} + (E_n \to -E_n) \right] \right\}, \tag{2.14}$$

where B_0 is the magnetic field and E_n is the quantized energy level. Notice that in the conductivity tensor, the off-diagonal terms satisfy the relation of $\sigma_{xy} = -\sigma_{yx}$. Under small magnetic field, we can assume the intervals between adjacent Landau levels are small, i.e. the energy can be seen as quasi-continuous. Under such low-magnetic approximations, the summation can be approximated by integration of diagonal element in Eq. 2.14 while the off-diagonal element yields:

$$\sigma_{xy}(\mu_c, B_0) = -\frac{e^2 v_f^2 eB_0}{\pi\hbar^2} \left[\frac{1}{(\omega + i\tau^{-1})^2} \int_0^{\infty} \left(\frac{\partial f(\varepsilon)}{\partial \varepsilon} + \frac{\partial f(-\varepsilon)}{\partial \varepsilon} \right) d\varepsilon + \int_0^{\infty} \frac{1}{(\omega + i\tau^{-1})^2 - 4(\varepsilon/\hbar)^2} d\varepsilon \right]. \tag{2.15}$$

In addition, assuming that μ_c is much larger than the energy intervals, this equation will only take into account the intraband transitions and agrees well with the semiclassical Lorentz-Drude model:

$$\sigma_{xx}(\omega, B_0) = \sigma_0 \frac{1 - i\omega\tau}{(\omega_c\tau)^2 + (1 - i\omega\tau)^2},\ \sigma_{yx}(\omega, B_0) = \sigma_0 \frac{\omega_c\tau}{(\omega_c\tau)^2 + (1 - i\omega\tau)^2}, \quad (2.16)$$

where

$$\sigma_0 = \frac{2e^2\tau}{\pi\hbar^2} kT ln\left(2\cosh\frac{\mu_c}{2kT}\right) \quad (2.17)$$

is the DC conductivity of graphene, and $\omega_c = \frac{eB_0 v_f^2}{\mu_c}$ is the cyclotron frequency. This parameter quantifies the frequency of carriers' circular movement under the perpendicular magnetic field. For the sake of illustration, Fig. 2.8 plots the conductivity computed from the quantum (Landau)

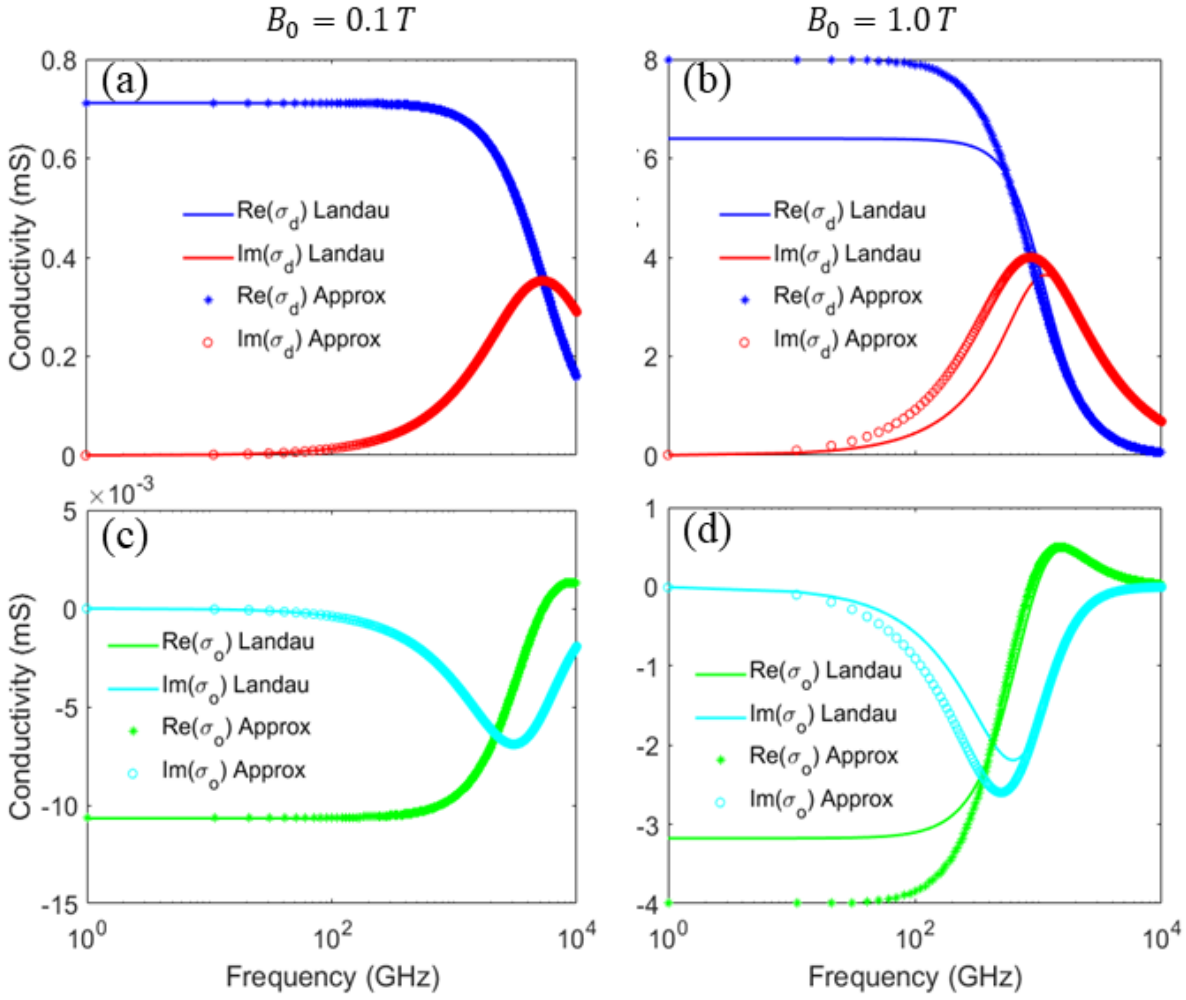

Figure 2.8 Diagonal and off-diagonal conductivity of graphene computed from quantum and Lorentz-Drude models showing both real and imaginary parts. Other parameters are $\mu_c = 0.2\ eV$ and $\tau = 30\ fs$..

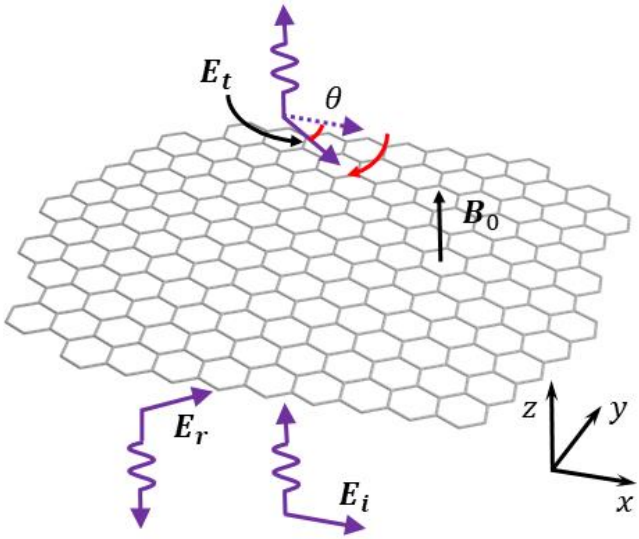

Figure 2.9 Graphene under magnetic bias showing the rotation angle. E_i, E_r, E_t are the electric field of the incident, reflected and transmitted waves.

and Lorentz-Drude models under small and magnetic fields. Results show that under small field, two models provide good agreement and for larger magnetic fields they start to deviate, and the quantum model gives the most accurate results.

The non-vanishing off-diagonal elements of the conductivity tensor will give rise to a magneto-optical phenomenon called Faraday effect [22] which was discovered by Michael Faraday. The most relevant consequence is that under magnetic field biasing the TRS is broken, enabling different rotation of polarization direction of electromagnetic wave propagating in opposite ways. The Faraday rotation angle θ_F (see Fig. 2.9) for graphene on dielectric substrate is obtained by applying Maxwell's equations (derivation from [21]) and is given by:

$$\theta_F = \tan^{-1}\left(\frac{\eta_0 \sigma_{yx}}{1 + n + \eta_0 \sigma_{xx}}\right), \tag{2.18}$$

where η_0 is the free space impedance and n is the dielectric constant of the substrate.

In addition to modifying the external magnetic bias, graphene offers a variety of ways to manipulate Faraday rotation, such as chemical doping, electrostatic biasing, and using

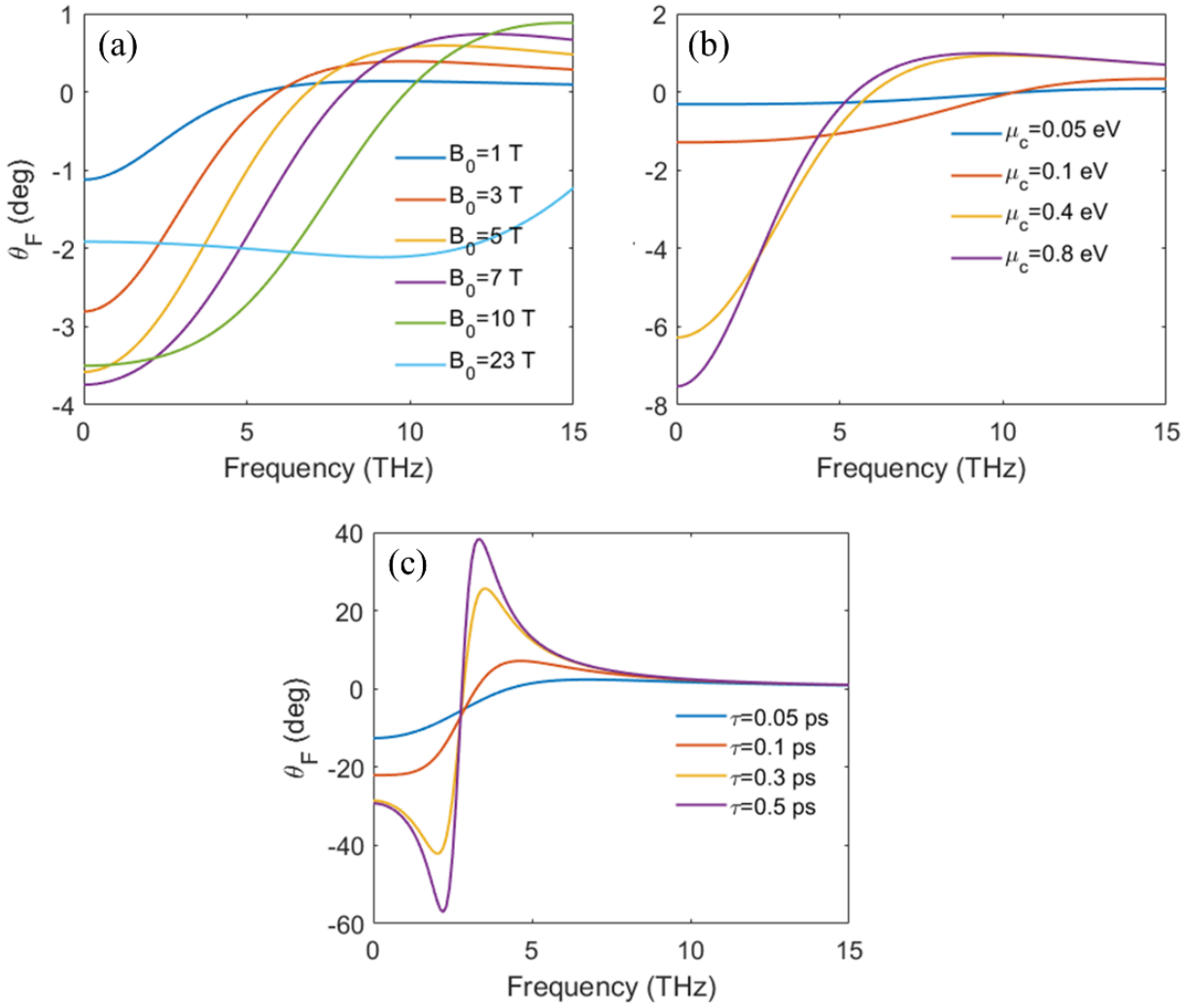

Figure 2.10 Faraday rotation (in degrees) versus various perpendicular magnetic fields, chemical potential, and relaxation scattering times. When not changing, the parameters are set as $B_0 = 7\,T, \mu_c = 0.4\,eV, \tau = 30\,fs$.

nanostructured configurations [23], [24]. We plotted the rotation angle for various values of B_0, μ_c and τ respectively in Fig. 2.10 using the accurate quantum model.

We can see that the external magnetic field can shift the peak of rotation angle and increase the angle. On the other hand, increasing chemical potential can boost the rotation angle while has negligible effect on moving the position where the rotation happens. Changing the scattering time can drastically increase the rotation angle but changing the peak from broadband to very narrow

band. Notice that $B_0 = 23\ T$ is almost impossible to achieve in practice, however, huge local magnetic field greater than 300 Tesla has been measured in graphene nanobubbles [25] which hold promise on achieving effectively large Faraday rotation without magnetic field in the near future.

2.2 Negative dynamic conductivity

An exciting direction of graphene under optical pump is to have negative dynamic conductivity in a wide spectrum range over terahertz frequencies which could lead to the development of active devices exhibiting gain in the THz and IR bands, including oscillators, modulators, sensors, etc. [26]-[30]. Negative conductivity has theoretically been shown to be tunable over terahertz frequencies upon a relatively weak pump owing to fast intraband relaxation channels such as Auger recombination, carrier-carrier (C-C) interactions and optical phonons (OP), etc. [31]-[33]. Stimulated emission, associated with the interband transitions have been demonstrated due to the inverted population of near the Dirac cones under optical pump, showing the possibility of turning conductivity from positive to negative in graphene [34]. A superluminal plasmonic platform is proposed in population inverted bilayer graphene with resonant gain [35]. An ultrafast, optically tunable thin film graphene modulator has been experimentally demonstrated based on negative dynamic conductivity [36]. Negative dynamic conductivity has also been theoretically explored in graphene metasurfaces with enhanced resonances to boost the plasmonic responses exhibiting the reconfigurable properties at terahertz frequencies [37]-[39].

Population inversion describes the phenomenon in a two-level system, where most of the particles in the system stay in the excited state than that remain in the ground state. This phenomenon is very unlikely to take place in semiconductors in thermal equilibrium because carriers governed by Fermi-Dirac distribution tend to stay in the lower energy bands and it requires high energy photons that usually exceed the bandgap to bring them to excited states.

Thanks to the gapless features of graphene, the populations at the band edges satisfy $f_e(0) = f_h(0) = 0.5$. Therefore, with even small injection it should theoretically be possible to flip the carrier-to-hole occupation in the two bands near the Dirac points. The creation of population inversion is required for spontaneous emission and stimulated emission, the latter being essential for optical amplification. Even more promising is the fact that the frequencies for optical amplification in graphene range from terahertz regime all the way to the IR due to its zero bandgap. Even though there have been experiments demonstrating the amplification of terahertz signals in graphene during the fast relaxation to recombination process through THz TDS [41],[42], optical gain at THz remains a significant technological challenge.

With only optical interband excitation, the photogenerated carriers will at best achieve a steady-state occupation of one half at the excited states under continuous pumping. However, when coupled to phonons with appropriate energy and momentum, photoexcited carriers can relax to lower energy levels accompanied by a cascade of phonon emission [43]. There are also other channels that would assist the photoexcited carriers to relax to the lower energy levels of the bands

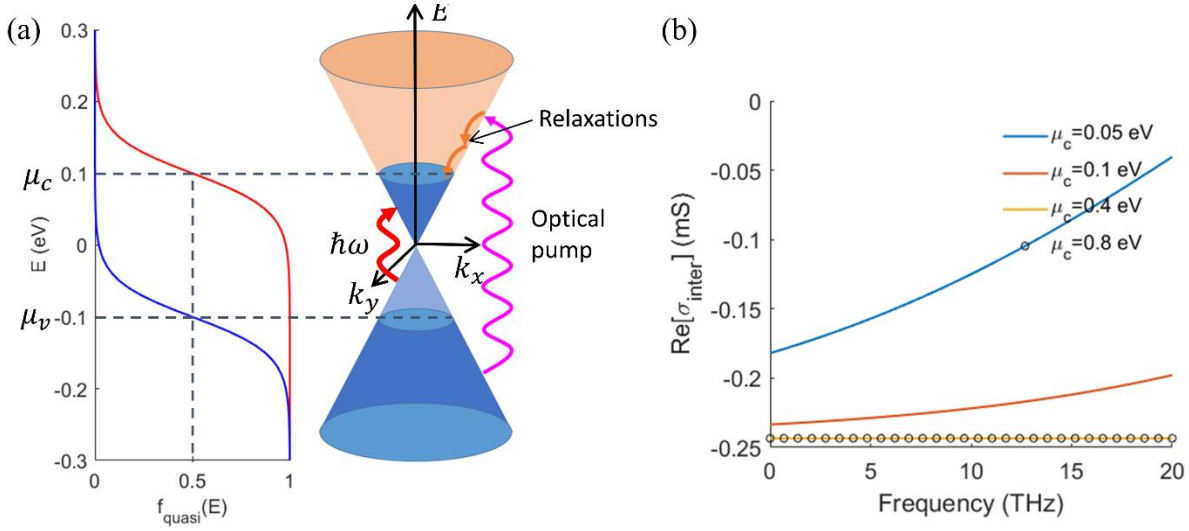

Figure 2.11 (a) Schematic illustrating the possible negative conductivity for photon energy smaller than $2\mu_c$. (b) The real part of interband conductivity versus the optical frequency for several quasi-Fermi energies.

[32]. Because of a lower density of states (DOS) and a relatively long interband recombination time compared to the relaxation times, there will be an accumulation of pockets of carriers toward the band edges. The entire process is schematically shown in Fig. 2.11(a) where we assume graphene has reached a quasi-equilibrium state under symmetrical interband optical pump which implies that quasi-Fermi energies for the two bands satisfy $\mu_v = -\mu_c$. The real part of the interband conductivity, calculated from Fermi golden rule, is given by [70]:

$$Re[\sigma_{inter}] = \frac{e^2}{\hbar}\left[f_v\left(-\frac{\hbar\omega}{2}\right) - f_c\left(\frac{\hbar\omega}{2}\right)\right]. \tag{2.19}$$

One can readily find that for photon with energy $\hbar\omega < 2\mu_c$, it is possible to have negative conductivity. The interband conductivity as a function of the optical frequency for several quasi-fermi energies is plotted in Fig. 2.11(b). One can see that the bandwidth broadens when quasi-Fermi energy gets higher. Quasi-Fermi energy is associated with pumping light photon energy $\hbar\Omega$, larger the frequency Ω, higher the quasi-Fermi energy. This allows us to dynamically tune the bandwidth of negative conductivity. Note that this calculation has not taken into account details of relaxation and assumes quasi-Fermi energies for the two bands.

2.3 Light-induced Faraday rotation

The objective of this section is to overview nonreciprocal responses of gapped graphene under CP light. The reason for using gapped graphene is that in gapped Dirac system where inversion symmetry is broken owing to the two inequivalent sublattices, the optical transitions at the two distinct valleys couple exclusively to optical excitations of opposite CP [44],[45]. We will first review the concept of valley-dependent optical selection. Then we go over the theoretical framework based on quantum Liouville's theorem and obtain a steady-state solution for population

under CP light pump. Finally, we will study Berry curvature and compute the Hall conductivity using both Berry curvature method and Kubo formula.

2.3.1. Valley-dependent optical selection

Modern semiconductor technology is mostly based on the manipulation of electron charge. However, there are still other degrees of freedom such as spin and valley. Over recent decades, there has been intensive explorations on spintronics using the spin degree of freedom of electrons. Because of its demonstrated ability and efficiency of data processing and storage, there are ever increasing interest and speculation of its possible future applications, in areas such as quantum computing [31] and spin-based transistors [46]. Moreover, the field of valleytronics - which uses another degree of freedom of electrons - has revived following the blossoming and experimental demonstration of 2D materials and their exotic properties.

In solid state physics, the local extrema of the electronic band structure are called valleys. In graphene and many other 2D materials, there are two distinct valleys K and K' where the electrons within each possess different physical properties [47]. These properties opens up to a new field called 'valleytronics' as opposed to electronics as it provides schemes to address each valley with external fields, thus can be used to store and process information [48], [48]. One of the most significant perspectives of valleytronics is the valley-dependent optical selection, where circularly-polarized light with different handedness will interact more with one valley than another, giving rise to circular dichroism based on materials with broken inversion symmetry [49]. Promising candidates are gapped graphene and transition metal dichalcogenides (TMD) [50], [51]. Moreover, the spin and valley coupling can even enable stable valley locking [52]. This optically-induced phenomenon has completely different mechanism with optical activity in birefringent materials

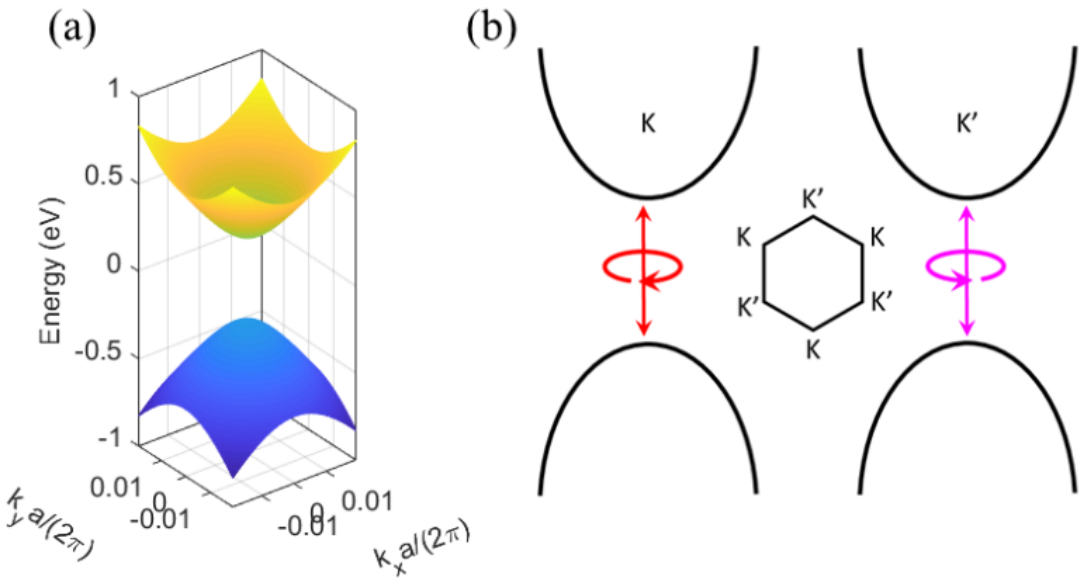

Figure 2.12 (a) Band structure of gapped graphene with bandgap $\Delta = 0.5\ eV$. (b) Schematic of valley-dependent optical selection rules. Each handedness can only couple with one valley.

since the former breaks TRS but the latter does not [53]. To demonstrate this in short, let us consider Hamiltonian of gapped graphene following the same linear approximation as in [54]:

$$\widehat{H} = \hbar v_f \begin{pmatrix} \delta/2 & e^{i\varphi}\left(k_x - i\tau k_y\right) \\ e^{-i\varphi}\left(k_x + i\tau k_y\right) & -\delta/2 \end{pmatrix}, \tag{2.20}$$

where δ is the energy bandgap. Solving the above Hamiltonian, we obtain the band structure which is plotted in Fig. 2.12(a). Using the electron wavefunctions we are able to evaluate the transition dipole matrix elements as

$$\boldsymbol{R}_{jj'}(\boldsymbol{k}) = \frac{i}{2}\int \psi_j^*(\boldsymbol{k})\partial_{\boldsymbol{k}}\psi_{j'}(\boldsymbol{k})d\boldsymbol{r} + h.c., \tag{2.21}$$

where $j, j' = \{v, \tau\}$ is the complex index of a given band. Consider a right-handed circularly-polarized (RHCP) incoming light with photon energy $\hbar\Omega = \delta$ and Jones vector $\boldsymbol{E}_0 = E_0\left(\boldsymbol{e}_x + i\boldsymbol{e}_y\right)/\sqrt{2}$. The matrix element is the dipole moment corresponding to the two transition levels. The matrix element for interband transition corresponding to the band edge modes is calculated as:

$$R_{cv}^{K,K'}(\boldsymbol{k}) = -\frac{2\hbar v_f}{3\sqrt{\beta_{\boldsymbol{k}}^{\tau}}}\begin{pmatrix} i\tau \\ 1 \end{pmatrix}, \tag{2.22}$$

where $\beta_{\boldsymbol{k}}^{\tau} = 4{\mathcal{E}_{c\boldsymbol{k}}^{\tau}}^2$ and $\mathcal{E}_{c\boldsymbol{k}}^{\tau}$ is the band energy. The dipole moment in a certain valley has a specific chirality. If we multiply the vectorial part of $R_{cv}^{K}(\boldsymbol{k})$ and that of the electric field of RHCP light, it comes to $i(1+\tau)$ which yields a finite value at K but zero at K'. Therefore, a right-handed circularly-polarized (RHCP) light with photon energy $\hbar\Omega = \delta$ is only able to interact with electrons residing at K points while LHCP light can interact with another. This so-called circular dichroism is schematically shown in Fig. 2.12(b). Based on this working principle, breaking TRS using 2D material has been demonstrated [50], [55], [56], providing alternative angles to non-reciprocity in the absence of magnetic field. In Ref. [55], TMD is experimentally demonstrated to have valley-selective response pumped by CP light due to the valley-selective exciton population. The Hall conductivity is measured as a good match with the theoretical calculations in Ref. [71]. However, the optical gain is not discussed in the experiment and nonreciprocal responses are somewhat weak.

2.3.2 Quantum Liouville's theorem

In order to understand the optical responses of 2D materials with broken inversion symmetry (here we use gapped graphene) under circularly-polarized light, we need to study the *dynamics* of the carrier distribution. Under the perturbation of external fields, the system will deviate from its thermal equilibrium state. Instead of describing the system with the time-evolving wave functions, the *density matrix* offers comprehensive information about the system especially when wave function fails depicting mixed states. The time-evolution of density matrix is governed by the quantum Liouville's equation, also known as von Neumann equation given, following [57]:

$$i\hbar\partial_t\hat{\rho} = \left[\hat{H} + \hat{V}, \hat{\rho}\right], \tag{2.23}$$

where $\hat{H}$ is the Hamiltonian of gapped graphene shown in Eq. (2.), $\hat{V} = -e\boldsymbol{E}\cdot\boldsymbol{r}$ is the perturbation term from the electromagnetic field, and $\hat{\rho}$ stands for the density operator. Evaluating the above equation in the momentum representation, we can obtain the dynamics of the populations and coherences corresponding to the diagonal and off-diagonal matrix elements, respectively [50]:

$$\begin{aligned}\frac{\partial\rho_{jj'}}{\partial t} + \frac{e}{\hbar}\boldsymbol{E}\cdot\frac{\partial\rho_{jj'}}{\partial\boldsymbol{k}} = -\frac{i}{\hbar}\rho_{jj'}\left[\mathcal{E}_j(\boldsymbol{k}) - \mathcal{E}_{j'}(\boldsymbol{k})\right] + \frac{ie}{\hbar}\boldsymbol{E} \\ \cdot\sum_{j''}\left[\boldsymbol{R}_{jj''}(\boldsymbol{k})\rho_{j''j'} - \rho_{jj''}\boldsymbol{R}_{j''j'}(\boldsymbol{k})\right],\end{aligned} \tag{2.24}$$

where the $j = \{v, \tau\}$ denotes the quantum number. By introducing a phenomenological relaxation time to the population and using rotating wave approximation(RWA) [50], the above equations can be solved for their steady state solutions where a set of four coupled equations are acquired for ρ_c^K, ρ_v^K, $\rho_c^{K'}$ and $\rho_v^{K'}$ corresponding to the distributions in K and K' valleys:

$$\rho_v^\tau = \beta_\tau\left(\rho_v^{eq,\tau} + \gamma\rho_v^{\tau'} + \alpha_K\rho_{v'}^\tau\right), \tag{2.25}$$

where $\rho_v^{eq,\tau}$ stands for the Fermi-Dirac distribution in thermal equilibrium, $\beta_\tau = 1/(1+\alpha_\tau+\gamma)$, $\gamma = \tau_0/\tau_1$ accounts for the intervalley scattering rate with τ_0 and $\tau_1$being the phenomenological carrier relaxation time and intervalley scattering time, and α_K characterizes the interaction strength with the electromagnetic field and is given by

$$\alpha_\tau = \frac{2e^2\tau_0\tau_d|\boldsymbol{E}_0\cdot\boldsymbol{R}_{cv}^\tau|^2}{\hbar^2(\tau_d^2(\omega-\omega_{cv}^\tau)^2+1)}, \tag{2.26}$$

where τ_d is the dephasing time, and $\omega_{cv}^{\tau} = (\mathcal{E}_{c\boldsymbol{k}}^{\tau} - \mathcal{E}_{v\boldsymbol{k}}^{\tau})/\hbar$ is the interband transition energy. Although the acquisition of Eq. (2.25) comes with tedious math derivation and several reasonable approximations, a qualitative understanding of it can be obtained. The steady state solution for the perturbed distribution is the average of distributions that interact with it and the thermal equilibrate state of itself weighted by the corresponding interaction strengths. Under continuous RHCP light pumping, we plotted the electron populations in the upper and lower bands in FBZ along the path from K and K' in Fig. 2.13. We can see that under RCHP light pumping, there is a population imbalance between K and K' valleys, indicating valley-dependent circular dichroism. Notice that the population is rotational symmetric with respect to the Dirac points. The symmetric contour of the carrier population in momentum space, implies that population as a function of momentum can reduce to a function of energy. Similarly, one expects to see a more populated K' valley in graphene if it is illuminated by a LHCP light.

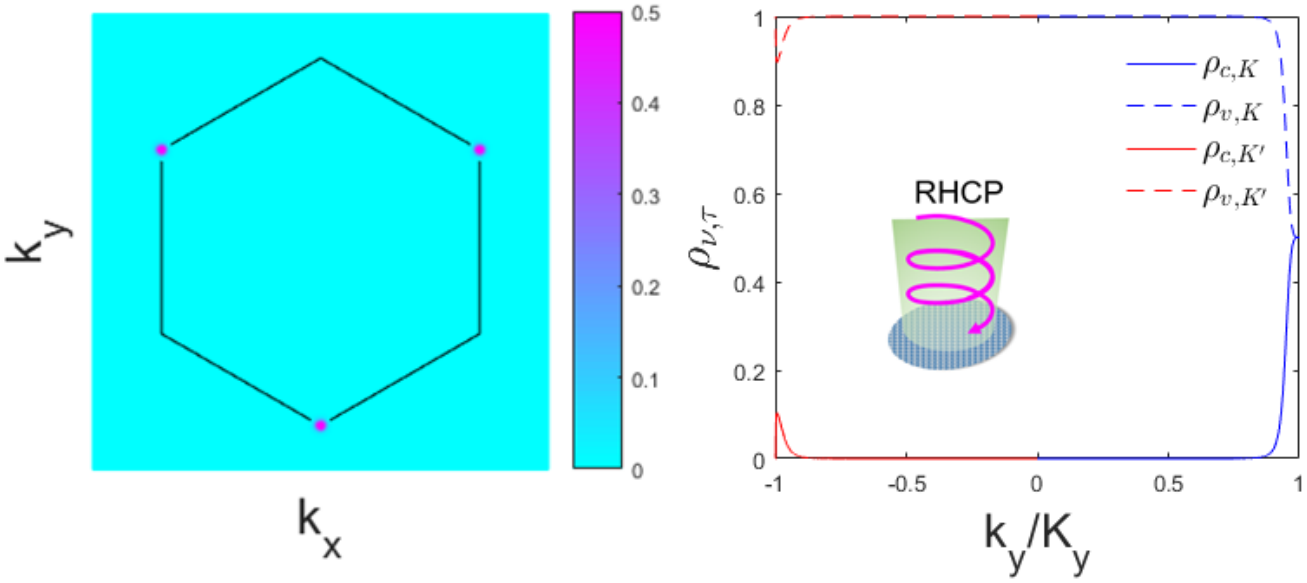

Figure 2.13 (a) Population along the path from K to K' in k-space; (b) Population for the conduction band in the entire FBZ.

2.3.3 Berry curvature and Faraday rotation.

In 1879, E. H. Hall conducted his famous experiment where an electric current was "pressed" to one side of the conductor when subject to a perpendicular magnetic field [58]. Then in his later publication [59], he reported several times larger of this effect in ferromagnetic iron than that in other nonmagnetic materials. This strong effect in ferromagnetic materials discovered by Hall came to be famous as anomalous Hall effect (AHE).

Unique properties were demonstrated in light-driven quantum solids such as photoexcited superconductivity [60], [61] and light-induced topological phases [79], [62], [63]. Under some circumstances, like the one we have mentioned where circularly-polarized light is applied to 2D materials with broken inversion symmetry, anomalous Hall effect can be observed [64], [65]. This is due to the presence of valley-contrasting optical selection and a sizable Berry curvature in gapped Dirac system given by [48]:

$$\Omega_{\tau,\boldsymbol{k}} = \tau \frac{2\hbar^2 v_f^2 \delta}{\left(\delta^2 + 4\hbar^2 v_f^2 k^2\right)^{3/2}}. \tag{2.27}$$

The Berry curvature arises from the adiabatic evolving of Bloch band electrons through a cyclic path, and it behaves just like a pseudomagnetic field acting in the momentum space. Fig. 2.13(a) shows the Berry curvature distribution in the FBZ. Therefore, under electric fields, the electron gains an anomalous velocity transverse to its trajectory. With linear-polarized light the contributions from the two valleys cancel with each other due to the sign change in their Berry curvatures thus showing zero net current. However, with circularly-polarized light pumping, we can observe anomalous Hall effect originated from the population imbalance between the two valleys. To calculate the Hall conductivity (off-diagonal element σ_{xy}) we use the following equation [66]

$$\sigma_{xy} = \frac{2e^2}{\hbar}\int \rho_{c,\tau}(\boldsymbol{k})\Omega_{c,\tau}(\boldsymbol{k})d\boldsymbol{k}, \tag{2.28}$$

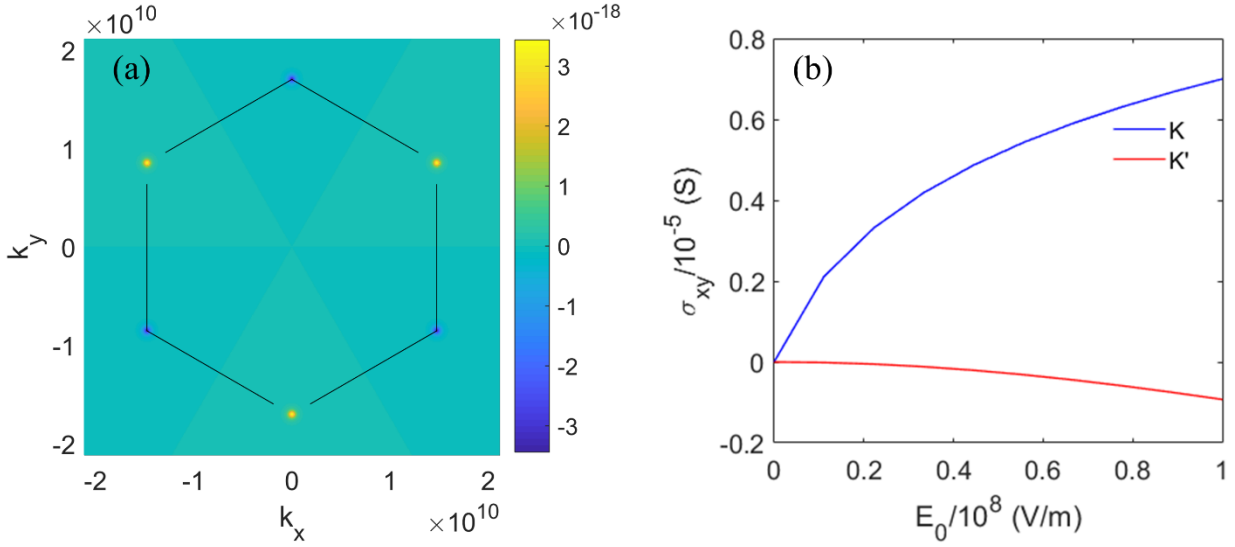

Figure 2.13 (a) Berry curvature for conduction band in FBZ. (b) σ_{xy} for K and K' valleys computed as a function of pumping intensity.

where the factor of 2 accounts for both conduction and valence bands. The contributions from the two K valleys to the DC conductivity are plotted in Fig. 2.13(b) using a pump energy of $\hbar\Omega = \delta$ and with varying intensity. The effectiveness of Kubo formula is also validated by comparing its calculation on σ_{xy} with that of Berry curvature method. Here, using Kubo formula, we also plotted the frequency responses of σ_{xx} and σ_{xy} without pump and under RHCP light pump with electric field $E_0 = 10^8\ V/m$, respectively. We can see that the real and imaginary parts of σ_{xy} vary slightly with frequency due to the dominated interband transitions over intraband transitions within the range we are interested, i.e., $\hbar\omega \ll \Delta$. The diagonal conductivity increases significantly because the near-resonant field at the Dirac points continuously pumps the electrons close to the top of valence band to the bottom of conduction band which saturate that point and energy states nearby. The quasi Fermi energy stays just at the bottom of conduction band. Notice that the laser intensity used to calculate Fig 2.13(b) and 2.14 is high and a large τ_0 is used indicating a high

quality of graphene sheet. Previous approaches present some challenges to calculate the conductivity of optically-pumped graphene. First, as described above, the optical gain and nonreciprocal responses are treated separately. Second, the laser energy is fixed to match the energy gap of the system resulting in a near resonant excitation at the band edges which in practice is very difficult to be satisfied. Third, the relaxation mechanisms are only considered up to a phenomenological level while the full carrier dynamics which would provide a more accurate model is yet not considered. As a result, it is critical to find a comprehensive theoretical frame work enable to calculate the full carrier dynamics and thus population, taken into account essential

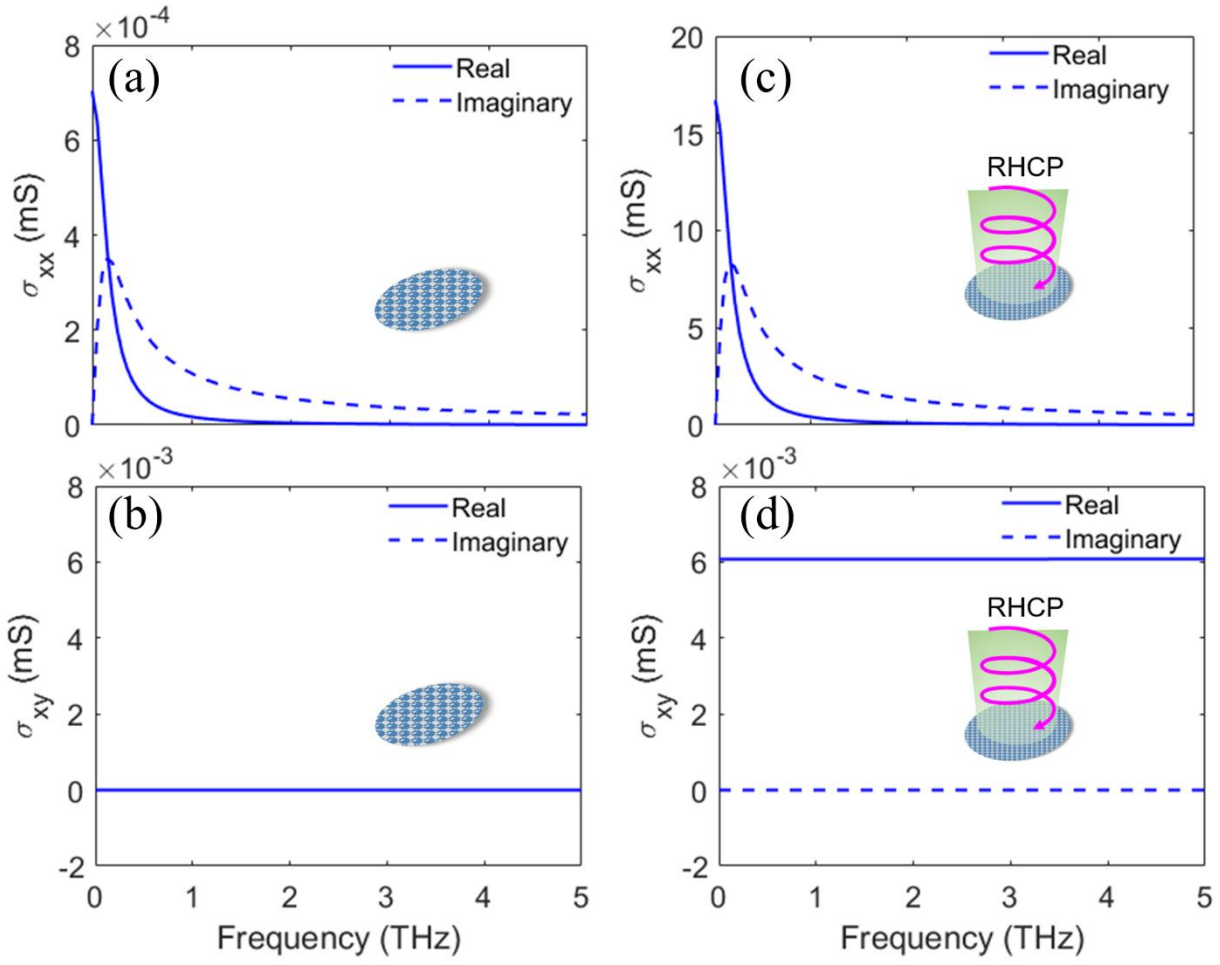

Figure 2.14 Frequency responses of graphene (a), (b) without pump and (c), (d) under RHCP light pump with $E_0 = 10^8\ V/m$ The parameters used are $\tau_0 = \tau_d = 1\ ps$, $E_g = 0.5\ eV$, $\mu_c = 0$.

scattering mechanisms under arbitrary optical excitation for 2D materials not limited to gapped Dirac systems.

2.4 Graphene devices

This section briefly describes some initial cleanroom experiments and testing results towards the graphene Hall devices. The goal of this fabrication process is to develop a chip that acts as a substrate and testbed for high quality graphene. The end goal is to successfully test a four terminal hall effect device for the measurement of both diagonal and off diagonal conductivity in graphene at DC, infrared, and THz. The following section describes the incremental advances made towards achieving this goal and the detailed process that was implemented.

To isolate CVD graphene such that it can be transferred to a target substrate, the wet transfer process was used originally described in reference [69]. The wet transfer process is described in additional detail in many of the experiments [70]-[76]. First, the silicon wafer is cleaned and a layer of silicon dioxide with 150nm thickness is deposited on it using HDPCVD. A lithography process is done to define the electrode area. The exposed area is developed and then deposited with 10nm of Chrome followed by 200nm of gold in an evaporator. The substrate is then soaked in hot acetone for a complete lift-off. Second, the PMMA-recoated hBN and graphene on copper foil are cut into approximately 1×1 mm^2 square pieces. They are floated and bathed in ammonium sulfate solution under 60 degrees for about 1 hour to fully remove the copper. The PMMA-supported 2D materials are then transferred into DI water dishes for three times until external impurities from the copper or the solution are largely eliminated. The chip made in the first step is diced into individual transistor devices and ozone treated for 150 seconds before the transfer of 2D materials. This treatment can make sure the blank device surface is hydrophilic so that it is easy to scoop 2D materials. Finally, the hBN is scooped out first and manipulated by

tweezers to the channel region. The devices are naturally dried overnight and then heated on hotplate with 150 degrees. They are put into acetone/IPA/DI water dishes to fully remove the PMMA. The devices are the used to scoop the graphene out followed by the same drying and heat cure procedures. The devices are wire-bonded using a ball bonder. The surface can be hydrophobic again after several times organic immersion, so it is suggested to be the bonding after another ozone treatment of 90 seconds. The device can be further annealed in a vacuum oven with nitrogen atmosphere under 220 degrees for 4 hours to remove more impurities and improve performance. We use the diamond cutter to scratch one corner of the device piece to expose the silicon surface for gate probe. The process is schematically illustrated in Fig. 2.15. Final devices are either tested by probing or wire-bonded to PCBs. The wire-bonded device and the electrode configuration are shown in Fig. 2.16.

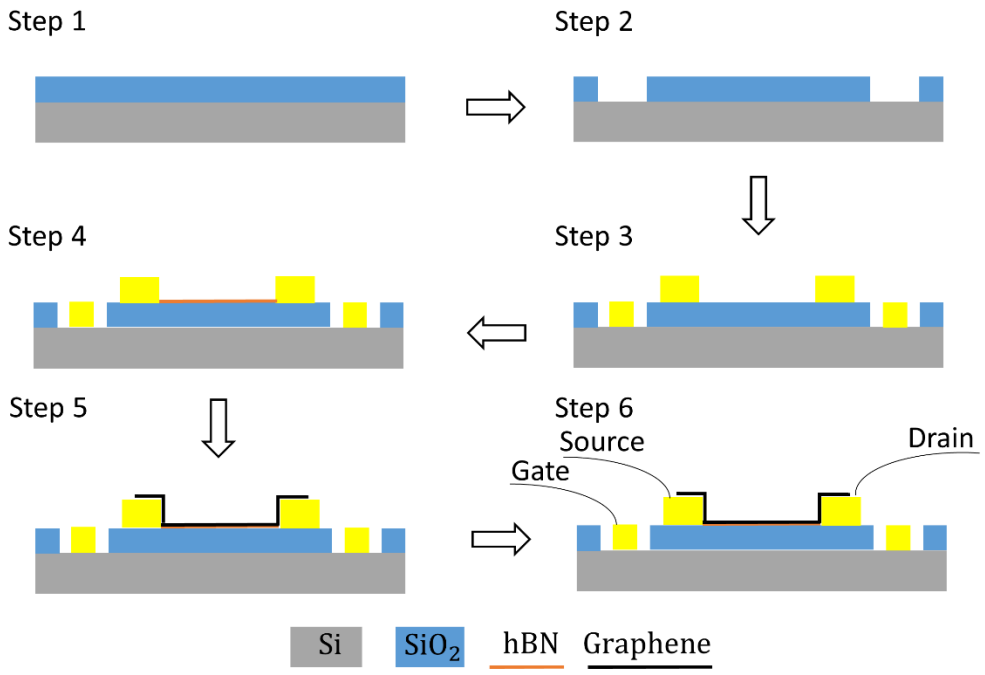

Figure 2.15 Graphene device fabrication process. Step 1: PECVD deposition of silicon oxide. Step 2: Electrodes deposition using gold E-beam evaporation. Step 3: Wet transfer of hBN and removal of PMMA. Step 4: Wet transfer of graphene. Step 5: Scatch off oxide to expose silicon for gating. Step 6: Wirebonding to electrode for desired measurement.

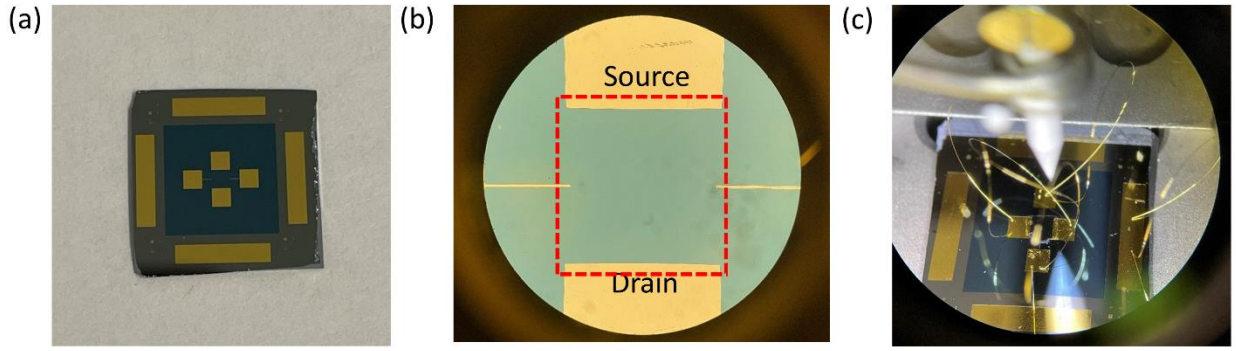

Figure 2.16 (a) Device image with source and drain and two side electrodes and four gate contacts. (b) A zoomed in microscope image in the channel region with the red dashed frame showing the graphene. (c) Wire-bonded graphene device.

When graphene is supported by silicon dioxide as a substrate, the carrier mobility is limited due to scattering from surface states, impurities, substrate surface roughness, and silicon dioxide surface phonons [77]. Hexagonal Boron Nitride (hBN) has a similar hexagonal lattice to graphene (1.7% lattice mismatch), is inert and insulating, and has no dangling bonds. and provide an excellent dielectric substrate for graphene [77]. The I_d-V_g tests of graphene devices with/without hBN are plotted in Fig. 2.17, the current is getting significantly increased due to the presence of

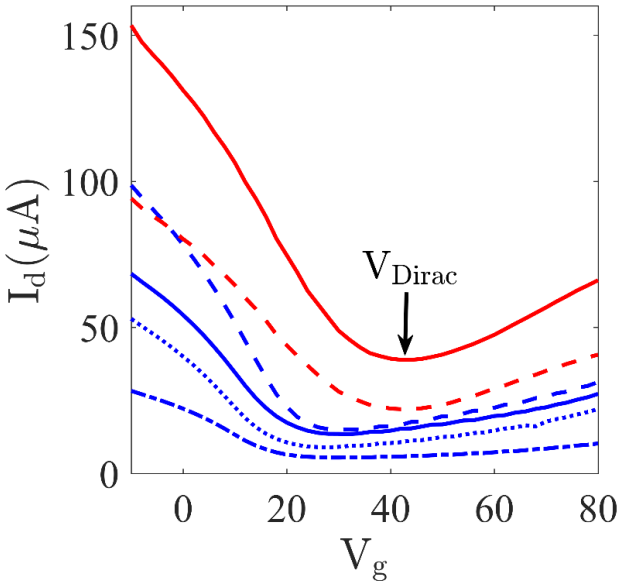

Figure 2.17 Graphene transconductance measurement showing Dirac point. The red/blue lines show the devices with and without hBN. The hBN/graphene devices show much higher current and better resolved Dirac point.

hBN as an layer of isolation from the substrate. One of the best performed devices is plotted in Fig. 2.18 together with its mobility calculated following Bolotin's method [78]. The result shows that a mobility of around 2500 is obtained which is reasonably good considering the larger area CVD graphene used in the experiment.

2.5 Conclusions and future work

This chapter builds up a powerful theoretical framework based on Kubo formalism which is able to calculate the optical conductivity of graphene either with or without optical pump and even under other perturbations such as strain field. Specifically, the optical conductivity of gapped graphene is calculated using the population obtained from evaluating the quantum Liouville's equation. The response is shown to match that obtained from calculated from Berry curvature.

There are several on-going research lines that appeared as a result of this work and that are currently being explored by our group. The goal of the remainder of this section is to describe such efforts. On the theory part, we propose to use the quantum Liouville's theorem, specifically, the von Neumann equation, to study the temporal evolution of the carrier population with explicit form of some relaxation mechanisms such as optical phonons. Our goal is to adapt this formalism to

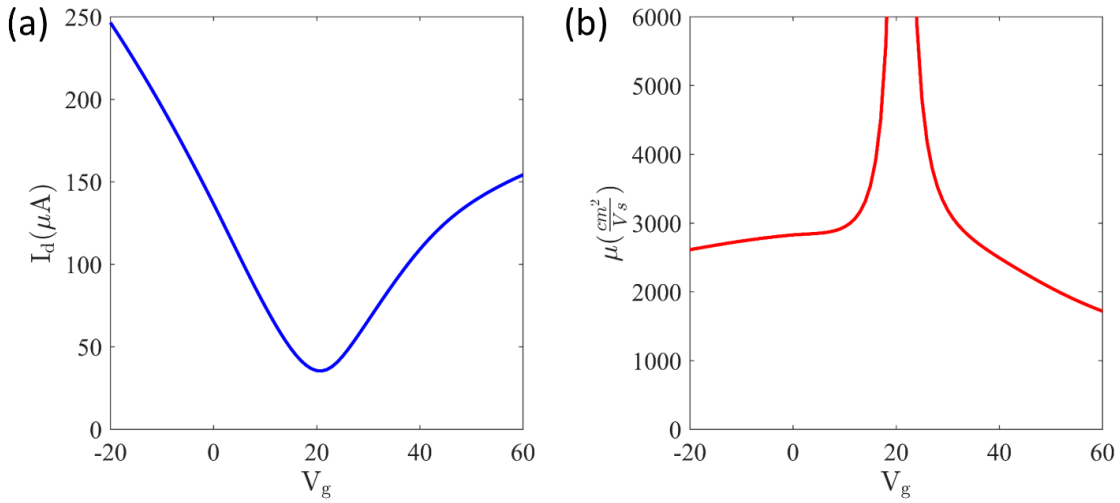

Figure 2.18 (a) The best performed devices after annealing with a Dirac voltage at around 20 V. (b) The mobility calculated using Bolotin's method.

determine the properties of inverted carrier populations (i.e., gain) and nonreciprocal responses versus the properties of the incoming circularly polarized light pumps. For the experimental part, the final objective is to validate theoretical results using a THz TDS equipment and to demonstrate active, nonreciprocal THz components.

2.5.1 Future work: Theory

In laboratory, lasers are powerful light sources commonly used for optical pumping. Previous theoretical works on CP light pumped graphene only focused on revealing nonreciprocal responses [71], [72] and assumed certain restrictions on the laser energy. However, lasers feed intensive energy to graphene and it is important to determine if nonreciprocal responses get amplified under this scheme as illustrated in Fig. 2.19. Being one of the most efficient relaxation mechanisms, electron-phonon coupling (EPC), the process of energy and momentum exchange between photogenerated electrons and optical phonons, is enough to invert the population near the Dirac points even under weak pumping intensities [62], [67]. Here, we reformulate Eq. 2.29 in the case of conduction band population and add general scattering events [33]:

$$\partial\rho \quad e \quad \partial\rho$$

$$+\frac{ie}{\hbar}\boldsymbol{E}\cdot \qquad\qquad \iota t\rho_{cc}, \tag{2.29}$$

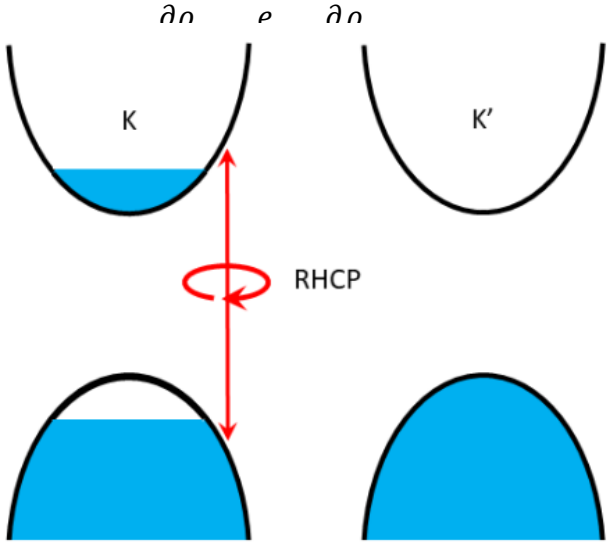

Figure 2.19 Schematic showing inverted population.

where the scattering rate $\Gamma_{\boldsymbol{k}}^{in/out}$ accounts for all possible mechanisms including C-C scatterings, optical phonons, which will enable the photoexcited carriers to relax and accumulate at lower energy levels. The possible relaxation mechanisms are schematically shown in Fig. 2.20(a). Previous approaches only used a phenomenological relaxation time τ, and thus they are not able to capture carrier relaxation from highly populated energy levels to lower, under-occupied energy levels. Therefore, these approaches cannot capture phenomena such as optical gain. Due to the lack of DOS near the bottom of the conduction band and a relatively slow interband recombination rate, it is possible for photoexcited carriers to have population inversion through the momentum and energy exchange with other scattering agents. The ultimate goal of this on-going theoretical work is to develop a comprehensive formalism able to calculate the frequency-dependent graphene

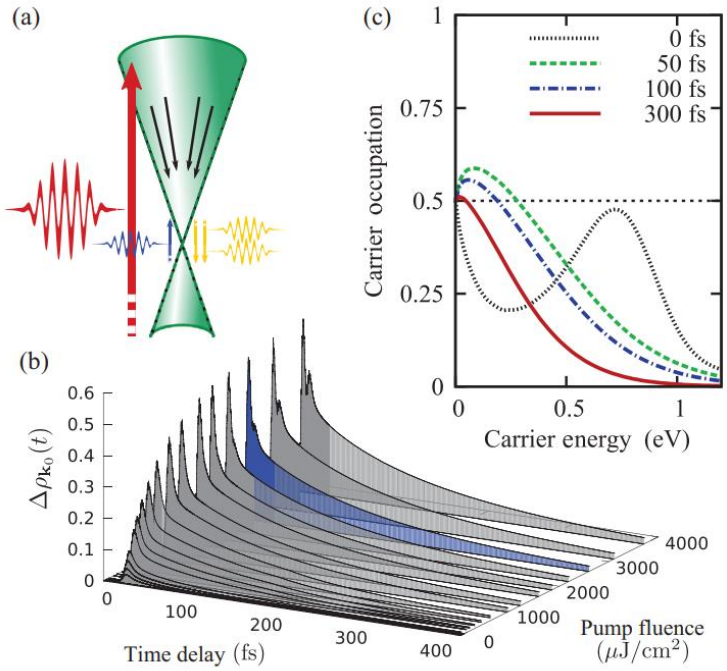

Figure 2.20 (a) Schematic of optical pumping and carrier relaxation and accumulation. (b) Time evolution of population at the excited energy level as functions of time and pump fluence. (c) Time evolution in conduction band at several moments. Figures reproduced from [33].

conductivity tensor versus the features of the incoming light in terms of intensity, energy, and polarization, thus unveiling active nonreciprocal responses at THz and IR frequencies.

Once the formalism is completed, it will be applied to investigate resonant-like configurations and metasurface to boost and manipulate nonreciprocal responses while amplifying terahertz signals, thus addressing one of the major bottlenecks of current technology.

2.5.2 Future work: Experiments

The ultimate goal of this on-going experiment is to measure the Faraday rotation of terahertz waves with possible optical gain after passing through graphene samples pumped by circularly polarized laser beam. To this purpose, we will fabricate two different types of graphene samples. The first sample is a pristine graphene layer. The graphene sample will be fabricated starting with depositing CVD grown graphene sheet on dielectric layer grown on silicon wafer. Metallic electrodes will be fabricated on top of graphene sample. The second case is a nanopatterned graphene sample which can provide a large local field enhancement at 780 nm of the incident laser. Several configurations, including strip, patches, and bow-type resonators will be explored.

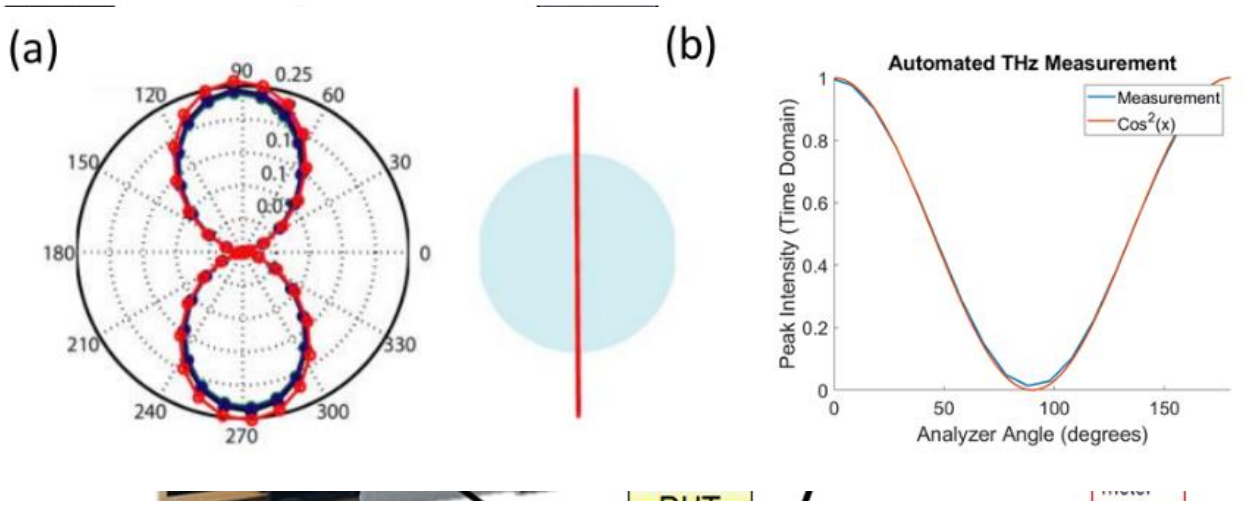

Figure 2.23 (a) Extraction of rotation angle by fitting of data and Malus's law [52]. (b) Test of attenuation of THz beam by rotating analyzer (LP2).

Figure 2.22 Current experimental setup.

The proposed experiment setup is schematically depicted in Fig. 2.21. A picture showing the on-going setup is shown in Fig. 2.22. The graphene sample is pumped by a circularly polarized light from the side which only offsets slightly from the optic axis. The THz emitter together with linearly polarizer (LP1) creates a linearly polarized terahertz wave is then focused onto the graphene on dielectric sample. Note that the focused beam must be smaller than the pump beam. The transmitted beam is then collimated to pass the second linearly polarizer (LP2) and received and processed by the spectrometer. Both LP1 and LP2 are mounted on mechanical rotators controlled by Matlab program. Both can rotate 360° with a precision of 0.05°. LP1 and LP2 are collimated before experiment to guarantee maximum signal to be received by the receiver without placing the sample. We presume that the incident terahertz is subject to a polarization rotation by the sample thus there will be an off-axis (polarization of LP1) angle corresponding to θ_i that we need to measure. To retrieve the Faraday rotation, we will apply the so-call Malus's law [52], which reads:

$$I = I_0 cos^2\theta_i, \tag{2.30}$$

where I_0 is the intensity of the incoming linearly polarized light and θ_i is the rotation angle of polarization after transmitted through an analyzer. The law dictates that when completely linearly polarized light is impinging on the analyzer, the intensity I of the transmitted light is proportional to the square of $\cos\theta_i$. The extraction of this angle is illustrated in Fig. 2.23(a). By rotating LP2, we can plot the transmitted beam power at the receiver versus the rotation angle of LP2. According to Malus's law, there will be two peaks because of the cosine square relation. Then one can fit the measured power plot with that calculated from Eq. 2.30. The attenuation of THz signal according to Malus's law and the fitting are plotted in Fig. 2.23(b) within half a circle using our experiment setup. If there is no rotation after transmission, the peaks should be located at 0° and 180°. But when there is rotation, the peaks will deviate from the original direction in which LP1 and LP2 are polarized. The measured Faraday rotation will be compared and matched with COMSOL Multiphysics simulations and our theoretical prediction. If the terahertz wave cannot be captured and the experiment is unsuccessful, a backup plan will be an IR measurement using the signal generated by an FTIR system. Another experiment is to time resolve the transient carrier dynamics within the relaxation time scale using the lock-in amplifier. The laser beam path will send a linearly/circularly polarized light upon graphene sample and the photoinduced carriers will be collected and read by a transimpedance amplifier and a lock-in amplifier. This experiment will help us understand and identify intraband and interband transitions and various types of relaxation mechanisms.

2.6 Chapter references

[1] Correas-Serrano, D., and J. S. Gomez-Diaz. "Nonreciprocal and collimated surface plasmons in drift-biased graphene metasurfaces." Physical Review B 100.8 (2019): 081410.

[2] Morgado, Tiago A., and Mário G. Silveirinha. "Negative Landau damping in bilayer graphene." *Physical review letters* 119.13 (2017): 133901.

[3] Morgado, Tiago A., and Mário G. Silveirinha. "Drift-induced unidirectional graphene plasmons." *ACS Photonics* 5.11 (2018): 4253-4258.

[4] Novoselov, Kostya S., et al. "Electric field effect in atomically thin carbon films." *science* 306.5696 (2004): 666-669.

[5] Hanson, George W. "Dyadic Green's functions and guided surface waves for a surface conductivity model of graphene." *Journal of Applied Physics* 103.6 (2008).

[6] Motlagh, S. Azar Oliaei, et al. "Ultrafast optical currents in gapped graphene." *Journal of Physics: Condensed Matter* 32.6 (2019): 065305.

[7] Nevius, M. S., et al. "Semiconducting graphene from highly ordered substrate interactions." *Physical review letters* 115.13 (2015): 136802.

[8] Jariwala, Deep, Anchal Srivastava, and Pulickel M. Ajayan. "Graphene synthesis and band gap opening." *Journal of nanoscience and nanotechnology* 11.8 (2011): 6621-6641.

[9] Geim, Andre K., and Irina V. Grigorieva. "Van der Waals heterostructures." Nature 499.7459 (2013): 419-425.

[10] Huang, Y. H., et al. "Transport properties in semiconducting NbS2 nanoflakes." Applied Physics Letters 105.9 (2014): 093106.

[11] Reich, Stephanie, Christian Thomsen, and Janina Maultzsch. *Carbon nanotubes: basic concepts and physical properties*. John Wiley & Sons, 2008.

[12] Kretinin, A., et al. "Quantum capacitance measurements of electron-hole asymmetry and next-nearest-neighbor hopping in graphene." Physical Review B 88.16 (2013): 165427.

[13] Leggett, A. "Lecture 5. Graphene: Electronic band structure and Dirac fermions." Physics 769. Selected topics in condensed matter physics (2010).

[14] Rostami, H., and Reza Asgari. "Electronic ground-state properties of strained graphene." Physical Review B 86.15 (2012): 155435.

[15] Tamagnone, Michele. Theory, design and measurement of near-optimal graphene reconfigurable and non-reciprocal devices at terahertz frequencies. No. THESIS. EPFL, 2016.

[16] Hanson, George W. "Dyadic Green's functions for an anisotropic, non-local model of biased graphene." *IEEE Transactions on antennas and propagation* 56.3 (2008): 747-757.

[17] Low, Tony, et al. "Tunable optical properties of multilayer black phosphorus thin films." *Physical Review B* 90.7 (2014): 075434.

[18] Correas-Serrano, D., et al. "Black phosphorus plasmonics: anisotropic elliptical propagation and nonlocality-induced canalization." *Journal of Optics* 18.10 (2016): 104006.

[19] Peres, N. M. R., and Eduardo V. Castro. "Algebraic solution of a graphene layer in transverse electric and perpendicular magnetic fields." Journal of Physics: Condensed Matter 19.40 (2007): 406231.

[20] Hebborn, J. E., and E. H. Sondheimer. "The diamagnetism of conduction electrons in metals." *Journal of Physics and Chemistry of Solids* 13.1-2 (1960): 105-123.

[21] Sounas, Dimitrios L., and Christophe Caloz. "Novel Electromagnetic Phenomena in Graphene and Subsequent Microwave Devices Enabled by Multi-Scale Metamaterials." *Metamaterial*. IntechOpen, 2012.

[22] Martin, Thomas. "Faraday's diary." (1932): 812-814.

[23] Tamagnone, Michele, et al. "Magnetoplasmonic enhancement of Faraday rotation in patterned graphene metasurfaces." Physical Review B 97.24 (2018): 241410.

[24] Slipchenko, Tetiana M., et al. "H." *Physical Review Research* 1.3 (2019): 033049.

[25] Levy, N., et al. "Strain-induced pseudo–magnetic fields greater than 300 tesla in graphene nanobubbles." *Science* 329.5991 (2010): 544-547.

[26] Rana, Farhan. "Graphene terahertz plasmon oscillators." IEEE Transactions on Nanotechnology 7.1 (2008): 91-99.

[27] Wendler, Florian, and Ermin Malic. "Towards a tunable graphene-based Landau level laser in the terahertz regime." Scientific reports 5.1 (2015): 1-7.

[28] Otsuji, Taiichi, et al. "Graphene-based devices in terahertz science and technology." Journal of Physics D: Applied Physics 45.30 (2012): 303001.

[29] Wen, Qi-Ye, et al. "Graphene based all-optical spatial terahertz modulator." Scientific reports 4.1 (2014): 1-5.

[30] Fan, Yuancheng, et al. "Graphene plasmonics: a platform for 2D optics." Advanced Optical Materials 7.3 (2019): 1800537.

[31] Tomadin, Andrea, et al. "The ultrafast dynamics and conductivity of photoexcited graphene at different Fermi energies." Science advances 4.5 (2018): eaar5313.

[32] Jago, Roland, et al. "Graphene as gain medium for broadband lasers." Physical Review B 92.8 (2015): 085407.

[33] Winzer, Torben, Ermin Malić, and Andreas Knorr. "Microscopic mechanism for transient population inversion and optical gain in graphene." Physical Review B 87.16 (2013): 165413.

[34] Karasawa, Hiromi, et al. "Observation of amplified stimulated terahertz emission from optically pumped heteroepitaxial graphene-on-silicon materials." Journal of Infrared, Millimeter, and Terahertz Waves 32.5 (2011): 655-665.

[35] Low, Tony, Pai-Yen Chen, and D. N. Basov. "Superluminal plasmons with resonant gain in population inverted bilayer graphene." Physical Review B 98.4 (2018): 041403.

[36] Tasolamprou, Anna C., et al. "Experimental demonstration of ultrafast THz modulation in a graphene-based thin film absorber through negative photoinduced conductivity." ACS photonics 6.3 (2019): 720-727.

[37] Chen, Pai-Yen, and Jeil Jung. "P t symmetry and singularity-enhanced sensing based on photoexcited graphene metasurfaces." Physical Review Applied 5.6 (2016): 064018.

[38] Fan, Yuancheng, et al. "Photoexcited graphene metasurfaces: significantly enhanced and tunable magnetic resonances." Acs Photonics 5.4 (2018): 1612-1618.

[39] Guo, Tianjing, et al. "Tunable terahertz amplification based on photoexcited active graphene hyperbolic metamaterials." Optical Materials Express 8.12 (2018): 3941-3952.

[40] Veldhorst, M., et al. "Silicon CMOS architecture for a spin-based quantum computer." *Nature communications* 8.1 (2017): 1-8.

[41] Boubanga-Tombet, S., et al. "Ultrafast carrier dynamics and terahertz emission in optically pumped graphene at room temperature." *Graphene-Based Terahertz Electronics and Plasmonics*. Jenny Stanford Publishing, 2020. 539-554.

[42] Karasawa, Hiromi, et al. "Observation of amplified stimulated terahertz emission from optically pumped heteroepitaxial graphene-on-silicon materials." *Journal of Infrared, Millimeter, and Terahertz Waves* 32 (2011): 655-665.

[43] Ryzhii, Victor, M. Ryzhii, and Taiichi Otsuji. "Negative dynamic conductivity of graphene with optical pumping." *Journal of Applied Physics* 101.8 (2007).

[44] Yao, Wang, Di Xiao, and Qian Niu. "Valley-dependent optoelectronics from inversion symmetry breaking." *Physical Review B* 77.23 (2008): 235406.

[45] Song, Justin CW, and Mark S. Rudner. "Chiral plasmons without magnetic field." *Proceedings of the National Academy of Sciences* 113.17 (2016): 4658-4663.

[46] Marchukov, Oleksandr V., et al. "Quantum spin transistor with a Heisenberg spin chain." *Nature communications* 7.1 (2016): 1-6.

[47] Chen, Lan, Peng Cheng, and Kehui Wu. "Quasiparticle interference in unconventional 2D systems." Journal of Physics: Condensed Matter 29.10 (2017): 103001.

[48] Mrudul, M. S., et al. "Light-induced valleytronics in pristine graphene." Optica 8.3 (2021): 422-427.

[49] Zeng, Hualing, et al. "Valley polarization in MoS 2 monolayers by optical pumping." Nature nanotechnology 7.8 (2012): 490-493.

[50] Kumar, Anshuman, et al. "Chiral plasmon in gapped Dirac systems." *Physical Review B* 93.4 (2016): 041413.

[51] Xu, Xiaodong, et al. "Spin and pseudospins in layered transition metal dichalcogenides." Nature Physics 10.5 (2014): 343-350.

[52] Dey, Prasenjit, et al. "Gate-controlled spin-valley locking of resident carriers in WSe 2 monolayers." Physical review letters 119.13 (2017): 137401.

[53] Warner, A. W., D. L. White, and W. A. Bonner. "Acousto-optic light deflectors using optical activity in paratellurite." Journal of Applied Physics 43.11 (1972): 4489-4495.

[54] Motlagh, S. Azar Oliaei, et al. "Ultrafast optical currents in gapped graphene." Journal of Physics: Condensed Matter 32.6 (2019): 065305.

[55] Kawaguchi, Yuma, et al. "All-optical nonreciprocity due to valley polarization in transition metal dichalcogenides." *arXiv preprint arXiv:2007.14934* (2020).

[56] Xiao, Di, et al. "Coupled spin and valley physics in monolayers of MoS 2 and other group-VI dichalcogenides." *Physical review letters* 108.19 (2012): 196802.

[57] Breuer, Heinz-Peter, and Francesco Petruccione. *The theory of open quantum systems*. Oxford University Press on Demand, 2002.

[58] Hall, Edwin H. "On a new action of the magnet on electric currents." *American Journal of Mathematics* 2.3 (1879): 287-292.

[59] Hall, E. H. "On the" rotational coefficient" in nickel and cobalt." *Proceedings of the Physical Society of London* 4.1 (1880): 325.

[60] Hart, Oliver, et al. "Steady-state superconductivity in electronic materials with repulsive interactions." *Physical Review B* 100.6 (2019): 060508.

[61] Goldstein, Garry, Camille Aron, and Claudio Chamon. "Photoinduced superconductivity in semiconductors." *Physical Review B* 91.5 (2015): 054517.

[62] Sato, S. A., et al. "Microscopic theory for the light-induced anomalous Hall effect in graphene." *Physical Review B* 99.21 (2019): 214302.

[63] Oka, Takashi, and Hideo Aoki. "Photovoltaic Hall effect in graphene." *Physical Review B* 79.8 (2009): 081406.

[64] Xiao, Di, Wang Yao, and Qian Niu. "Valley-contrasting physics in graphene: magnetic moment and topological transport." *Physical Review Letters* 99.23 (2007): 236809.

[65] Yao, Wang, Di Xiao, and Qian Niu. "Valley-dependent optoelectronics from inversion symmetry breaking." *Physical Review B* 77.23 (2008): 235406.

[66] Xiao, Di, et al. "Coupled spin and valley physics in monolayers of MoS 2 and other group-VI dichalcogenides." Physical review letters 108.19 (2012): 196802.

[67] Low, Tony, et al. "Cooling of photoexcited carriers in graphene by internal and substrate phonons." Physical Review B 86.4 (2012): 045413.

[68] Satou, A., F. T. Vasko, and V. Ryzhii. "Nonequilibrium carriers in intrinsic graphene under interband photoexcitation." *Physical Review B* 78.11 (2008): 115431.

[69] Reina, Alfonso, et al. "Large area, few-layer graphene films on arbitrary substrates by chemical vapor deposition." *Nano letters* 9.1 (2009): 30-35.

[70] Wang, Feng, et al. "Gate-variable optical transitions in graphene." *science* 320.5873 (2008): 206-209.

[71] Gomez-Diaz, J. S., et al. "Self-biased reconfigurable graphene stacks for terahertz plasmonics." *Nature communications* 6.1 (2015): 6334.

[72] De Fazio, Domenico, et al. "High-mobility, wet-transferred graphene grown by chemical vapor deposition." *ACS nano* 13.8 (2019): 8926-8935.

[73] Wang, S., et al. "Photocurrent generation of a single-gate graphene p–n junction fabricated by interfacial modification." *Nanotechnology* 26.38 (2015): 385203.

[74] Kobayashi, Shiho, et al. "Photoresponse of graphene field-effect-transistor with n-type Si depletion layer gate." *Scientific reports* 8.1 (2018): 1-9.

[75] Heyman, J. N., et al. "Carrier heating and negative photoconductivity in graphene." *Journal of Applied Physics* 117.1 (2015).

[76] Shi, S-F., et al. "Controlling graphene ultrafast hot carrier response from metal-like to semiconductor-like by electrostatic gating." *Nano letters* 14.3 (2014): 1578-1582.

[77] Dean, Cory R., et al. "Boron nitride substrates for high-quality graphene electronics." *Nature nanotechnology* 5.10 (2010): 722-726.

[78] Bolotin, Kirill I., et al. "Ultrahigh electron mobility in suspended graphene." *Solid state communications* 146.9-10 (2008): 351-355.

3. Graphene in strain fields

In this chapter, we delve into the examination of strain effects on graphene. Our focus lies in the exploration of both uniform and non-uniform strains applied to graphene. In the context of uniform strain, we introduce the strain tensor and the Hamiltonian by leveraging a combination of tight-binding models and linear elastic theory. We also present an analysis of lattice distortion under various types of uniform strain, providing a specific example with the calculation of the displacement of Dirac points for armchair uniaxial strain. Furthermore, we calculate the optical conductivity of uniformly-strained graphene. Moving on, we study the intriguing realm of non-uniform strain within graphene. We focus into the band structure, density of states, and the causal relationship that links lattice displacement to a pseudomagnetic field in graphene. This comprehensive exploration lays the foundation for the forthcoming chapter, where we aim to manipulate nonreciprocity in graphene by combining optical pumping and non-uniform strain.

3.1 Introduction

Recently, there has been extensive interest in the use of graphene electronics [1], thermal, and transport properties [3] upon mechanical deformation for the development of new photonic and IR applications [4], [5]. Graphene provides a relatively large mechanical tunability – owing to a noteworthy 25% strain which a monolayer graphene can withstand without breaking [5]. Remarkably, both theoretical and experimental investigations have revealed the existence of strain-induced pseudomagnetic fields in graphene. As large as 300 Tesla magnetic field was measured using scanning tunneling microscopy on graphene nanobubbles at the nanoscale [6]. The demonstration of such extreme pseudomagnetic, localized, field embraces the possibility of studying carrier dynamics in high magnetic field regimes which were previously inaccessible. Additionally, it has been shown that designed non-uniform strain or strain gradient can generate

uniform pseudomagnetic fields exceeding 10 Tesla [7]. A report also shows stretching along graphene's three crystallographic directions can create measurable large-scale uniform pseudomagnetic field near the center of the deformation [8]. This suggests a facile approach to launch uniform pseudomagnetic field distributions with profiled surfaces. In general, all these strain-induced homogeneous pseudomagnetic fields exhibit positive/negative responses on localized regions that cancel out when the entire physical geometry is considered. As a result, strain engineering is unable to break time-reversal symmetry.

3.2 Graphene in uniform strain fields

3.2.1 Lattice distortion

In mechanics, the deformation of a body subject to external forces is usually characterized by the mechanical strain [9]. In 2D materials, the strain is represented mathematically by a 2×2 tensor:

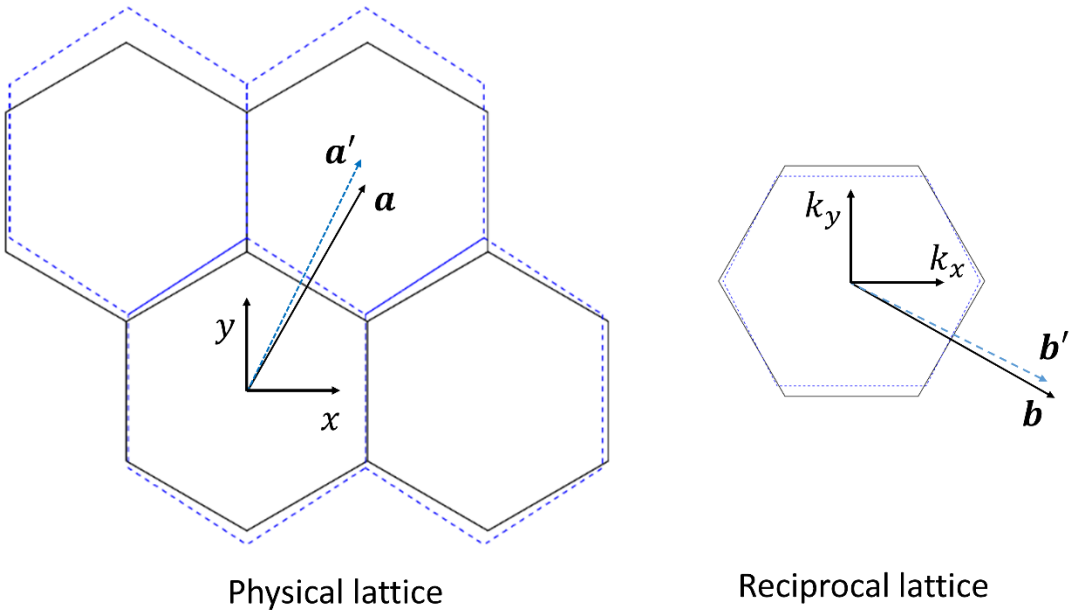

Figure 3.1 Vector deformation in physical lattice and reciprocal lattice in graphene under an armchair uniaxial strain.

$$\boldsymbol{\epsilon} = \begin{pmatrix} \epsilon_{xx} & \epsilon_{xy} \\ \epsilon_{yx} & \epsilon_{yy} \end{pmatrix}. \tag{3.1}$$

In the specific case of graphene, its bond lengths are subject to change under strain. If $\boldsymbol{a}$ represents a generally vector in the physical lattice (see Fig. 3.1(a)), then its strained counterpart becomes $\boldsymbol{a}' = (\boldsymbol{I} + \boldsymbol{\epsilon}) \cdot \boldsymbol{a}$, where $\boldsymbol{I}$ is the identity matrix. Several lattice transformations (blue dashed lines) under various types of strain are plotted in Fig. 3.2(a) considered a strain strength of $\epsilon = 10\%$. The figure also shows the undistorted lattices (black solid lines) as a reference. Correspondingly, a general vector $\boldsymbol{b}$ in the reciprocal space (see Fig. 3.1(b)) suffers a transformation governed by $\boldsymbol{b}' = (\boldsymbol{I} + \boldsymbol{\epsilon})^{-1} \cdot \boldsymbol{b}$. The Brillouin zone is bounded by the lines bisecting the reciprocal lattice vectors. The six vertexes of the distorted FBZ are called high-symmetry points (HSP). Fig. 3.2(b) shows the distorted (blue dashed lines) and undistorted (black solid lines) FBZ. It is important to note that HSPs redefine the limits of the FBZ.

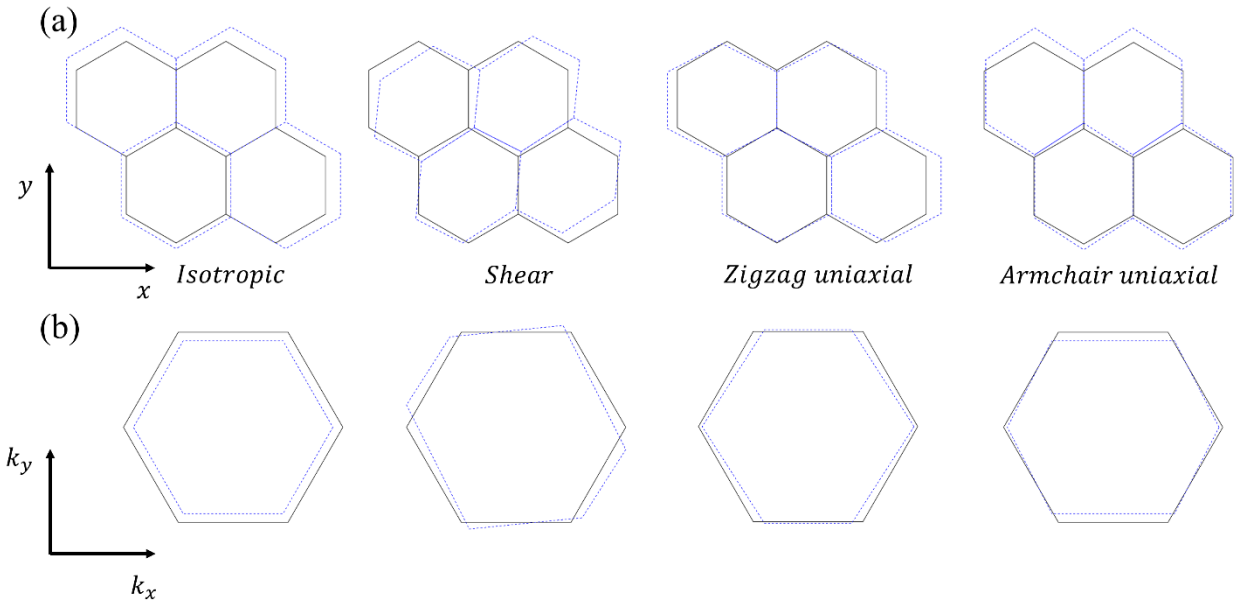

Figure. 3.2 (a) Lattice distortion and (b) reciprocal lattice distortion under four different types of strain. $\epsilon = 10\%$ and Poisson's ratio is $\upsilon = 0.165$.

An immediate consequence after applying strain on graphene is the change of hopping energy which follows an exponential decay [10]:

where $\beta = -\partial lnt/\partial lna$ is called the Grüneisen parameter describing the relative change of hopping energy with respect to the bond length, $\boldsymbol{\delta}'_n = (\boldsymbol{I} + \boldsymbol{\epsilon}) \cdot \boldsymbol{\delta}_n$ are the strained hopping vectors and n runs over all three bonds connecting to the nearest carbon atoms. Then the strained graphene Hamiltonian can be written as [10]:

$$\widehat{H}_s = -\sum_{n=1}^{3} t'_n \begin{pmatrix} 0 & e^{-i\boldsymbol{k}\cdot\boldsymbol{\delta}'_n} \\ e^{i\boldsymbol{k}\cdot\boldsymbol{\delta}'_n} & 0 \end{pmatrix}. \tag{3.3}$$

Solving equation $\mathcal{E}(\boldsymbol{k}) = \left|\sum_{n=1}^{3} t'_n e^{-i\boldsymbol{k}\cdot\boldsymbol{\delta}'_n}\right| = 0$ one can find local extrema of bands which are the Dirac points, as they exhibit zero energy points in the band structure for gapless graphene. Surprisingly, the Dirac points in strained graphene shift away from the HSPs whereas they coincide in unstrained graphene, as shown schematically in Fig. 3.3. This evokes the impact on charge carriers caused by a magnetic field B applied perpendicularly to the graphene plane. As a case

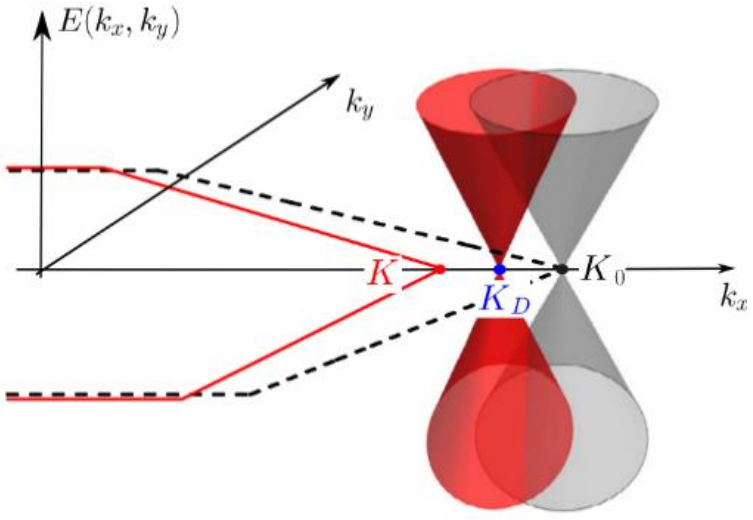

Figure 3.3 The distorted HSP, Dirac point and the Dirac cone. Reproduced from [11].

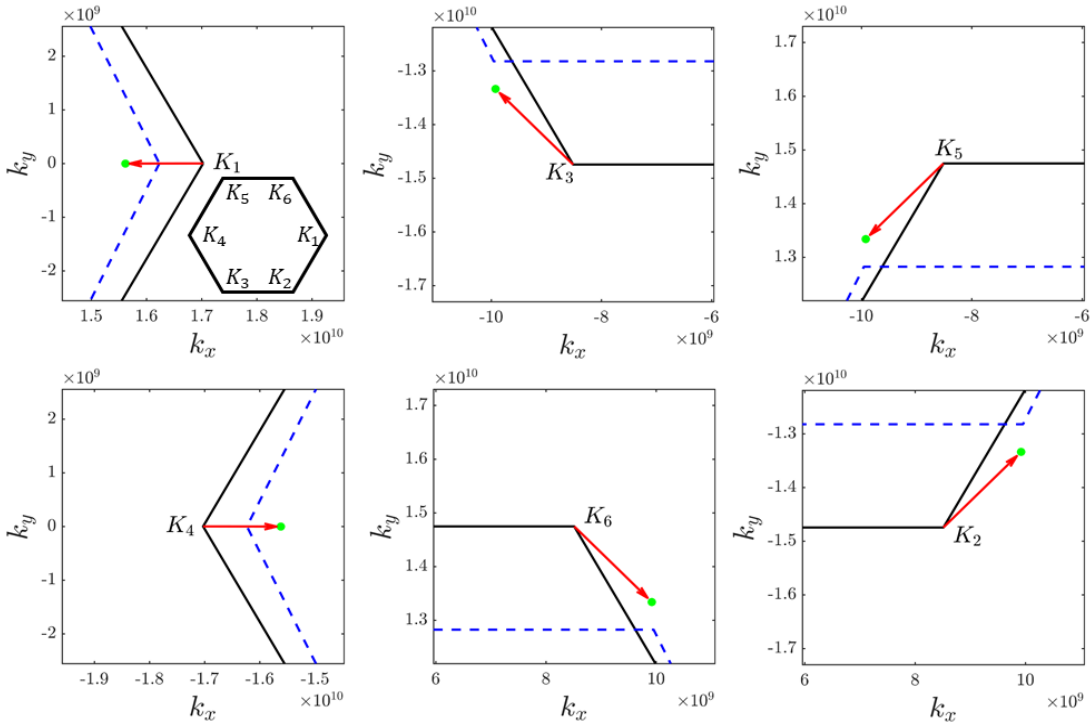

Figure. 3.4 Unstrained (black solid) and strained (blue dashed) FBZ, strained Dirac points (green dots) and displacement of Dirac points (red arrows). The strain type is Armchair uniaxial strain with a magnitude of 5%.

study, we plotted the distorted FBZ and the calculated Dirac points in Fig. 3.4 for armchair uniaxial strain.

3.2.2 Optical conductivity of uniformly strained graphene

The optical conductivity of uniformly strained graphene can be calculated using the Kubo formalism by integrating over the entire deformed FBZ due to mechanical strain. The Hamiltonian in low energy can be approximated as [12]:

$$\widehat{H}_s \cong \hbar v_f \boldsymbol{\sigma} \cdot (\boldsymbol{I} + \boldsymbol{\epsilon} - \beta \boldsymbol{\epsilon}) \cdot \boldsymbol{k}', \tag{3.4}$$

where $\boldsymbol{\sigma} = (\sigma_x, \sigma_y)$ and σ_x, σ_y are two Pauli matrices and $\boldsymbol{k}'$ is the wavevector in deformed reciprocal space. A direct consequence of solving this Hamiltonian is that the band structure is deformed. In pristine graphene, the Dirac cone is circular. Given an energy level, the iso-energy

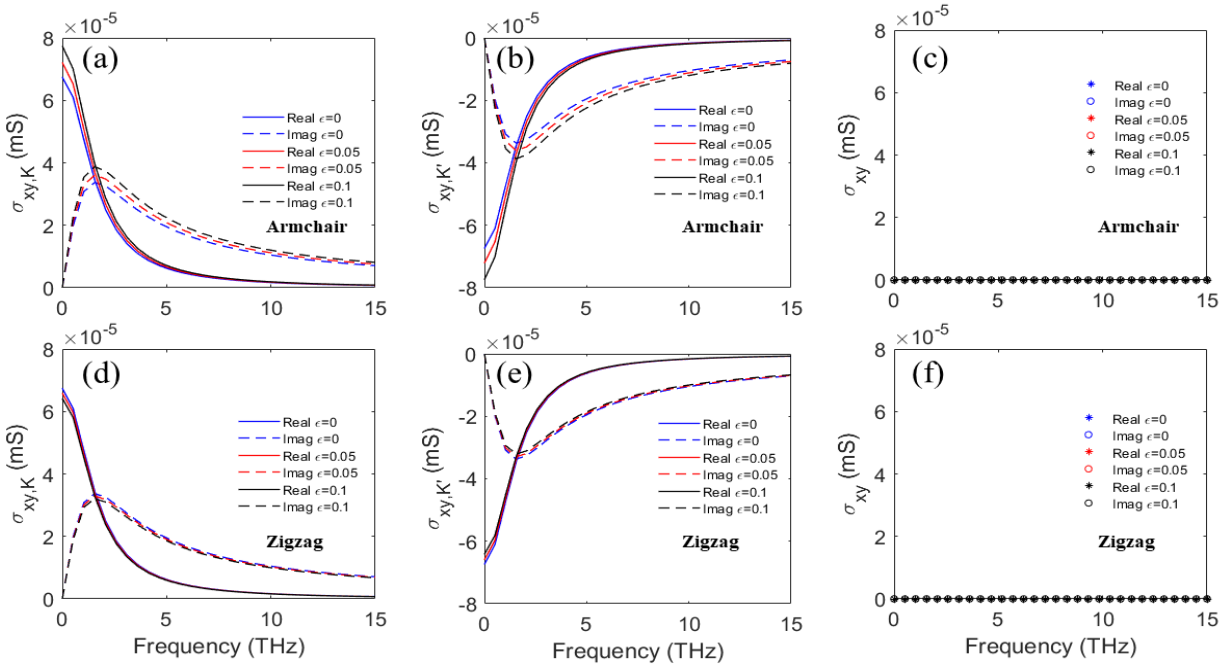

Figure 3.5 Frequency dependence of Hall conductivity computed from K valley and K' valleys and their sums under (a)-(c) armchair and (d)-(f) zigzag uniaxial strain for several strain magnitudes. The parameters used are

contour in the reciprocal space is circular. However, the new iso-energy contour is deformed in reciprocal space and has the relation with that of unstrained graphene by:

$$\boldsymbol{k} = (\boldsymbol{I} + \boldsymbol{\epsilon} - \beta\boldsymbol{\epsilon}) \cdot \boldsymbol{k}', \tag{3.5}$$

so the iso-energy contour may not be circular and depending on the strain type it can be elliptical under uniaxial strain and remains circular under isotropic strain. The electron wavefunction velocity operators are also deformed in reciprocal space and is essential in our calculation of strained graphene. Here we compute the contributions to the Hall conductivity from K and K' valleys individually and their sums as a function of frequency under armchair (upper panels) and zigzag (lower panels) uniaxial strain for three strain magnitudes and plot them in Fig. 3.5. For armchair strain, both real and imaginary parts of the two valleys increase as strain magnitude increases. The values from two valleys have opposite signs but the same modulus. When summed up, their total contribution to Hall conductivity vanished as shown in Fig. 3.5(c), which implies

that uniform strain does not violate TRS. Both real and imaginary parts of the two valleys decrease as strain magnitude increases but not as much as they increase for armchair strain. The change upon strain is slightly for zigzag so that we will potentially use armchair strain to engineering the Hall conductivity of graphene in the future. We also plot the diagonal conductivity σ_{xx} and σ_{yy} as a function of frequency for several strain magnitudes in Fig. 3.6. Results show that σ_{xx} increases with strain magnitude but σ_{yy} decreases, thus leading to an effectively anisotropic surface.

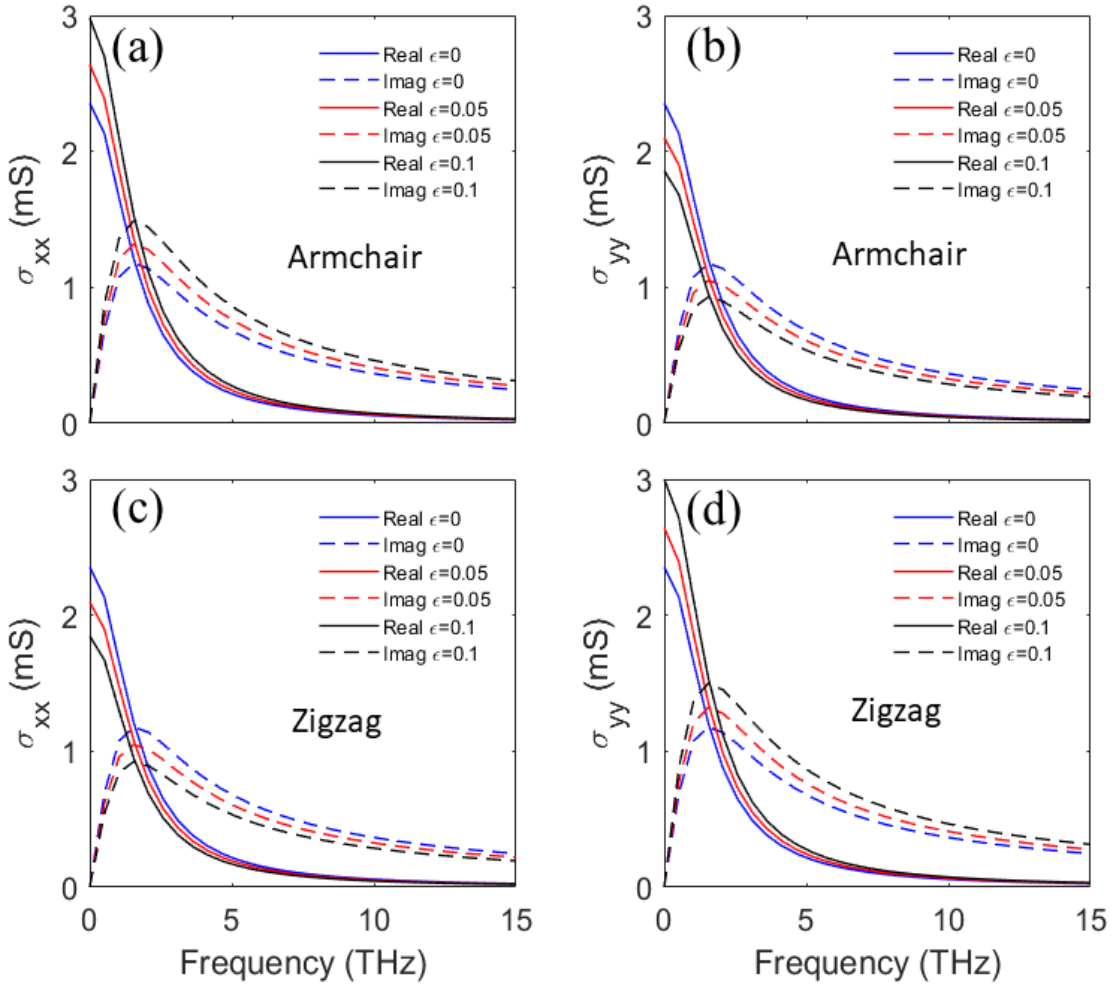

Figure 3.6 Frequency dependence of diagonal conductivities under (a) and (b) Armchair and (c) and (d) Zigzag uniaxial strain for several different strain magnitudes. Parameters used are $\mu_c = 0.2\ eV, \tau = 0.1\ ps$.

3.3 Graphene in non-uniform strain

As we discussed in the previous section, when mechanical strain changes smoothly over distances comparable to interatomic spacing, it maintains sublattice symmetry and instead distorts the Brillouin zone in a manner that results in the displacement of the graphene's Dirac cones situated at K and K' points in opposite directions. However, the application of non-uniform strain to graphene has emerged as a powerful tool to tailor its band structure and explore novel physical phenomena. Non-uniform strain refers to strain distributions that are spatially varying, as opposed to uniform strain applied uniformly. Non-uniform strain in graphene introduces a rich panorama of effects, including the emergence of pseudomagnetic fields, localized electronic states, and the potential to engineer topological phases. Among them, the existence of pseudomagnetic fields, as has been proved by experiments [16], transforms the linear dispersion and continuous energy states to discretized Landau levels, strongly mimicking the behavior of real magnetic fields. However, as opposed to the effect of real magnetic fields which break time-reversal symmetry, a pseudomagnetic field rather shifts the two Dirac cones in opposite directions, which can be captured by opposite pseudo-vector potentials. The implication of this is the unbroken time-reversal symmetry of under non-uniform strain, since the net Hall effect induced by the opposite pseudomagnetic field cancels out in K and K' valley.

Understanding the interplay between strain and electronic properties in non-uniformly strained graphene holds great promise for the development of advanced electronic and optoelectronic devices. This section primarily delves into the connection between non-uniform strain applied to graphene and the pseudomagnetic fields generated as a result of this strain, shedding light on the innovative possibilities it offers for engineering and the realization of novel nonreciprocal phenomena.

3.3.1 Strain-induced pseudomagnetic fields

The strain tensor induced by structural deformation in graphene is characterized by

$$\epsilon_{ij}(\boldsymbol{r}) = \frac{1}{2}\Big(\partial_i u_j(\boldsymbol{r}) + \partial_j u_i(\boldsymbol{r}) + \partial_i h(\boldsymbol{r})\partial_j h(\boldsymbol{r})\Big), \tag{3.7}$$

where $\boldsymbol{u}(\boldsymbol{r})$ and $h(\boldsymbol{r})$ are the in-plane and out-of-plane deformation fields, respectively, $\boldsymbol{r}$ denotes the position in the $x-y$ plane. The deformation fields can be determined by high-resolution atomic force microscopy (AFM). If we mainly focus on the out-of-plane deformation induced by nanostructures that induce vertical lattice distortion much bigger than in-plane lattice distortion, the strain components can be calculated as:

$$\epsilon_{xx} = \frac{1}{2}\left(\frac{\partial h(\boldsymbol{r})}{\partial x}\right)^2, \tag{3.8}$$

$$\epsilon_{yy} = \frac{1}{2}\left(\frac{\partial h(\boldsymbol{r})}{\partial y}\right)^2, \tag{3.9}$$

$$\epsilon_{xy} = \frac{1}{2}\frac{\partial h(\boldsymbol{r})}{\partial x}\frac{\partial h(\boldsymbol{r})}{\partial y}. \tag{3.10}$$

The pseudo-gauge field or vector potential $\boldsymbol{A}$ originated from the strain field is expressed as

$$\boldsymbol{A} = \frac{\beta}{a}\begin{pmatrix}\epsilon_{xx} - \epsilon_{yy} \\ -2\epsilon_{xy}\end{pmatrix}, \tag{3.11}$$

where a is the lattice constant and $\beta = -\partial \ln t / \partial \ln a$ is the Grüneisen parameter. The resulting pseudomagnetic field B_s from this vector potential $\boldsymbol{A}$ can be expressed in terms of the strain components:

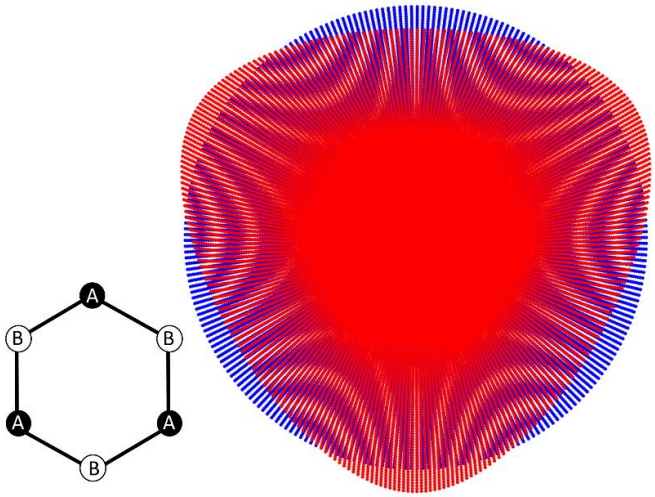

Figure 3.7 A graphene circular disc with mesh points (blue dots) and the distorted lattice (red dots) with the displacement field given by Eq. 3.13. The inset shows the orientation of a single graphene hexagonal lattice.

$$B_s = \frac{\beta}{a}\Big(\partial_y \epsilon_{xx}(x,y) - \partial_y \epsilon_{yy}(x,y) + 2\partial_x \epsilon_{xy}(x,y)\Big). \tag{3.12}$$

An immediate observation from the above equation is that with uniform strain fields $\boldsymbol{A} = \text{const}$, which yield zero B_s. Therefore, pseudomagnetic field can only be created by non-uniform strain. It is easy to show that a uniform pseudomagnetic field can be implemented by the following two-dimensional displacement fields in its polar coordinate representation [13]

$$u(\boldsymbol{r},\theta) = \begin{pmatrix} u_r \\ u_\theta \end{pmatrix} = \begin{pmatrix} cr^2 \sin 3\theta \\ cr^2 \cos 3\theta \end{pmatrix}, \tag{3.13}$$

where c is a constant determining the strength of the displacement field. In the following, the x-axis is chosen to be the zigzag direction of the graphene honeycomb lattice. To visualize how graphene is distorted with the above displacement field, we use a graphene disc which is shown in Fig. 3.7 and apply the field $u(\boldsymbol{r},\theta)$ in Eq. 3.13. We can clearly see that the graphene disc is stretched towards the three equivalent crystallographic directions $\langle 100 \rangle$. The resulting uniform

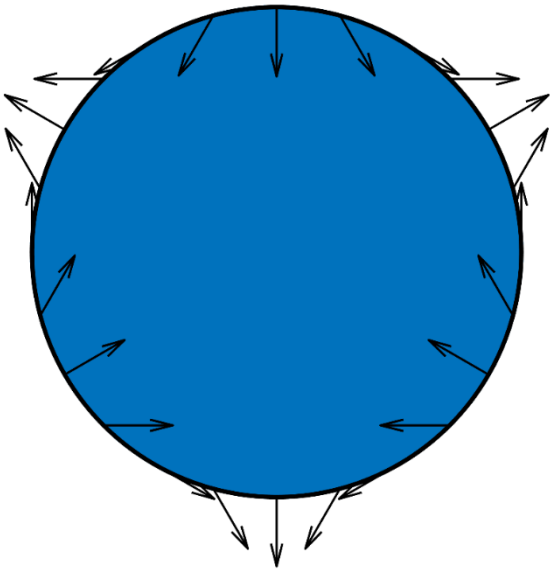

Figure 3.8 The distribution of external forces applied at the perimeter of the graphene disc (black arrows) that would induce the distortion in Fig. 3.7.

pseudomagnetic field is readily calculated to be $B_s = \frac{8\beta c}{a}$ using the polar form of Eq. 3.7 and 3.12. However, to generate such displacement fields, the needed realistic applied forces on the graphene disc still have to be investigated. It is demonstrated that such distortion can be generated by in-plane forces only at the perimeter [13]

$$F_x(\theta) \propto \mu \sin 2\theta, F_x(\theta) \propto \mu \cos 2\theta, \tag{3.14}$$

where μ is the shear modulus. The forces applied at the perimeter of graphene disc is shown in Fig. 3.8. It is difficult to create such strain experimentally because it involves tangential forces and both compression and stretching simultaneously.

On the other hand, it has been shown that when graphene is placed on metasurfaces, it can likewise give rise to pseudomagnetic fields. There are a variety of metasurfaces that could be potential candidates. To analyze the local strain distribution, we utilized the example of strained graphene on nanopillars array from Ref. [14], as shown in the SEM image in Fig. 3.9(a). The topology of two-unit cells is reconstructed in Fig. 3.9(b). In this representation, the brightest areas

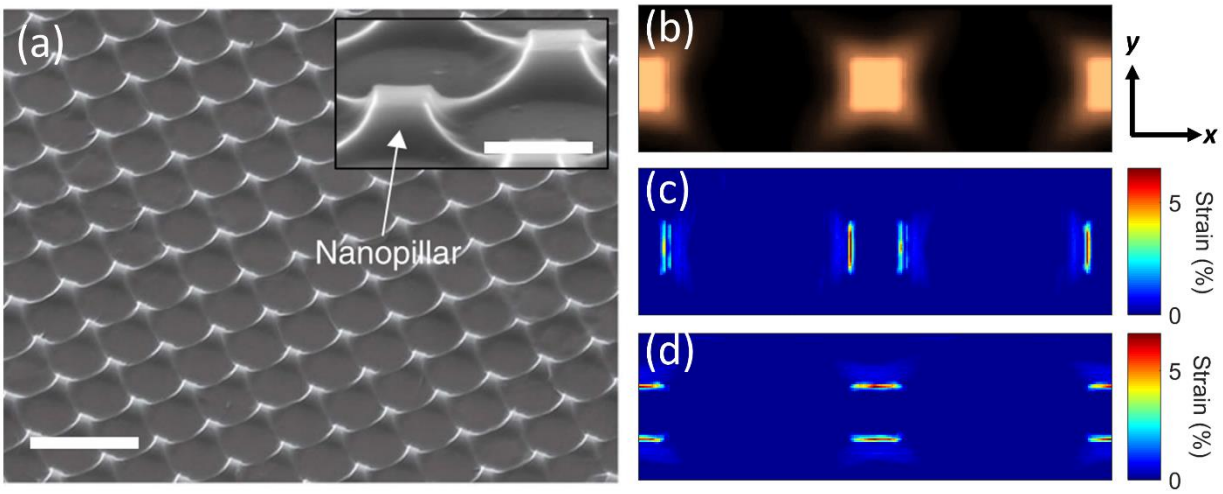

Figure 3.9 (a) Tilted view of SEM image of strained graphene sheet on nanopillar array. (b) reconstructed topology of two nanopillar unit cells from AFM data. (a) and (b) adapted from Ref. [14].

correspond to a height of 300 nm, while the darkest areas signify a height of 0 nm. The lateral dimensions of the nanopillars are approximately 300 nm. Due to the pronounced structural deformation around the sharp corners and edges of the nanopillars, a significant tensile strain of approximately 6.5% is observed at the atomic scale. By decomposing the strain distribution into its x and y components, illustrated in the Fig. 3.9(c) (ϵ_{xx}) and Fig. 3.9(d) (ϵ_{yy}), respectively, we observed that ϵ_{yy} is nearly negligible where ϵ_{xx} is maximized. However, since the pseudomagnetic fields are only generated on the sharp edges of the nanopillars, it is still difficult to resolve the carrier properties in those regions for some optical systems. Therefore, it is highly desirable to obtain uniform pseudomagnetic field over a large area using simple straining approaches.

A facile and effective way to achieve extreme pseudomagnetic fields with uniform distributions across a large planar graphene sheet is through uniaxial stretching [15]. Notice that the uniaxial stretching we are discussing here would result in some strain gradient along a specific graphene crystallographic direction instead of uniform strain which would lead to zero pseudomagnetic field that we mentioned in previous section. Assuming a uniform pseudomagnetic

field can be obtained through a specific uniaxial strain. The stress tensor components σ_{ij} are correlated with the strain tensor components ϵ_{ij} in the form of

$$\sigma_{xx} = \frac{E}{1-\nu^2}\left(\epsilon_{xx} + \nu\epsilon_{yy}\right), \tag{3.14}$$

$$\sigma_{yy} = \frac{E}{1-\nu^2}\left(\epsilon_{yy} + \nu\epsilon_{yy}\right), \tag{3.15}$$

$$\sigma_{xy} = 2\mu\epsilon_{xy}, \tag{3.16}$$

where E_g is graphene Young's modulus, ν is Poisson's ratio and correlated with the shear modulus μ by $\mu = \frac{E}{2(1+\nu)}$. The stress equilibrium requires that

$$\frac{\partial\sigma_{xx}}{\partial x} + \frac{\partial\sigma_{yy}}{\partial y} = 0 \text{ and } \frac{\partial\sigma_{xy}}{\partial x} + \frac{\partial\sigma_{yy}}{\partial y} = 0. \tag{3.17}$$

For uniaxial strain along graphene armchair direction, there is $\epsilon_{xx} = -\nu\epsilon_{yy}$. Therefore, we can solve Eq. 3.14-3.17 and obtain

$$\frac{\partial\epsilon_{xy}}{\partial y} = 0, \frac{\partial\epsilon_{xy}}{\partial x} = -(1+\nu)\frac{\partial\epsilon_{yy}}{\partial y}, \tag{3.18}$$

Substituting Eq. 3.18 into Eq. 3.12 we arrive to the following equation which dictates the general requirements for generating a uniform pseudomagnetic field

$$B_s = \frac{3\beta}{a}(1+\nu)\frac{\partial\epsilon_{yy}}{\partial y}. \tag{3.19}$$

The above equation reveals that uniform pseudomagnetic field can be realized using uniaxial strain in graphene. For example, a constant strain gradient $\partial\epsilon_{yy}/\partial y$, i.e., a linear tensile strain along the armchair direction of the honeycomb lattice can generate a uniform pseudomagnetic field across a large area in graphene.

Let us now consider a tapered graphene ribbon as depicted in Fig. 3.10(a). Note that our analysis holds for geometries beyond trapezoidal. The ribbon basal width is set to be W_0 and length L. The wrist width at a given point y is described by a function $W = f(y)W_0$. Let us assume that the external forces are applied evenly at the top and bottom edges. When the length is much larger than the wrist L, it is reasonable to assume that the strain ϵ_{yy} stays constant along any cross-section cut in x direction except in the vicinity of the corners. Following the stress-strain relation, the forces balance along any cross-section cut of the graphene nanoribbon in x direction requires

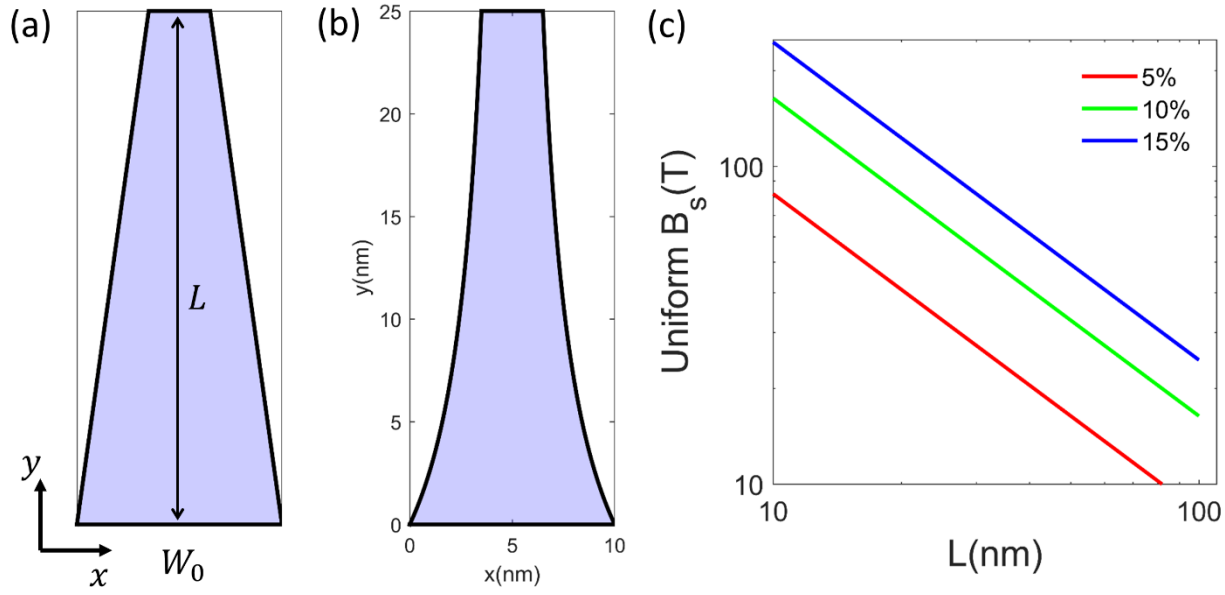

Figure 3.10 (a) The schematic of the graphene nanoribbon. (b) Designed graphene nanoribbon that would generate uniform pseudomagnetic field over large area. (c) The relation between the intensity of pseudomagnetic field and graphene nanoribbon length for several global uniaxial strain intensity of $\epsilon_{app} = 5\%, 10\%$ and 15%.

$$F = E_g \epsilon_{yy} f(y) W_0 h, \tag{3.20}$$

where F is the force applied at the two parallel sides to generate the tensile strain and $h = 0.34$ nm is the thickness of the graphene monolayer. Rearranging the two sides of Eq. 3.20 and take the derivative of both sides with respect to y leads to

$$\frac{\partial \epsilon_{yy}}{\partial y} = -\frac{F}{E_g W_0 h} \frac{1}{f^2} \frac{\partial f}{\partial y}. \tag{3.21}$$

For a linear distribution of ϵ_{yy} along y direction, i.e., $\frac{\partial \epsilon_{yy}}{\partial y} = \text{const}$, there is the relation for the wrist function f

$$\frac{1}{f^2} \frac{\partial f}{\partial y} = C, \tag{3.22}$$

where C is a constant. Using the boundary conditions $f(0) = 1$ and $f(L) = f_L$, the solution of the wrist function is given by

$$f(y) = \frac{f_L L}{f_L (L - y) + y}, \tag{3.23}$$

and

$$C = \frac{f_L - 1}{f_L L}. \tag{3.24}$$

From the above equations, one can engineer uniform pseudomagnetic fields by properly designing the shape of the graphene nanoribbon. The shape of a graphene nanoribbon with parameters $L =$

25 nm, $W_0 = 10$ nm, $f_L = 0.3$ is drawn in Fig. 3.10(b). The applied force can be related with the global deformation by

$$\int_0^L \epsilon_{yy}\, dy = \Delta L, \tag{3.25}$$

where ΔL is related to the global uniaxial strain ϵ_{app} by $\epsilon_{app} = \Delta L/L$. Solving Eq. 3.25 give rise the solution of F

$$F = \frac{2\Delta L E_g f_r W_0 h}{(1+f_r)L}. \tag{3.26}$$

Substituting Eq. 3.26 and 3.23 into Eq. 3.21 gives

$$B_s = \frac{6\beta}{a}\frac{\epsilon_{app}(1-f_r)}{L(1+f_r)}(1+\nu). \tag{3.27}$$

A parametric study informs that the intensity of the pseudomagnetic field is linear proportional to the applied uniaxial strain ϵ_{app} inversely proportional to the graphene nanoribbon length. This can be seen from the plot in Fig. 3.10(c).

3.3.2 Electronic band structure of graphene under non-uniform strain

Recent theoretical research suggests that when graphene layers experience strain, it generates a pseudomagnetic field, resulting in observable Landau levels. In a study conducted by Levy and colleagues [16], scanning tunneling microscopy was employed to investigate the energy states of graphene grown on a platinum surface, forming highly strained "nanobubbles." This strain is equivalent to exposing the material to extremely high magnetic fields, surpassing 300 Tesla.

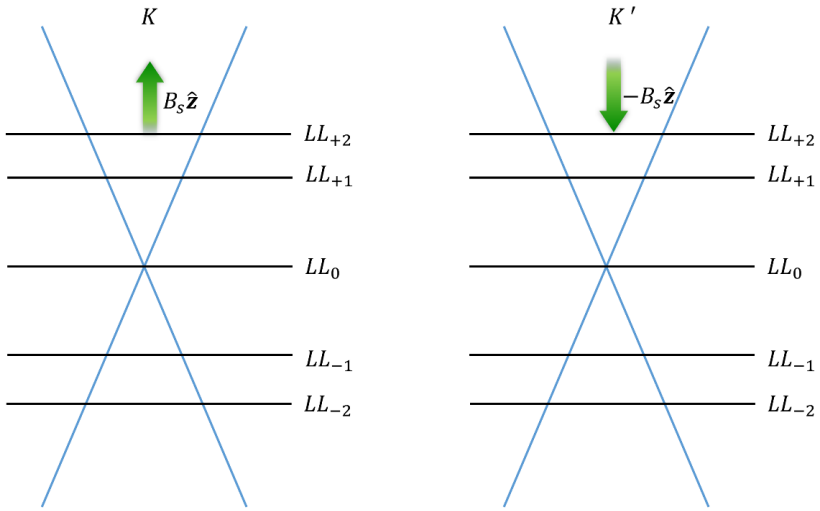

Figure 3.11 Five pseudo-Landau levels in K and K' valleys in graphene under non-uniform strain.

Consequently, the application of strain is shown to effectively alter the electronic properties of graphene.

Non-uniform strain causes the energy-momentum relation near the Dirac points to deviate from the ideal linear dispersion, and this deviation can be described as the generation of pseudomagnetic fields. The strain-induced pseudomagnetic field gives rise to "pseudo-Landau levels" within each valley which is schematically shown in Fig 3.11 where only five Landau levels are drawn. These levels in strained graphene behave similarly to the Landau levels in real magnetic fields [14]. The strength and orientation of the pseudomagnetic field can be different for the K and K' valleys. This implies that the two valleys can exhibit distinct responses to the same strain profile, resulting in intriguing electronic and transport properties, while the time-reversal symmetry (TRS) remains intact, much like in the case of uniform strain.

In this scenario, the density of states (DOS) transitions from a linear relationship with respect to energy to a spectrum in which the density is accumulated on discrete Landau levels. Such response is governed by the relation [14]

$$\mathrm{DOS}(E) = \frac{1}{\pi}\sum_{n}\frac{\gamma}{(E-E_n)^2+\gamma^2}, \tag{3.13}$$

where $\gamma = 7\ meV$ is the broadening factor of Laudau level. Figure 3.12 shows the calculated DOS for strained graphene under various pseudo-magnetic field conditions (10, 40 and 80 T).

3.4 Exploiting pseudo-magnetic fields with low-B

As described above, certain types of nonuniform strain can behave as pseudomagnetic field acting on different valleys in the reciprocal space. The contributions to Hall conductivity from K and K' valleys cancel out yielding zero net Hall conductivity and overall TRS is not broken. Effectively, we have B_{ps} in K valley and $-B_{ps}$ in K' valley. Notice that this only happens in reciprocal space rather than physical space. An external magnetic field acts in physical space, it renders the same value everywhere in reciprocal space. Thus, the total magnetic field in K valley is $B_{ps} + B_e$ while in K' valley we have $-B_{ps} + B_e$ and they do not cancel each other out and will

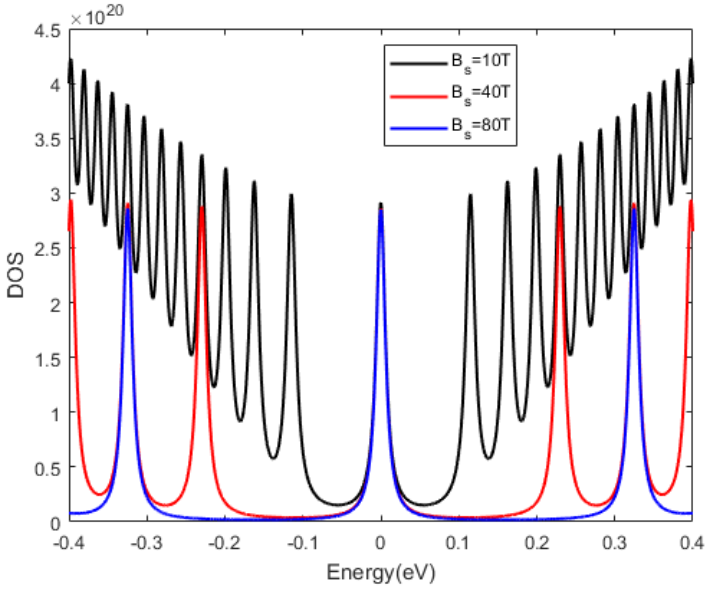

Figure 3.12 The Density of States is calculated for strained graphene under pseudo-magnetic fields of 10 T (black), 40 T (red), and 80 T (blue). These calculations employ the broadening parameter γ = 7 meV.

give rise to large FR nearly the cyclotron frequency mainly determined by B_{ps}. The amplitude largely depends on B_e and τ.

To obtain the Hall conductivity for strained graphene under a magnetic field, we follow the approach outlined in [17] based on mathematical fitting the Kubo formula under magnetic field as present in Eq. 2.14. The Hall conductivity for strained graphene calculated from K and K' valleys are fitted by Eq. 2.14 individually to correlate with an effective pseudomagnetic field $\pm B_{ps}^{eff}$. The total effective magnetic field in presence of an external magnetic field will be $B_e \pm B_{ps}^{eff}$ for K and K' valleys respectively. Therefore, the total Hall conductivity can be obtained by:

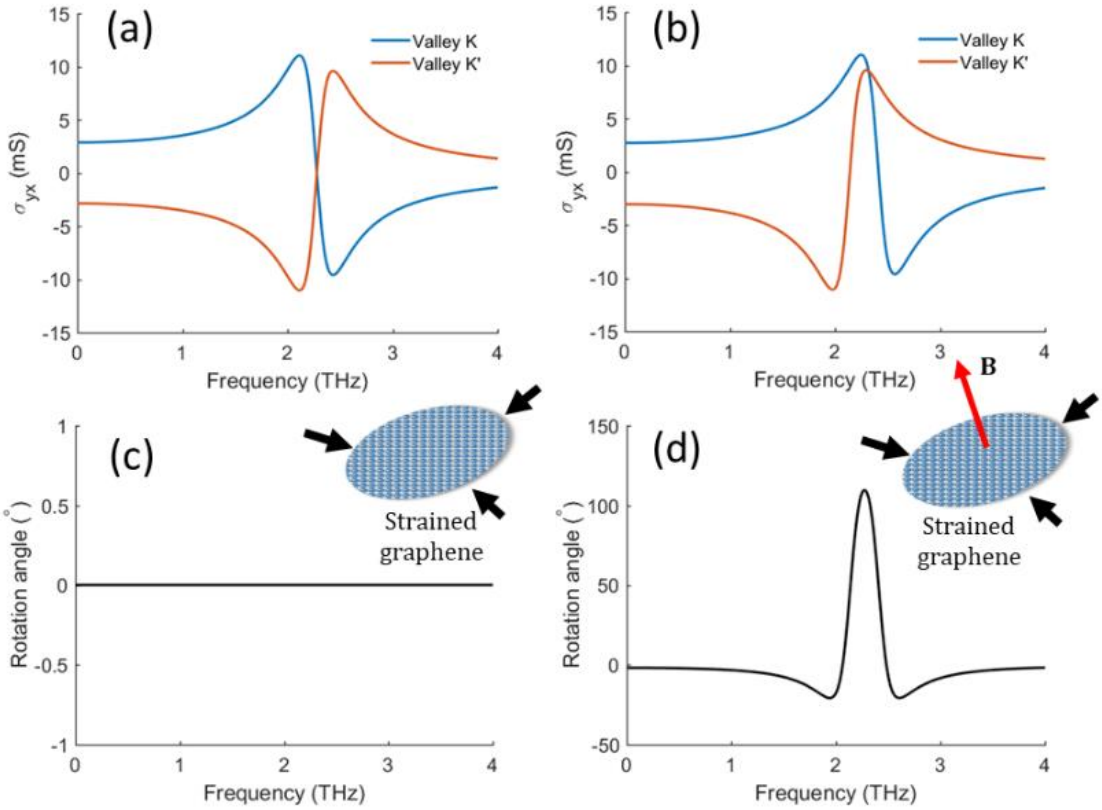

Figure 3.13 Hall conductivity computed considering K and K' valleys respectively and the corresponding Faraday rotation of strained graphene and of strained graphene under a small magnetic field . $\tau = 1\ ps, \mu_c = 0.35\ eV, B_{ps} = 5\ T, B_{ext} = 0.5\ T$.

$$\sigma_{xy}(\omega, B_e) = \sigma_{xy,K}\left(\omega, B_e + B_{ps}^{eff}\right) + \sigma_{xy,K'}\left(\omega, B_e - B_{ps}^{eff}\right). \quad (3.6)$$

To illustrate the idea, we plot the Hall conductivity and the corresponding Faraday rotation angle in Fig. 3.13 under an effective pseudomagnetic field which mimics the role of strain with and without a small external magnetic field to break the reciprocity. In Fig. 3.13(a), with only strain being applied, the contributions from K and K' valleys are large but their sum is zero so that the reciprocity is not broken. However, in Fig. 3.13(b), when a small external magnetic field is applied, it breaks the balance between the opposite pseudomagnetic field in the two valley such that the spectra of the conductivity from K and K' valleys shift in opposite direction thus creating a large Faraday rotation angle. The increasing strain magnitude does boost the diagonal conductivity from K and K' valleys. Graphene strain engineering opens up ways to obtain non-reciprocity combining different TRS-breaking techniques, alleviating the need of large magnetic field.

3.5 Conclusions and future work

This chapter has explored uniform and non-uniform strain on pristine graphene. The uniform strain does not break TRS and the overall Hall conductivity remains zero after graphene is strained. In contrast, non-uniform strain profoundly modifies the band structure of graphene. The continuous energy dispersion is quantized with non-equidistant spacings which would possibly open up opportunity of separately optically addressing those transitions associated with them. The strain-induced pseudomagnetic field further indicates that the optical transitions in K and K' valleys would follow distinct selection rules, which if combined with optical pumping of CP light, could contribute to conceptualizing a novel approach to the realization of magnetless nonreciprocity in 2D materials.

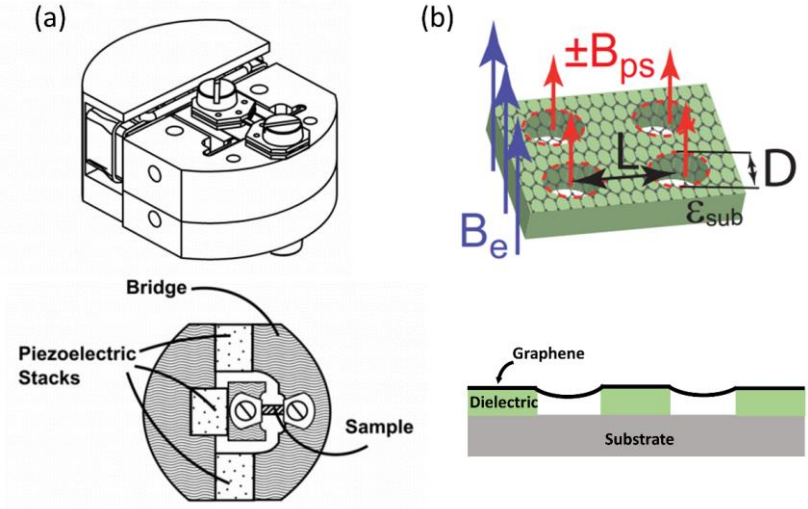

Figure 3.14 Two approaches of creating uniform strain [17],[19].

Future works following the theoretical investigation of strain-induced pseudomagnetic field include the experimental demonstration of such field. This could be carried out by Hall measurement. There are several possibilities to generate non-uniform strain in graphene. For instance, one can strain engineer graphene using commercialized strain cells [19]. This is illustrated in Fig. 3.14(a) where a sample with graphene on top of a silicon chip is either contracted or compressed uniaxially by two sets of piezoelectric stacks of a strain cell. Another approach relies on placing graphene on a set of dielectric substrates perforated with periodic nanohole arrays as shown in Fig. 3.14(b).

3.6 Chapter references

[1] Ni, Zhen Hua, et al. "Uniaxial strain on graphene: Raman spectroscopy study and band-gap opening." *ACS nano* 2.11 (2008): 2301-2305.

[2] Gui, Gui, Jin Li, and Jianxin Zhong. "Band structure engineering of graphene by strain: first-principles calculations." *Physical Review B* 78.7 (2008): 075435.

[3] Lindsay, L., et al. "Phonon thermal transport in strained and unstrained graphene from first principles." *Physical Review B* 89.15 (2014): 155426.

[4] Bae, Sang-Hoon, et al. "Graphene-based transparent strain sensor." *Carbon* 51 (2013): 236-242.

[5] Wei, Ning, et al. "Strain engineering of thermal conductivity in graphene sheets and nanoribbons: a demonstration of magic flexibility." *Nanotechnology* 22.10 (2011): 105705.

[6] Levy, N., et al. "Strain-induced pseudo–magnetic fields greater than 300 tesla in graphene nanobubbles." *Science* 329.5991 (2010): 544-547.

[7] Guinea, Francisco, et al. "Generating quantizing pseudomagnetic fields by bending graphene ribbons." *Physical Review B* 81.3 (2010): 035408.

[8] Guinea, Francisco, Mikhail I. Katsnelson, and A. K. Geim. "Energy gaps and a zero-field quantum Hall effect in graphene by strain engineering." *Nature Physics* 6.1 (2010): 30-33.

[9] Truesdell, Clifford, and Walter Noll. "The non-linear field theories of mechanics." The non-linear field theories of mechanics. Springer, Berlin, Heidelberg, 2004. 1-579.

[10] Oliva-Leyva, M., and Gerardo G. Naumis. "Anisotropic AC conductivity of strained graphene." *Journal of Physics: Condensed Matter* 26.12 (2014): 125302.

[11] Oliva-Leyva, M., and Gerardo G. Naumis. "Generalizing the Fermi velocity of strained graphene from uniform to nonuniform strain." Physics Letters A 379.40-41 (2015): 2645-2651.

[12] Oliva-Leyva, M., and Gerardo G. Naumis. "Understanding electron behavior in strained graphene as a reciprocal space distortion." *Physical Review B* 88.8 (2013): 085430.

[13] Guinea, Francisco, Mikhail I. Katsnelson, and A. K. Geim. "Energy gaps and a zero-field quantum Hall effect in graphene by strain engineering." Nature Physics 6.1 (2010): 30-33.

[14] Kang, Dong-Ho, et al. "Pseudo-magnetic field-induced slow carrier dynamics in periodically strained graphene." Nature Communications 12.1 (2021): 5087.

[15] Zhu, Shuze, Joseph A. Stroscio, and Teng Li. "Programmable extreme pseudomagnetic fields in graphene by a uniaxial stretch." *Physical review letters* 115.24 (2015): 245501.

[16] Levy, N., et al. "Strain-induced pseudo–magnetic fields greater than 300 tesla in graphene nanobubbles." *Science* 329.5991 (2010): 544-547.

[17] Slipchenko, Tetiana M., et al. "Strain-induced large Faraday rotation in graphene at subtesla external magnetic fields." Physical Review Research 1.3 (2019): 033049.

[18] Vozmediano, Maria AH, M. I. Katsnelson, and Francisco Guinea. "Gauge fields in graphene." *Physics Reports* 496.4-5 (2010): 109-148.

[19] Kissikov, T., et al. "Nuclear magnetic resonance probe head design for precision strain control." Review of Scientific Instruments 88.10 (2017): 103902.

[20] Ni, Z. H., et al. "Raman spectroscopy of epitaxial graphene on a SiC substrate." Physical Review B 77.11 (2008): 115416.

[21] Sounas, Dimitrios L., and Christophe Caloz. "Electromagnetic nonreciprocity and gyrotropy of graphene." Applied Physics Letters 98.2 (2011): 021911.

[22] Sounas, Dimitrios L., and Christophe Caloz. "Gyrotropy and nonreciprocity of graphene for microwave applications." IEEE Transactions on Microwave Theory and Techniques 60.4 (2012): 901-914.

[23] Kumar, Anshuman, et al. "Chiral plasmon in gapped Dirac systems." Physical Review B 93.4 (2016): 041413.

4. Optically pumped strained graphene

Chapter 2 focused on optically-pumped gapped graphene and derived techniques to calculate the population and conductivity of this 2D material. The underlying reason for this choice is that, in order to obtain net Hall effect, it is required to have a 2D material with hexagonal lattice structure that possesses distinct optical selection rules for its two valleys (K and K'). The use of rotating wave approximation (RWA) adds another drawback to the same method, restricting it from being applicable to a large number of systems beyond gapped Dirac systems. From the discussion of Chapter 3, we are enlightened with the idea that strained-induced pseudomagnetic field can be used to enable distinct optical selection rules within the two valleys, lifting the restriction of using gapped Dirac systems. In this chapter, a more accurate theory will be considered to model the carrier dynamics in optically-pumped strained pristine graphene and other 2D systems. The carrier dynamics in strained graphene considering the carrier-carrier scattering after optical excitation is thoroughly investigated using density matrix formalism. No certain strain scenario is presumed, and therefore a Landau quantized graphene attributed to a non-uniform pseudomagnetic field caused by some unknown strain profile is considered. We first start by re-evaluating the tight-binding model for Laudau-quantized graphene. The optical selection rules are revisited using an optical matrix element approach different from the dipole matrix element approach described in Chapter two. For carrier relaxation mechanism, we focus on the carrier-carrier scattering and investigate its dominant role in the carrier redistribution after optical excitation and before thermal equilibrium. To calculate the imbalanced population in strained graphene upon optical pump of a circularly polarized light, we assume opposite magnetic field in the graphene K and K' valleys. The population imbalance between the two valleys will be presented together with the resulting conductivity calculated by summing up the perturbed Landau levels within the Kubo formalism.

Due to the high complexity involved in this coupled system of differential equations employed to model these responses, achieving an analytical solution is unfeasible in most scenarios. Consequently, our findings are obtained through the numerical evaluation of these differential equations. Our results suggest that merging strain engineering and optical pump will open new possibilities to break and manipulate electromagnetic nonreciprocity.

4.1 Tight-binding model for Landau-quantized graphene

To calculate the dispersion relation of Landau-quantized graphene, let us first write down the graphene Hamiltonian in the low-energy regime [1] as

$$H = v_F \boldsymbol{\sigma}_\xi \cdot \boldsymbol{p} = v_F \begin{pmatrix} 0 & \xi p_x - i p_y \\ \xi p_x + i p_y & 0 \end{pmatrix}, \tag{4.1}$$

where $\boldsymbol{p} = (p_x, p_y)$ is the momentum and $\xi = \pm 1$ is the valley index. Using the substitution of momentum $\boldsymbol{p} \to \boldsymbol{\pi} = \boldsymbol{p} + e\boldsymbol{A}(\boldsymbol{r})$ to account for an external magnetic field, the Hamiltonian can be formulated as [1]

$$H_B = v_F \boldsymbol{\sigma}_\tau \cdot \boldsymbol{\pi} = v_F \begin{pmatrix} 0 & \tau\pi_x - i\pi_y \\ \tau\pi_x + i\pi_y & 0 \end{pmatrix}. \tag{4.2}$$

For simplicity, the ladder operators are defined as

$$a^\dagger = \frac{l_B}{\sqrt{2}\hbar}(\pi_x + i\pi_y),\ a = \frac{l_B}{\sqrt{2}\hbar}(\pi_x - i\pi_y), \tag{4.3}$$

where $l_B = \sqrt{\hbar/(eB)}$ is the magnetic length. The relations $a^\dagger|n\rangle = \sqrt{n+1}|n+1\rangle$ and $a|n\rangle = \sqrt{n}|n-1\rangle$ define the number operator $N = a^\dagger a$. Then, the Hamiltonian for electrons in graphene's K and K' valleys are simplified to

$$H_B^K = \hbar\omega_c \begin{pmatrix} 0 & a \\ a^\dagger & 0 \end{pmatrix}, \quad H_B^{K'} = -\hbar\omega_c \begin{pmatrix} 0 & a^\dagger \\ a & 0 \end{pmatrix}, \tag{4.4}$$

where $\omega_c = \sqrt{2}v_F/l_B$ is the cyclotron frequency. Then, the Schrodinger equation $H_B^\tau|\boldsymbol{\psi}\rangle = \mathcal{E}|\boldsymbol{\psi}\rangle$ is solved, which allows to determine electron's energy and wave function as [2]-[3]

$$\mathcal{E}_n^\lambda = \lambda\sqrt{n}\hbar\omega_c = \lambda v_F\sqrt{2n\hbar e_0 B}, \tag{4.5}$$

$$|\boldsymbol{\psi}\rangle = \frac{\alpha_n}{\sqrt{2}}\begin{pmatrix} |n\rangle \\ \xi\lambda|n-1\rangle \end{pmatrix}, \alpha_n = \begin{cases} \sqrt{2}, & n = 0 \\ 0, & n \neq 0 \end{cases}, \tag{4.6}$$

where $\lambda = \pm 1$ is the band index. The Landau-quantized energy levels are not equidistant spaced as compared to conventional two-dimensional electron gases due to the graphene's intrinsic linear dispersion. The first few Landau levels are plotted as a function of magnetic field in Fig. 4.1. We can see that the spacing of the adjacent energy level grows following a square root relation with respect to the magnetic field. Note that the external magnetic field can also interact with the magnetic moment due to the electron spin, which would give rise to the phenomena called the Zeeman effect where each Landau level splits into two distinct energy branches with different spin states. However, as can be seen in Fig. 3.12, the Landau level broadening caused by electron-impurity scattering actually superimposes with Zeeman splitting. However, this effect is small and will be neglected in the scenarios considered in this Thesis.

In graphene under a magnetic or pseudomagnetic field, each Landau level is indeed degenerate, and the quantum number that distinguishes the states within a single Landau level is the magnetic quantum number, often denoted as m. This quantum number arises from the quantization of the orbital motion of electrons in a magnetic field. In the context of the Landau level quantization, the magnetic quantum number m corresponds to different states within the

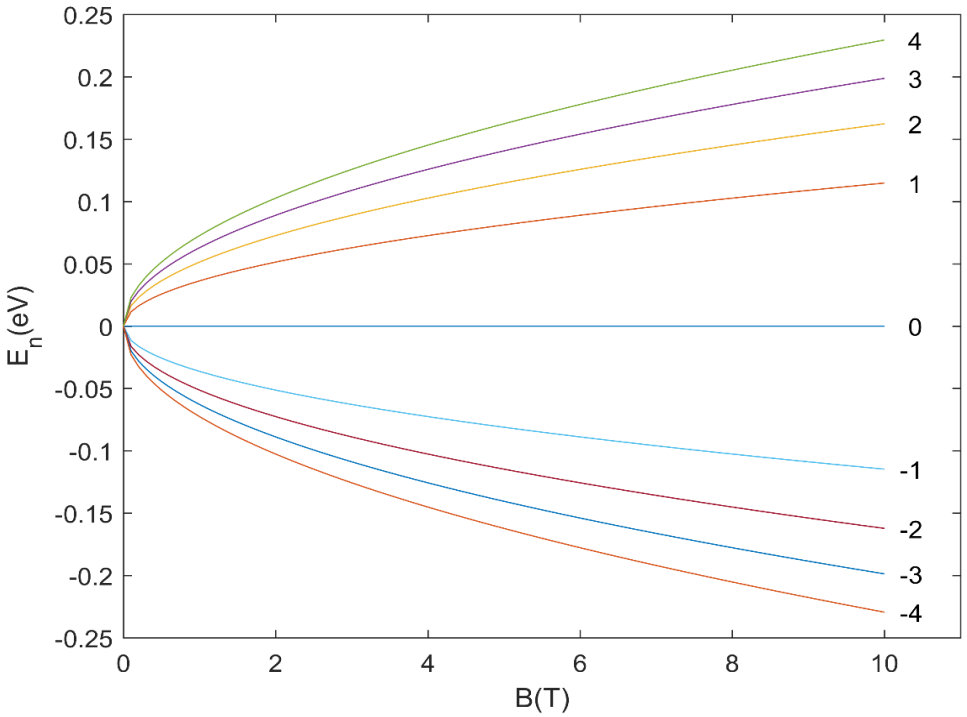

Figure 4.1 The dispersion of Laudau-quantized graphene under a homogeneous magnetic field as a function of the magnetic field with the first few Landau levels shown.

same Landau level that have the same energy but differ in their momentum or position in the cyclotron orbit. These states are degenerate because they are energetically equivalent in the presence of a uniform magnetic field. Therefore, while the Landau level index n determines the energy level in the magnetic field, the magnetic quantum number m differentiates between the degenerate states within each of these energy levels. This degeneracy is a key characteristic of the quantum Hall effect observed in graphene and other two-dimensional electron systems. To this end, the wavefunction described by Eq. 4.6 needs to take into account this quantum number m, which can be expressed as

$$|\boldsymbol{\psi}\rangle = \frac{\alpha_n}{\sqrt{2}}\begin{pmatrix} |n,m\rangle \\ \xi\lambda|n-1,m\rangle \end{pmatrix}. \tag{4.7}$$

Therefore, the momentum degree of freedom in the absence of an external magnetic field is then replaced by the quantum numbers n and m in the presence of an external magnetic field. The area of a cyclotron orbit is given by the uncertainty [3]

$$\Delta X \Delta Y = 2\pi l_B^2. \tag{4.8}$$

As a result, the degeneracy of each Landau level is given by [3]

$$N_B = \frac{A}{\Delta X \Delta Y} = \frac{A e_0 B}{2\pi\hbar}, \tag{4.9}$$

where A is the area of the graphene sheet and the quantum number m may assume integer number from 0 to $N_B - 1$.

Analogue to the case in the absence of a magnetic field, the wavefunction in the presence of a magnetic/pseudo-magnetic field can also be described by a superposition of the wavefunctions at the two sublattices [3],

$$\Psi(\boldsymbol{r}, \lambda n, m, \xi) = \frac{1}{\sqrt{N}} \sum_{l \in \{A,B\}} \sum_{\boldsymbol{R}_l} c_l(\boldsymbol{r}, \lambda n, m, \xi) e^{i\xi \boldsymbol{K}\cdot\boldsymbol{R}_l} \phi(\boldsymbol{r} - \boldsymbol{R}_l), \tag{4.10}$$

where $\boldsymbol{R}_l$ represents the coordinate of the two sublattices A and B. The coefficient c_l is the spatial representation of the wavefunction in Eq. 4.10 using the relation $\langle \boldsymbol{R}|\boldsymbol{\psi}\rangle = (c_A, c_B)$, and yields

$$\begin{aligned} c_A(\boldsymbol{r}, \lambda n, m, \xi) &= \frac{\alpha_n}{\sqrt{2}} \langle \boldsymbol{R}|n, m\rangle, \\ c_B(\boldsymbol{r}, \lambda n, m, \xi) &= \frac{\alpha_n}{\sqrt{2}} \xi\lambda \langle \boldsymbol{R}|n-1, m\rangle. \end{aligned} \tag{4.11}$$

The wavefunction is normalized using $\langle \Psi(\boldsymbol{r}, \lambda' n', m', \xi') | \Psi(\boldsymbol{r}, \lambda n, m, \xi) \rangle = \delta_{\lambda,\lambda'} \delta_{n,n'} \delta_{m,m'} \delta_{\xi,\xi'}$ and the explicit form of $\langle \boldsymbol{R} | n, m \rangle$ is given by

$$\langle \boldsymbol{R} | n, m \rangle = \sqrt{N_B} i^{|n-m|} \sqrt{\frac{\min(n,m)!}{\max(n,m)!}}, \tag{4.12}$$

with the vector $\boldsymbol{R} = (R, \varphi)$ in expressed in polar coordinates, and $\tilde{R} = R^2/2l_B^2$ and L_n^{α} the generalized Laguerre polynomials, respectively.

4.2 Optical matrix element

The optical matrix element is a crucial concept in the study of light-matter interactions, especially in the context of optical transitions in materials such as semiconductors or graphene [3],[7]. It is a fundamental component in calculating the probability of transitions between different quantum states of a system due to the absorption or emission of photons. In the case of optical transitions, the Hamiltonian typically involves the electric dipole interaction, which can be approximated as [3]

$$\boldsymbol{H}_{int} = i\hbar \frac{e_0}{m_0} \sum_{i,f} \boldsymbol{M}_{if} \cdot \boldsymbol{A}(t) a_f^{\dagger} a_i, \tag{4.13}$$

where e_0 and m_0 are the electron charge and mass, (i, f) denote the initial and final states, $\boldsymbol{A}(t)$ is the vector potential of the incident electromagnetic wave. The optical matrix element is central to determining the transition rate or the absorption/emission coefficients, as dictated by Fermi's Golden Rule, which states that the probability of a transition is proportional to the square of the magnitude of the optical matrix element [8],[9]. In simpler terms, it gives a measure of how "strongly" a particular electronic transition is coupled to the electromagnetic field of the incoming light. In quantum mechanics, the optical matrix element is defined as the matrix element of the

interaction Hamiltonian (or perturbation) between the initial and final states of the system. Mathematically, it is represented as [4]:

$$\boldsymbol{M}_{if} = \int d\boldsymbol{r}\Psi_f^*(\boldsymbol{r})\nabla\Psi_i(\boldsymbol{r}), \tag{4.14}$$

where $\Psi_i(\boldsymbol{r})$ and $\Psi_f(\boldsymbol{r})$ are the initial (ground state) and final state (excited state) of the electronic transition of unperturbed graphene. Within the tight-binding model basis, the optical matrix element can be calculated as [4]

$$\boldsymbol{M}_{if} = i\delta_{\xi_i,\xi_f}\delta_{m_i,m_f}\frac{\alpha_{n_i}\alpha_{n_f}m_0 v_F}{2\sqrt{2}\hbar}\left[\lambda_i\hat{\boldsymbol{\epsilon}}^-\delta_{n_f,n_i-1} + \lambda_f\hat{\boldsymbol{\epsilon}}^+\delta_{n_f,n_i+1}\right], \tag{4.15}$$

where m_0 is the mass of the free electron and $\hat{\boldsymbol{\epsilon}}^{\pm} = \left(\hat{\boldsymbol{e}}_x \mp i\hat{\boldsymbol{e}}_y\right)/\sqrt{2}$ denote the Jones vectors of left and right-handed circularly polarized light. The polarization of the external electric field is decomposed in circularly polarized basis, defined in such a way that the angular momentum of the photon of σ^+-polarization (σ^--polarization) is parallel (anti-parallel) to the magnetic field.

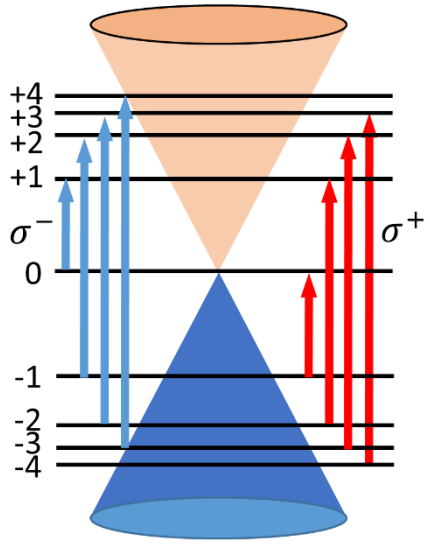

Figure 4.2 Allowed interband optical transitions in Landau-quantized graphene for σ^+ and σ^- polarizations with the only first few Landau levels sketched.

Assuming the light travels in the same direction as the magnetic field, both oriented along the z-axis (i.e., perpendicular to the graphene sheet), σ^+ and σ^- polarizations of light correspond to left ($\hat{\boldsymbol{\epsilon}}^+$) and right ($\hat{\boldsymbol{\epsilon}}^-$) circular polarizations, respectively, with the polarization being defined from the perspective of the observer. The allowed interband optical transitions in Landau-quantized graphene for σ^+ and σ^- polarizations are sketched in Fig. 4.2.

The Kronecker Delta δ_{ξ_i,ξ_f} dictates the conserving nature of the optical selection rules on valley degree of freedom. The Kronecker Deltas $\delta_{n_f,n_i\pm1}$ express that the optical transition can only happen between Landau levels with $\Delta n = \pm 1$. The quantum number m is connected to the cyclotron orbit of electrons under magnetic fields. The Kronecker Delta δ_{m_i,m_f} prohibits the transfer of electrons in distinct cyclotron orbits. In the presence of a magnetic field, the concept of momentum conservation is modified due to the influence of the magnetic force on charged particles. In quantum mechanics, in the context of electrons in a magnetic field (as in the case of Landau levels), the relevant quantum number that dictates the behavior of the system under these conditions is not directly the usual linear momentum quantum number, but rather quantum numbers (n, m) and the angular momentum $m_z = n - m$. Since the Kronecker Delta δ_{m_i,m_f} restricts any change from m_i to m_f during optical transitions, the Landau level quantum number n directly reflects Δm_z, which corresponds to an angular momentum transfer of $\Delta m_z = \pm 1$.

4.3 Optical pump

Following the derivation developed by Wendler et al. [4], the optical excitation is mathematically expressed using the time dependent magnetic vector potential (expressed in the same *xy* plane as the graphene layer) as [5]

$$\boldsymbol{A}(t) = A_{ent}(t)\left[A_0^+\begin{pmatrix}\cos\omega t\\ \sin\omega t\end{pmatrix} + A_0^-\begin{pmatrix}\cos\omega t\\ -\sin\omega t\end{pmatrix}\right], \tag{4.16}$$

where $A_0^{\pm} \neq 0 \wedge A_0^{\mp} = 0$ ($A_0^+ = 1$, $A_0^- = 0$ or $A_0^+ = 0$, $A_0^- = 1$) represents circular polarization, $A_0^+ = A_0^-$ linear polarization, and elliptical polarization appears for any other case. The envelope function $A_{ent}(t)$ regulates the amplitude of the vector potential.

In laboratory settings, pulsed waves are often preferred over continuous waves for several compelling reasons, particularly in applications involving precision measurements, material processing, and scientific research. One primary advantage is the higher peak power that pulsed waves can achieve. Unlike continuous waves that transport energy steadily, pulsed waves concentrate energy into short bursts, allowing them to reach significantly higher peak intensities. This characteristic is crucial for applications like laser-induced breakdown spectroscopy or pulsed laser deposition, where high energy density is required to interact with materials effectively. Furthermore, pulsed waves minimize thermal damage to the target materials. Pulsed waves, with their brief bursts of energy, reduce the overall heat exposure, making them ideal for delicate materials or processes. Pulsed waves also offer better temporal resolution, which is vital in time-resolved spectroscopy and other applications where understanding the dynamics of fast processes is essential. The ability to produce extremely short pulses, sometimes in the femtosecond range, allows researchers to observe and measure rapid phenomena that would be impossible with continuous wave illumination. In the context of this Thesis, the carrier relaxation mechanisms immediately after the optical excitation are of utmost interest so that the choice of pulsed waves is essential and study of graphene carrier dynamics upon illumination of pulsed waves has to be thoroughly investigated.

The form of envelope function for a Gaussian pulse is described by

$$A_{env}(t) = \left(\sigma_t\sqrt{2\pi}\right)^{-1} e^{-t^2/2\sigma_t^2}, \tag{4.17}$$

where σ_t regulates the Gaussian pulse width and has a definite relation with the experimental accessible quantity full width at half maximum (FWHM) σ_{FWHM}. The pre-factor $\left(\sigma_t\sqrt{2\pi}\right)^{-1}$ guarantees that the envelope function is normalized to 1, i.e., $\int_{-\infty}^{\infty} dt\, A_{env}(t) = 1$.

In order to assign values to the width and amplitude of the envelope function $A_{env}(t)$, the relation between the experimental settings and the pulse parameters has to be given. In experiment, usually the width of the pulse intensity $I(t)$ is measured to characterize the broadening of the pulse and an ϵ_{pf} to identify the pump fluence. The pulse intensity, which indicates the optical power transfer per unit area, can be determined by according to $I(t) = \epsilon_0 c|\boldsymbol{E}(t)|^2$. The electric field $\boldsymbol{E}(t) = -\partial_t \boldsymbol{A}(t)$ is calculated using the magnetic vector potential in Eq. 4.16 for circular polarization as

$$\boldsymbol{E}^{\pm}(t) = -\frac{A_0^{\pm}}{\sigma_t\sqrt{2\pi}} e^{-\frac{t^2}{2\sigma_t^2}} \left[\omega \begin{pmatrix} -\sin\omega t \\ \pm\cos\omega t \end{pmatrix} - \frac{t}{\sigma_t^2}\begin{pmatrix} \cos\omega t \\ \pm\sin\omega t \end{pmatrix}\right]. \tag{4.18}$$

Usually for Gaussian pulses, the condition $\sigma_t \gg T$ (the period of sinusoidal oscillating part of the electric field) always holds. Therefore, there is $t/\sigma_t^2 \ll \omega$, namely, the second item of the electric field is negligible comparing to the first item. Thus, the FWHM of the pulse intensity satisfies $e^{-\sigma_{\mathrm{FWHM}}^2/2\sigma_t^2} = 1/2$ which resolves $\sigma_{\mathrm{FWHM}} = 2\sqrt{2\ln 2}\sigma_t$. The presumed condition $\sigma_t \gg T$ is then use throughout the thesis.

The integration of the intensity over time gives rise to the optical energy transfer per unit area

$$\epsilon_{pf} = \int_{-\infty}^{\infty} dt\, I(t). \tag{4.19}$$

For circular polarization, using only the first part of electric field in Eq. 4.18 and $I(t) = \epsilon_0 c|\boldsymbol{E}(t)|^2$, it reads

$$\epsilon_{pf} = \frac{\epsilon_0 c\left(A_0^{\pm}\right)^2 \omega^2}{2\sqrt{\pi}\sigma_t}. \tag{4.20}$$

Therefore, the amplitude of the vector potential $A_0^{\pm}$ can be expressed in terms of the pump fluence ϵ_{pf} by

$$A_0^{\pm} = \frac{1}{\omega}\sqrt{\frac{2\sqrt{\pi}\sigma_t \epsilon_{pf}}{\epsilon_0 c}}. \tag{4.21}$$

Finally, the amplitude $A_0^{\pm}$ is redefined and included into the envelope function of the pulse $A_{env}(t)$ using $\sigma_{\mathrm{FWHM}} = 2\sqrt{2\ln 2}\sigma_t$ as

$$A_{env}(t) = \frac{1}{\omega}\sqrt{\frac{2\sqrt{\ln 2}\epsilon_{pf}}{\sqrt{\pi}\epsilon_0 c\sigma_{\mathrm{FWHM}}}}\, e^{-\frac{2\ln 2\, t^2}{(\sigma_{\mathrm{FWHM}})^2}}, \tag{4.22}$$

where $A_0^{\pm}$ is defined to be 0 or 1. Therefore, the vector potential of a circularly polarized Gaussian pulse can be rewritten as

$$\boldsymbol{A}^{\pm}(t) = A_{ent}(t)\begin{pmatrix}\cos\omega t \\ \pm\sin\omega t\end{pmatrix}, \tag{4.23}$$

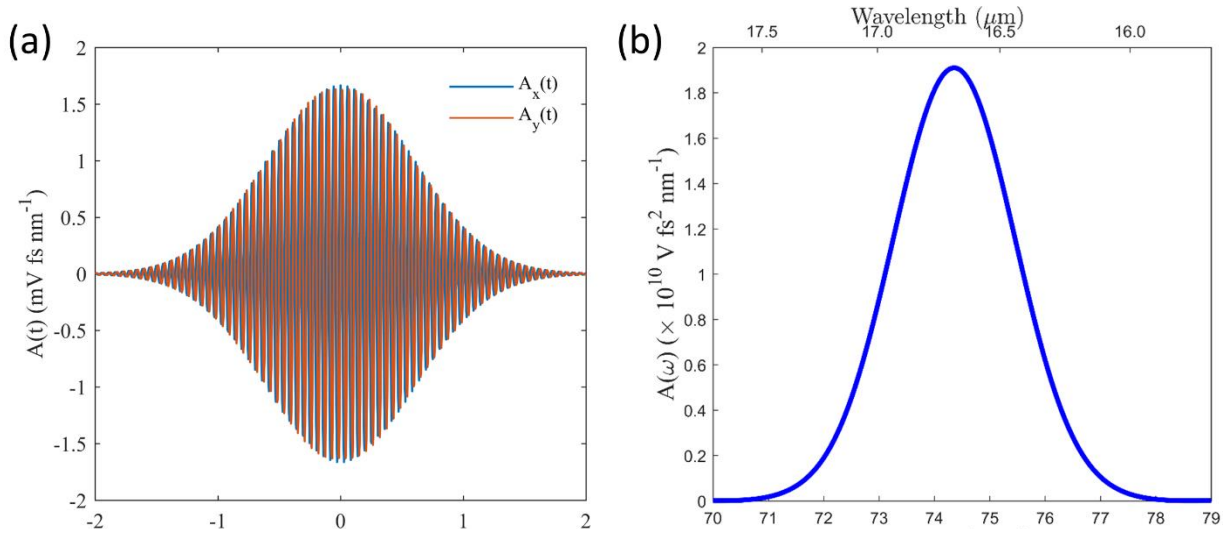

Figure 4.3 (a) The x and y components of the vector potential and (b) the spectrum of the x component of a left-handed circularly polarized Gaussian pulse with a pump fluence $\epsilon_{pf} = 0.01$ μJcm^{-2} and width $\sigma_{\mathrm{FWHM}} = 1$ ps. The photon energy is 74.4 meV, which is in resonance with the transition between the first two Landau levels LL_0 and LL_{+1} under a magnetic field $B = 4.0$ T.

with the envelope function $A_{env}(t)$ given by Eq. 4.22 and the condition $\sigma_t \gg T$. The x and y components of a left-handed circularly polarized Gaussian pulse are plotted in Fig. 4.3 with a pump fluence $\epsilon_{pf} = 0.01$ μJcm^{-2} and width $\sigma_{\mathrm{FWHM}} = 1$ ps. The photon energy is 74.4 meV, which is in resonance with the transition between the first two Landau levels LL_0 and LL_{+1} under a homogeneous magnetic field $B = 4.0$ T. The amplitude of the fast-oscillating cosine part of the vector potential is modulated by a Gaussian profile. If the width of the Gaussian profile function is large enough to an extent that the spectrum of the modulated signal is narrow as to the off-resonant transitions among the higher Landau levels are least addressed, such pumping condition would be considered ideal. If the pulse is narrow in the time domain (small width), it will have a broad spectrum in the frequency domain. This broadening is due to the Fourier transform relationship, where a shorter pulse has a wider range of frequency components. However, for realistic experimental settings, the pulse width has to be traded off between the spectrum broadening with a high temporal resolution and minimized spectrum at a cost of delivering too

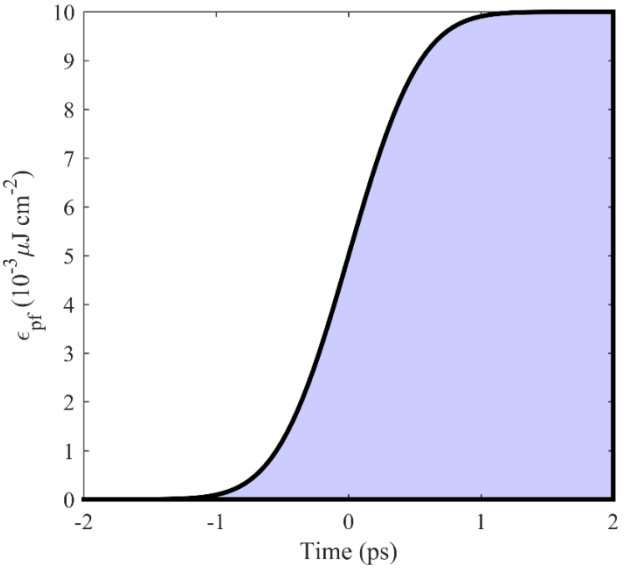

Figure 4.4 The building up of energy density with a total pumping fluence $\epsilon_{pf} = 0.01\ \mu J cm^{-2}$ and pulse width $\sigma_{FWHM} = 1$ ps.

much energy to the materials. Therefore, it is crucial to investigate the spectrum of the optical pulse by taking the Fourier transform of the vector potential. The spectrum of the x component of the vector potential for the same Gaussian-modulated cosine pulse is plotted in Fig. 4.3. With the pulse width on picosecond timescales, the spectrum spreads narrow compared to the spacing between Landau levels LL_0 and LL_{+1} and is of the same order as the Landau level broadening induced by the carrier-impurity scattering. Therefore, it is reasonable to neglect the couplings between the off-resonant frequency components in the spectrum and the optical transitions among the higher Landau levels and thus using a Gaussian pulse as short as picosecond timescales is considered to be safe.

The optical energy density is also calculated by integrating the pulse intensity $I(t)$ over the pulse duration using Eq. 4.19. For circular polarization, using the vector potential in Eq. 4.23, the building up of energy density over time is illustrated in Figure. 4.4.

4.4 Light-carrier interactions

Combining the free energy and light-carrier interaction, the Hamiltonian of electrons in Landau-quantized graphene is given by [2]

$$H = \sum_i \epsilon_i a_i^\dagger a_i + i\hbar \frac{e_0}{m_0} \sum_{i,f} \boldsymbol{M}_{if} \cdot \boldsymbol{A}(t)\, a_f^\dagger a_i, \tag{4.24}$$

where $\epsilon_i \approx 2.8\ eV$ is the is the hopping integral. The microscopic polarization $p_{if} = \langle a_f^\dagger a_i \rangle(t)$ is the off-diagonal matrix element of the density operator and is a measure of the transition probability from the initial state i to the final state f with an initial value of zero, while $\rho_i = \langle a_i^\dagger a_i \rangle(t)$ is the occupation of state i which in thermal equilibrium is given by the Fermi-Dirac distribution. The above Hamiltonian is used to obtain the microscopic equations of motion (or Bloch equations) for the density matrix elements as [3]

$$\dot{p}_{if} = \frac{i}{\hbar}(\epsilon_f - \epsilon_i) p_{if} + \frac{e_0}{m_0} \sum_l \left[\boldsymbol{M}_{li} p_{lf} - \boldsymbol{M}_{fl} p_{il} \right] \cdot \boldsymbol{A}(t), \tag{4.25}$$

Using the relation $\boldsymbol{M}_{if} = -\boldsymbol{M}_{fi}^*$ obtained from Eq. 4.15 and considering that the polarization only couples to itself or occupation $\rho_i = p_{ii}$, two separates yet coupled equations of motion (EOM) can be derived from Eq. 4.25 for polarizations and occupations [3]:

$$\dot{\rho}_i|_{\text{light}} = -2 \sum_l \text{Re}[\Omega_{il} p_{il}], \tag{4.26}$$

$$\dot{p}_{if}\big|_{\text{light}} = i\Delta\omega_{if} p_{if} - \Omega_{if}^* (\rho_f - \rho_i). \tag{4.27}$$

The energy difference $\hbar\Delta\omega_{if} = \epsilon_f - \epsilon_i$ is the difference between the final and initial states and describes the inherent oscillating part of the polarization p_{if} due to the free energy part of the Hamiltonian. The Rabi frequency $\Omega_{if} = (e_0/m_0)\boldsymbol{M}_{if} \cdot \boldsymbol{A}(t)$ is a fundamental concept in quantum mechanics and quantum optics, particularly relevant in the context of two-level systems interacting with an electromagnetic field. It quantifies the rate of oscillation (transition) between two states under the influence of an external oscillating field, like a laser or a microwave. The frequency of the electromagnetic field is typically close to the resonance frequency (energy difference) between the two states. Under the influence of the field, the quantum system undergoes oscillations between the two states, known as Rabi oscillations. The probability of finding the system in a particular state oscillates sinusoidally at this frequency.

4.5 Rabi oscillations in the Rotating Wave Approximation (RWA)

The Rotating Wave Approximation (RWA) is a widely used simplification in quantum mechanics and quantum optics, particularly in the context of systems interacting with oscillating electromagnetic fields, such as in the study of atomic and molecular spectroscopy, laser physics, and quantum information processing. It is used to simplify the mathematical description of the interaction between a quantum system and an electromagnetic field. In quantum systems driven by an oscillating field, the Hamiltonian typically contains terms that oscillate at very high frequencies. The RWA simplifies this Hamiltonian by keeping only the terms that vary slowly over time and neglecting the ones that oscillate rapidly. This approximation is valid when the frequency of the driving field is close to the resonance frequency of the quantum system. The RWA significantly simplifies the mathematical treatment of the system. It allows for easier calculation of Rabi frequencies, understanding of Rabi oscillations, and analysis of quantum coherence and entanglement in driven systems.

To this end, the microscopic Bloch equations for Landau-quantized graphene without a dephasing term in the polarization can be solved analytically using RWA and helps understand how the carrier dynamics evolves under optical driving field. Using the substitution $p_{if} = p_{if}^{\mathrm{rot}} e^{i\Delta\omega_{if}t}$, Eq. 4.26 and 4.27 can be written as [3]

$$\dot{\rho}_{if}^{\mathrm{rot}} = -2\sum_{l} \mathrm{Re}[\Omega_{il}^{\mathrm{rot}} p_{il}^{\mathrm{rot}}], \tag{4.28}$$

$$\dot{p}_{if}^{\mathrm{rot}} = -\left(\Omega_{if}^{\mathrm{rot}}\right)^{*}\left(\rho_{f}^{\mathrm{rot}} - \rho_{i}^{\mathrm{rot}}\right), \tag{4.29}$$

where the definition $\Omega_{if}^{\mathrm{rot}} = \Omega_{if} e^{i\Delta\omega_{if}t}$ is used. For a resonant excitation in the RWA the Rabi frequency can be written as

$$\Omega_{if}^{rot}\big|_{RWA} = i\delta_{\tau_i\tau_f}\delta_{m_i,m_f}\frac{\alpha_{n_i}\alpha_{n_f}e_0 v_F A_{env}(t)}{4\hbar}\Big(v_i\delta_{n_f,n_i+1}A_0^{-} + v_f\delta_{n_f,n_i-1}A_0^{+}\Big) = i\bar{\Omega}_{if}^{rot}, \tag{4.30}$$

where the real quantity $\bar{\Omega}_{if}^{\mathrm{rot}} = Im\left[\Omega_{if}^{\mathrm{rot}}\big|_{\mathrm{RWA}}\right]$ is used to simplify the equation of motion (EOM) in the RWA. Eq. 4.28 and 4.29 are written as

$$\dot{\rho}_{i}^{rot} = -2\sum_{l} Re\left[\Omega_{if}^{rot} p_{if}^{rot}\right], \tag{4.31}$$

$$\dot{p}_{if}^{rot} = i\bar{\Omega}_{if}^{rot}\left(\rho_{f}^{rot} - \rho_{i}^{rot}\right). \tag{4.32}$$

Eq. 4.31 informs that $\dot{p}_{if}^{\mathrm{rot}}$ is purely imaginary due to the resonant driving field and no dephasing in polarization. the EOM are written for the new quantities $v_{if} = 2Im\left[p_{if}^{\mathrm{rot}}\right]$, and $w_{if} = \left(\rho_f^{\mathrm{rot}} - \rho_i^{\mathrm{rot}}\right)$ which yields [3]

$$\dot{w}_{if} = \sum_{ll'} \left(\bar{\Omega}_{fl}^{rot} v_{fl} - \bar{\Omega}_{il'}^{rot} v_{il'}\right), \tag{4.33}$$

$$\dot{v}_{if} = 2\bar{\Omega}_{if}^{rot} w_{if}. \tag{4.34}$$

The discussion is restricted to a single transition $i \to f$. Furthermore, the relations $v_{fi} = -v_{if}$ and $\bar{\Omega}_{fi}^{\mathrm{rot}} = \bar{\Omega}_{if}^{\mathrm{rot}}$ are used. The resulting equation of motion (EOM) becomes

$$\dot{w}_{if} = -2\bar{\Omega}_{if}^{rot} v_{if}, \tag{4.35}$$

$$\dot{v}_{if} = 2\bar{\Omega}_{if}^{rot} w_{if}. \tag{4.36}$$

We solve the above differential equations by assuming the initial conditions $\rho_f^{\mathrm{rot}}(t = -\infty) = 0$, $\rho_i^{\mathrm{rot}}(t = -\infty) = 1$, $p_{if}^{\mathrm{rot}}(t = -\infty) = 0$

$$w_{if}(t) = -cos\left[\Theta_{if}(t) - \alpha\right], \tag{4.37}$$

$$v_{if}(t) = -sin\left[\Theta_{if}(t) - \beta\right], \tag{4.38}$$

where the quantities α and β are introduced to help account for the initial conditions and have to be solved accordingly. The phase term $\Theta_{if}(t)$ of a pulse refers to the initial phase angle of the electromagnetic wave used in the pulse. In quantum mechanics, this phase determines the axis of

rotation on the Bloch sphere (a geometric representation of the state space of a two-level quantum system). The phase can be thought of as specifying the direction in which the quantum state rotates when a pulse is applied and is related to the Rabi frequency by the integral

$$\Theta_{if}(t) = 2\int_{-\infty}^{t} dt' \bar{\Omega}_{if}^{rot}(t'), \tag{4.39}$$

Let us consider a circularly polarized Gaussian pulse modulated by the envelope function described by Eq. 4.22. Then, we can substitute the expression for Rabi frequency in Eq. 6.30 into the integration performed in Eq. 4.39 to obtain [3]

$$\Theta_{if}(t) = \frac{e_0 v_F}{2\hbar\omega}\sqrt{\frac{\epsilon_{pf}\sqrt{\pi}\sigma_{FWHM}^{exp}}{\epsilon_0 c\sqrt{ln2}}}\left[erf\left(\frac{\sqrt{2ln2}}{\sigma_{FWHM}^{exp}}t\right)+1\right]. \tag{4.40}$$

Thus, one can plot the temporal evolution of microscopic polarizations and occupations with the help of $\Theta_{if}(t)$ function. Such relations are given by

$$\rho_i(t) = \frac{1}{2} + \frac{1}{2}cos\left[\Theta_{if}(t)\right], \tag{4.41}$$

$$\rho_f(t) = \frac{1}{2} - \frac{1}{2}cos\left[\Theta_{if}(t)\right], \tag{4.42}$$

$$p_{if}(t) = -\frac{i}{2}sin\left[\Theta_{if}(t)\right]e^{i\Delta\omega_{if}t}, \tag{4.43}$$

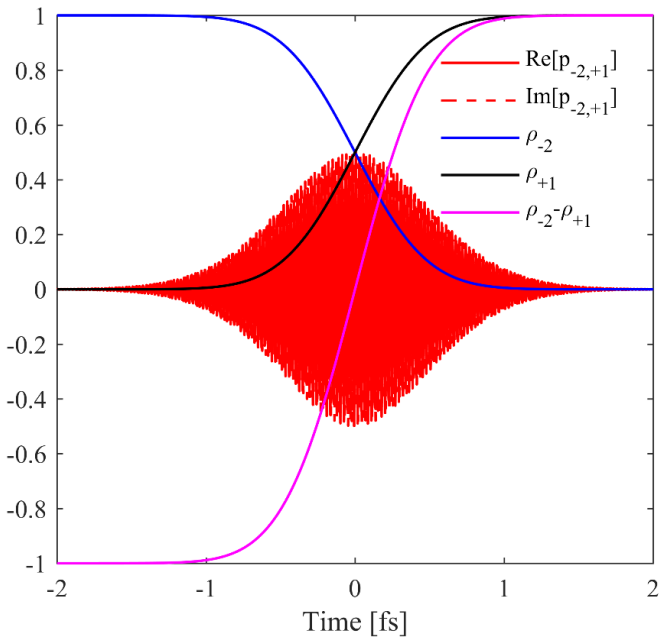

Figure 4.5 Occupations of a two level-system ρ_{-2}, ρ_{+1} and the population inversion $\rho_{+1} - \rho_{-2}$ and the polarization $P_{-2,+1}$ over a π-pulse oscillation. The system is resonantly driven by a Gaussian pulse.

when $\Theta_{if}(t)$ completes a π-phase from $n\pi$ to $(n+1)\pi$, the two-level system flips state. Therefore, a π-pulse is defined as an electromagnetic pulse that is precisely tuned such that its duration and strength cause a complete transition from one quantum state to another, i.e., $\Theta_{if}(t = \infty) = \pi$. It is named a π-pulse because the area of the pulse in a Rabi frequency-time plot is π. In other words, if a system starts in state $|1\rangle$, a π-pulse will flip it completely to state $|2\rangle$ and vice versa. In addition to π-pulses, there are also $\pi/2$-pulses and 2π-pulses. A $\pi/2$-pulse brings the system into a superposition of states, while a 2π-pulse returns the system to its original state after completing two full Rabi cycles. The temporal evolution of a two-level system comprised of LL_{-2} and LL_{+1} is plotted for a π-pulse in Figure. 4.5. As is seen, the system achieves population inversion after a $\pi/2$-pulse and ultimately reaches full inversion when π-pulse is done. After a second π-pulse, it will result in the returning of the two-level system back to its original state, as is illustrated in Figure. 4.6. After the π-pulse, if the external field continues to be applied, the

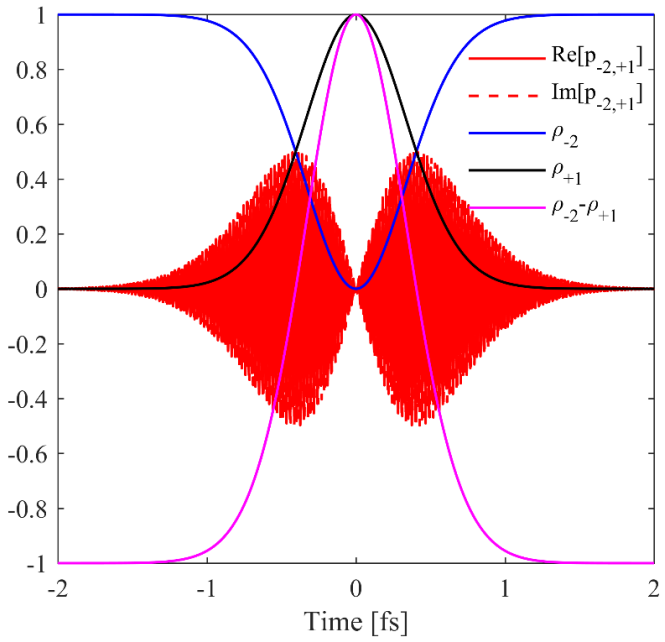

Figure 4.6 Occupations of a two level-system ρ_{-2}, ρ_{+1} and the population inversion $\rho_{+1} - \rho_{-2}$ and the polarization $P_{-2,+1}$ over a 2π-pulse oscillation. The system is resonantly driven by a Gaussina pulse.

system can undergo further Rabi oscillations. This means that it can be excited again (or de-excited) depending on its current state and the characteristics of the ongoing external field. As seen from the second π-pulse, the two occupations start to reverse their state. It is not regarded as a direct result of stimulated emission as it occurs in lasers. Instead, it is a consequence of the ongoing interaction with the external driving field, which continues to drive Rabi oscillations. This process is more about the coherent absorption and re-emission of energy due to the driving field rather than stimulated emission due to external photons.

4.6 The initial states

Before the numerical investigation of the microscopic Bloch equations, one more issue needs to be solved, which is the initial conditions for both occupations and polarizations. It is reasonable to assume that the polarizations stay on zero value right before the optical excitation. However,

the initial occupation on the discrete Landau levels needs to be known. The density of states (DOS) of pristine graphene is govern by the linear relation with respect to the energy, given by [10][11]

$$\rho(E) = g_s g_v \frac{|E|}{2\pi\hbar^2 v_F^2}, \tag{4.44}$$

where the degeneracies of spin and valley degree of freedom g_s and g_v have been accounted for. The carrier concentration can be calculated by integration of DOS with respect to the energy as

$$n_c(E_F) = \int_0^{E_F} \rho(E)dE = \frac{1}{2} g_s g_v \frac{E_F^2}{2\pi\hbar^2 v_F^2}, \tag{4.45}$$

where the carrier concentration can be experimentally obtained using Hall measurements. Thus, the Fermi energy is readily known from the above relation. Upon applying external magnetic field, the DOS no longer follows the linear relation, and the carrier population has to redistributed among discrete Landau levels. With moderate doping, the filling factor of the zeroth Landau level is neither vanishing nor close to one. To begin with, the degeneracy of each Landau level at a constant magnetic field B is given by [12]

$$G(B) = \frac{eB}{h}, \tag{4.46}$$

excluding the spin and valley degeneracy. For completely filled zeroth Landau level, the degeneracy is calculated as $4.06 \times 10^{11}\text{cm}^{-2}$ for $B = 4.0\ T$. For zero magnetic field, this corresponds to a Fermi level of $74\ meV$. Note that for undoped graphene, the filling factor for the zeroth Landau level $\rho_0 = 0.5$, corresponding to an intrinsic carrier concentration of $2.03 \times 10^{11}\text{cm}^{-2}$ on this level. If an excess carrier concentration is measured to be $6 \times 10^{10}\,\text{cm}^{-2}$, i.e., the Fermi level $E_F = 29\ meV$ at $B = 0$. Then, the filling factor at $B = 4.0\ T$ is calculated as $\rho_0 =$

$2.63 \times \frac{10^{11}\,\mathrm{cm}^{-2}}{4.06} \times 10^{11}\mathrm{cm}^{-2} = 0.648$. For such initial settings, the populations of the positive and negative Landau level can be reasonably assumed to be 0 and 1.

4.7 Carrier-carrier scattering

Coulomb-induced carrier–carrier interaction refers to the interaction between charge carriers in a material due to the Coulombic repulsion. The interaction is described by the Hamiltonian [3]

$$H_{Coul} = \frac{1}{2} \sum_{ii'ff'} V_{ff'}^{ii'} a_f^{\dagger} a_{f'}^{\dagger} a_{i'} a_i. \tag{4.47}$$

The definition of the ladder operators $a_f^{\dagger}$, $a_{f'}^{\dagger}$, $a_{i'}$ and a_i can be found in Eq. 4.3. $V_{ff'}^{ii'}$ refers to the Coulomb matrix element and is used to describe the strength of the Coulombic interaction between two charged particles. The Fourier representation of the Coulomb matrix element from is given by [13]

$$V_{34}^{12} = \sum_{\boldsymbol{q}} V_{\boldsymbol{q}} \Gamma_{13}(\boldsymbol{q}) \Gamma_{24}(-\boldsymbol{q}), \tag{4.48}$$

$$\Gamma_{if}(\boldsymbol{q}) = \int d\boldsymbol{r} \Psi_f^*(\boldsymbol{r}) e^{i\boldsymbol{q}\boldsymbol{r}} \Psi_i(\boldsymbol{r}), \tag{4.49}$$

where $V_{\boldsymbol{q}} = e_0^2/2\epsilon_0 A|\boldsymbol{q}|$ is the Fourier transform of the Coulomb potential $V_{Coul} = e_0^2/4\pi\epsilon_0|\boldsymbol{r} - \boldsymbol{r}'|$. The sum over $\boldsymbol{q}$ can be transformed into an integral using the relation $A/(2\pi)^2 \sum_{\boldsymbol{q}} \rightarrow \int d\boldsymbol{q} = \int d\varphi \int q dq$ An explicit expression for the Coulomb matrix element in polar coordinates $\boldsymbol{q} = (q, \phi)$ is written as [4]

$$V_{34}^{12} = \alpha_{n_1}\alpha_{n_2}\alpha_{n_3}\alpha_{n_4}\frac{e_0^2\delta_{\xi_1,\xi_3}\delta_{\xi_2,\xi_4}}{32\pi^2\epsilon_0}\int_0^\infty dq\int_0^{2\pi}d\varphi$$

$$\times\left[\lambda_1\lambda_3\langle n_3-1,m_3|e^{i\boldsymbol{q}\hat{\boldsymbol{R}}}|n_1-1,m_1\rangle+\langle n_3,m_3|e^{i\boldsymbol{q}\hat{\boldsymbol{R}}}|n_1,m_1\rangle\right] \tag{4.50}$$

$$\times\left[\lambda_2\lambda_4\langle n_4-1,m_4|e^{i\boldsymbol{q}\hat{\boldsymbol{R}}}|n_2-1,m_2\rangle+\langle n_4,m_4|e^{i\boldsymbol{q}\hat{\boldsymbol{R}}}|n_2,m_2\rangle\right],$$

with form factor $\langle n_3-1,m_3|e^{\pm i\boldsymbol{q}\hat{\boldsymbol{R}}}|n_1-1,m_1\rangle$ given by [14]

$$\langle nm|e^{\pm i\boldsymbol{q}\hat{\boldsymbol{R}}}|n'm'\rangle=(-1)^{\Theta(\pm n'\mp n)+\Theta(\pm m'\mp m)}e^{-l_B^2q^2/2}$$

$$\times\sqrt{\frac{min(m',m)!}{max(m',m)!}}\left(\frac{l_Bq}{\sqrt{2}}\right)^{|m-m'|}e^{-i\varphi(m'-m)}L_{min(m,m')}^{|m-m'|}\left(\frac{l_B^2q^2}{2}\right) \tag{4.51}$$

$$\times\sqrt{\frac{min(n',n)!}{max(n',n)!}}\left(\frac{l_Bq}{\sqrt{2}}\right)^{|n-n'|}e^{i\varphi(n'-n)}L_{min(n,n')}^{|n-n'|}\left(\frac{l_B^2q^2}{2}\right),$$

where L_n^α denotes the generalized Laguerre polynomial and Θ stands for the Heaviside step function with the unambiguously defined value at zero, i.e., $\Theta(0)=1$. The exponential term $e^{-l_B^2q^2/2}$ in the form factor, often referred to as the "exponential suppression factor," is associated with the Coulomb interaction between charged particles. It arises from the long-range nature of the Coulomb potential. The exponential term restricts the allowed momentum transfers in scattering processes. High momentum transfers are less likely to be affected by long-range Coulomb interactions and are often associated with short-range processes. The calculation of the integral over ϕ give rise to the Kronecker delta

$$\int_0^{2\pi} d\varphi\, e^{-i\varphi(m_1-m_3)} e^{i\varphi(n_1-n_3)} e^{-i\varphi(m_2-m_4)} e^{i\varphi(n_2-n_4)} \tag{4.52}$$

$$= 2\pi\delta_{n_1-m_1+n_2-m_2,n_3-m_3+n_4-m_4},$$

which put another restriction over the quantum numbers n and m of the carriers involved in an scattering event. To notice, the spin degree of freedom is not taken into account in the formulism. To account for that, two Kronecker deltas $\delta_{s_1,s_3}\delta_{s_2,s_4}$ have to be added into Eq. 4.50 which stand for the conservation of spin degree of freedom in a carrier scattering event.

4.7.1 Coulomb screening

In general, the Coulomb interaction, which is the electrostatic force between charged particles, can be influenced by the presence of other charges nearby. To illustrate this, consider an electron and a proton, both of which attract each other due to their opposite charges according to Coulomb's law. In a vacuum, this attractive force can extend infinitely, so these particles would still be drawn to each other even if placed far apart.

However, when other charges are in the vicinity, the interaction between the electron and the proton may be affected. For instance, if we introduce another electron near the proton, the original attraction between the electron and the proton would be partially offset by the repulsive force between the two electrons. Effectively, the positive charge of the proton becomes screened or partially shielded by the presence of the additional electron. This screening phenomenon occurs because the repulsion between electrons counteracts the attraction between opposite charges (electron and proton), leading to a modified net interaction. The screened Coulomb potential is modified according to [4]

$$V_{\boldsymbol{q}} \to \frac{V_{\boldsymbol{q}}}{\epsilon_r(\boldsymbol{q},\omega)}, \tag{4.53}$$

where relative permittivity $\epsilon_r(\boldsymbol{q},\omega)$ is the wavenumber- and frequency-dependent dielectric function which accounts for the dynamic response of the material to the Coulomb interaction. The frequency ω is associated with the energy transfer of charge carriers between the initial and final states of a transition in a scattering event, i.e., $\hbar\omega = \epsilon_3 - \epsilon_1$. The relative permittivity consists of two components: a constant part attributed to the background ϵ_{bg} and a momentum-dependent component originating from the mobile charge carriers, such as the π-bands in graphene, denoted as ϵ_c while the relation is dictated by

$$\epsilon_r(\boldsymbol{q},\omega) = \epsilon_{bg}\epsilon_c(\boldsymbol{q},\omega). \tag{4.54}$$

The background screening comes from the substrate where graphene is placed and is given by $\epsilon_{bg} = (\epsilon_{sub} + 1)/2$. The dynamic screening from the permittivity is related to both the Coulomb potential and polarizability and calculated in the random phase approximation [15]

$$\epsilon_c(\boldsymbol{q},\omega) = 1 - V_{\boldsymbol{q}}\Pi^0(\boldsymbol{q},\omega), \tag{4.55}$$

where the polarizability is calculated by

$$\Pi^0(\boldsymbol{q},\omega) = 4N_B \sum_{\lambda\lambda'}\sum_{nn'} \frac{n_{FD}\left(\varepsilon_n^{\lambda}\right) - n_{FD}\left(\varepsilon_{n'}^{\lambda'}\right)}{\varepsilon_n^{\lambda} - \varepsilon_{n'}^{\lambda'} + \hbar\omega + i\gamma^{imp}} \left|F_{\lambda n,\lambda' n'}(\boldsymbol{q})\right|^2, \tag{4.56}$$

where $n_{FD} = 1/(1 + \exp[(\epsilon - \mu_c)/k_B T])$ stands for the standard Fermi-Dirac distribution with μ_c the chemical potential and the form factor is given by [16]

$$F_{\lambda n,\lambda' n'}(\boldsymbol{q}) = \sqrt{\frac{(1-\delta_{n,0})(1-\delta_{n',0})}{4}} f_{n-1,\,n'-1}(\boldsymbol{q}) + \lambda\lambda' \sqrt{\frac{(1+\delta_{n,0})(1+\delta_{n',0})}{4}} f_{n,\,n'}(\boldsymbol{q}), \tag{4.57}$$

with

$$f_{n,\,n'}(\boldsymbol{q}) = e^{-l_B^2 q^2/4} \sqrt{\frac{min(n,n')!}{max(n,n')!}} \left(-i\frac{l_B q}{2}\right)^{|n-n'|} L_{min(n,n')}^{|n-n'|}\left(\frac{l_B^2 q^2}{2}\right). \tag{4.58}$$

The dynamical dielectric function can be numerical assessed in dependence of wavenumber $\boldsymbol{q}$ for any possible transition with given magnetic field, chemical potential and Landau level broadening. To illustrate this, consider the energy transfer $\hbar\omega = \epsilon_3 - \epsilon_1$ involving transition from LL_0 to LL_{+1}

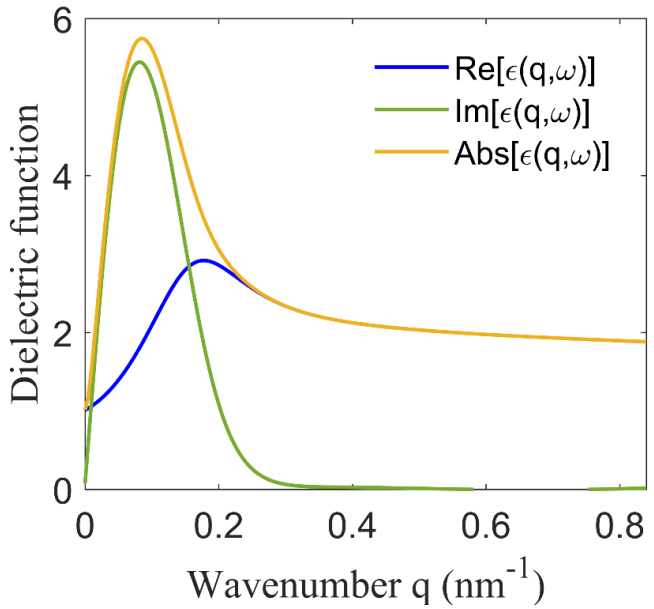

Figure 4.7 The wavenumber dependent dielectric function accounted for Coulomb screening associated with the transition from LL_0 to LL_{+1} using the parameters $B = 4.0\,T$, $\mu_c = 0$ and $\hbar\gamma^{imp} = 7\,meV$.

with the parameter settings $B = 4\ T$, $\mu_c = 0$ and $\hbar\gamma^{imp} = 7\ meV$. The wavenumber dependent response of the dynamic dielectric function is numerical calculated and plotted in Fig. 4.7.

4.7.2 Scattering rates

In this section, the damping in the population will be addressed quantitatively where the scattering rates due to the carrier-carrier interaction needs to be discussed in fully details. First of all, general Bloch equations solely account for the inward-going and outward going carriers due to Coulomb interaction are given by [17]

$$\dot{\rho}_i|_{Coul} = S_i^{in}(1-\rho_i) - S_i^{out}\rho_i, \tag{4.59}$$

$$\dot{p}_{if}\big|_{Coul} = -\left(S_i^{in} + S_i^{out} + S_f^{in} + S_f^{out}\right)p_{if}, \tag{4.60}$$

where $S_i^{in/out}$ and $S_f^{in/out}$ are the inward and outward scattering rates with regard to the initial and final states of the scattered charge carriers. Those two equations are obtained under the assumptions that the occupations only couple to other occupations, while the polarization only couple to itself and to occupations. Using the Coulomb potential discussed in last section, the explicit expressions of the scattering rates are given by [2]

$$S_f^{in}(t)\big|_{Coul} = \frac{2\pi}{\hbar}\sum_{abc} V_{bc}^{fa}\,\tilde{V}_{fa}^{bc}(1-\rho_a)\rho_b\rho_c L_\Gamma\left(\Delta E_{fabc}\right), \tag{4.61}$$

$$S_i^{out}(t)|_{Coul} = \frac{2\pi}{\hbar}\sum_{abc} V_{bc}^{ia}\,\tilde{V}_{ia}^{bc}\rho_a(1-\rho_b)(1-\rho_c)L_\Gamma(\Delta E_{iabc}). \tag{4.62}$$

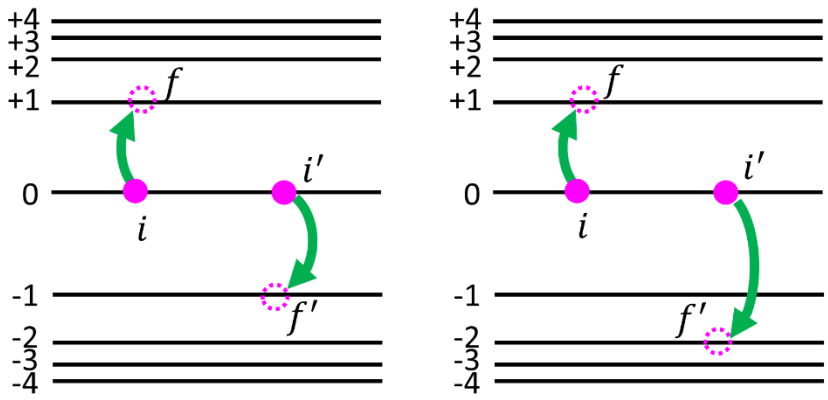

Figure 4.8 Two scattering events with vanishing and nonvanishing energy difference. The graphene is Landau quantized with an external magnetic field $B = 4.0\,T$.

The abbreviation $\tilde{V}_{ia}^{bc} = V_{ia}^{bc} - V_{ai}^{bc}$ is introduced and the terms $\rho_a(1-\rho_b)(1-\rho_c)$ or $(1-\rho_a)\rho_b\rho_c$ describe how the scattering rates of the respective process depend on the occupation of the involved levels. The notation $\Delta E_{ff'}^{ii'} = \epsilon_f - \epsilon_i + \epsilon_{f'} - \epsilon_{i'}$ in the Lorentzian plays the role of a weighting factor for the scattering rates which quantifies the difference between the two energies connected to the transitions of the involved charge carriers. Taking a closer look into this factor and considering two scattering events depicted in Fig. 4.8, the energy difference in the left panel is $\Delta E_{ff'}^{ii'} = 0$ while in the right panel it has a nonvanishing value $\Delta E_{ff'}^{ii'} = \epsilon_{-2} - \epsilon_{-1} = -30.8\,meV$. Considering a finite level broadening $\Gamma = 7\,meV$, the Lorentzian of the right case is smaller than that of the left case by an order of ~20. This is crucial since it indicates that for the scatterings involving lower levels (low n), the Lorentzian rules out those with nonvanishing energy difference $\Delta E_{ff'}^{ii'}$, leaving only those with symmetric scattering like the one in the left panel. This selection rule becomes more dominant when the broadening weakens. Therefore, it is a good approximation to consider only symmetric scattering events for lower levels. the compound index $i = (\lambda_i, n_i, m_i, \xi_i, s_i)$ is used which takes the band index λ_i, landau level number n_i, the index m_i related to the cyclotron motion, valley and spin degrees of freedom ξ_i and s_i. As mentioned in the

previous section that the Coulomb interaction is spin and in good approximation valley conserving, it is convenient to use the abbreviated index $\tilde{\imath} = (\lambda_i, n_i, m_i)$ over the occupation and polarization, rendering $\rho_{\lambda_i,n_i,m_i} = \frac{1}{2}\sum_{\xi_i}\frac{1}{2}\sum_{s_i}\rho_i$ and $\rho_{(\lambda_i,n_i,m_i),(\lambda_f,n_f,m_f)} = \frac{1}{2}\sum_{\xi}\frac{1}{2}\sum_{s}p_{if}$. Then, the sum over the initial compound index is converted to the sums over the rest three quantum numbers while averaging over the valley and spin degrees of freedom, i.e. [3],

$$\sum_{abc} V_{bc}^{fa}\,\tilde{V}_{fa}^{bc} = \frac{1}{4}\sum_{\xi_j,s_j}\sum_{abc} V_{bc}^{ja}\,\tilde{V}_{ja}^{bc}, \tag{4.63}$$

It is important to explicitly document the deriving process of conducting the averages over the valley and spin degrees of freedom since in the following chapter one may need to resolve instead of averaging them. Writing all the compound indices into the subscripts/superscripts and assuming spin-conserving and in good approximation valley-conserving, i.e., $s_j = s_b$, $s_a = s_c$ and $\xi_j = \xi_b$, $\xi_a = \xi_c$ (Kronecker deltas $\delta_{s_1,s_j}\delta_{s_2,s_4}$ and $\delta_{\xi_1,\xi_3}\delta_{\xi_2,\xi_4}$ appearing in V_{34}^{12} reflecting the spin and valley conserving nature of Coulomb scattering), the process is presented as follows

$$\begin{aligned}
&\frac{1}{4}\sum_{\xi_j,s_j}\sum_{abc} V_{bc}^{ja}\,\tilde{V}_{ja}^{bc} \\
&= \frac{1}{4}\sum_{\tilde{a}\tilde{b}\tilde{c}}\sum_{\xi_j}\sum_{\xi_a}\sum_{s_j}\sum_{s_a} V_{\tilde{b},\xi_b,s_b\ \tilde{c},\xi_c,s_c}^{\tilde{\jmath},\xi_j,s_j\ \tilde{a},\xi_a,s_a}\left(V_{\tilde{\jmath},\xi_j,s_j\ \tilde{a},\xi_a,s_a}^{\tilde{b},\xi_b,s_b\ \tilde{c},\xi_c,s_c} - V_{\tilde{a},\xi_a,s_a\ \tilde{\jmath},\xi_j,s_j}^{\tilde{b},\xi_b,s_b\ \tilde{c},\xi_c,s_c}\right) \\
&= \frac{1}{4}\sum_{\tilde{a}\tilde{b}\tilde{c}}\sum_{\xi_j}\sum_{\xi_a}\sum_{s_j}\sum_{s_a} \delta_{\xi_j,\xi_b}\delta_{\xi_a,\xi_c}\delta_{s_j,s_b}\delta_{s_a,s_c} V_{\tilde{b}\tilde{c}}^{\tilde{\jmath}\tilde{a}} \\
&\times\left(\delta_{\xi_b,\xi_j}\delta_{\xi_c,\xi_a}\delta_{s_b,s_j}\delta_{s_c,s_a} V_{\tilde{\jmath}\tilde{a}}^{\tilde{b}\tilde{c}} - \delta_{\xi_b,\xi_a}\delta_{\xi_c,\xi_j}\delta_{s_b,s_a}\delta_{s_c,s_j} V_{\tilde{a},\xi_a,s_a\ \tilde{\jmath},\xi_j,s_j}^{\tilde{b},\xi_b,s_b\ \tilde{c},\xi_c,s_c}\right)
\end{aligned} \tag{4.64}$$

$$= \frac{1}{4}\sum_{\tilde{a}\tilde{b}\tilde{c}}\sum_{\xi_j}\sum_{\xi_a}\sum_{s_j}\sum_{s_a} V_{\tilde{b}\tilde{c}}^{\tilde{j}\tilde{a}}\left(V_{\tilde{j}\tilde{a}}^{\tilde{b}\tilde{c}} - \delta_{\xi_b,\xi_a}\delta_{\xi_c,\xi_j}\delta_{s_b,s_a}\delta_{s_c,s_j}V_{\tilde{a}\tilde{j}}^{\tilde{b}\tilde{c}}\right)$$

$$= \frac{1}{4}\sum_{\tilde{a}\tilde{b}\tilde{c}} V_{\tilde{b}\tilde{c}}^{\tilde{j}\tilde{a}}\left(16V_{\tilde{j}\tilde{a}}^{\tilde{b}\tilde{c}} - 4V_{\tilde{a}\tilde{j}}^{\tilde{b}\tilde{c}}\right) = \sum_{\tilde{a}\tilde{b}\tilde{c}} V_{\tilde{b}\tilde{c}}^{\tilde{j}\tilde{a}}\left(4V_{\tilde{j}\tilde{a}}^{\tilde{b}\tilde{c}} - V_{\tilde{a}\tilde{j}}^{\tilde{b}\tilde{c}}\right)$$

$$= \sum_{\tilde{a}\tilde{b}\tilde{c}} V_{\tilde{b}\tilde{c}}^{\tilde{j}\tilde{a}}\left(4V_{\tilde{j}\tilde{a}}^{\tilde{b}\tilde{c}} - V_{\tilde{j}\tilde{a}}^{\tilde{c}\tilde{b}}\right),$$

where we have used the relation $V_{34}^{12} = V_{43}^{21}$. From now on we still use i/j instead of $\tilde{\imath}/\tilde{\jmath}$ to represent the reduced compound index $i/j = \left(\lambda_{i/j}, n_{i/j}, m_{i/j}\right)$.

4.8 Numerical investigation of microscopic Bloch equations

4.8.1 Bloch equations without dephasing and damping

As is mentioned in the beginning of this chapter that the complete solutions to the carrier dynamics have to deal with the numerical approach. As a validation to the Rabi oscillations using RWA, the carrier-light interaction is solely studied without considering either dephasing in polarizations or any damping in populations. First, a continuous wave (CW) is used with right handed circular polarization (σ^--polarized). The time evolution of the population and polarization in LL_{-1}, LL_0 and LL_{+1} is illustrated in Figure. 4.9. The σ^--polarized continuous wave is constantly driving the carrier back and forth between LL_0 and LL_{+1} which is the typical Rabi oscillation feature. The initial conditions of $\rho_{+1} = 0$, $\rho_0 = 0.647$ and $\rho_{-1} = 1$ resulted from the calculation in Section 4.6 are presumed. An apparent trend is that the polarization is maximum when the occupations in the two coupled Landau levels are evenly distributed. Another conclusion $\dot{\rho}_i|_{\text{light}} = -2\sum_l \text{Re}[\Omega_{il}p_{il}]$,we can draw from the figure is that the amplitude of the polarization is about the same as the range the population swings. The optical selection rules that are mentioned

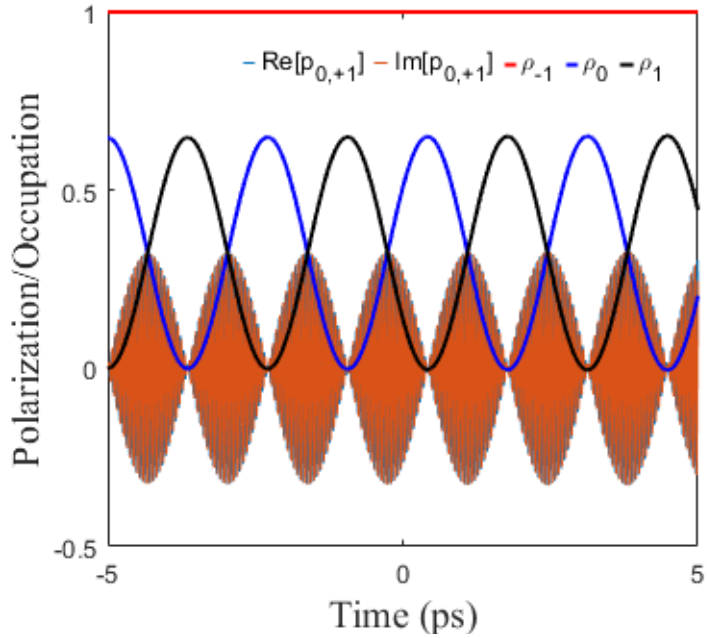

Figure 4.9 Rabi oscillation with a resonant driving field. The transfer of carrier between LL_0 and LL_{+1} is constantly happening under a σ^--polarized continuous wave. The photon energy is 74.4 meV, which is in resonance with the transition between LL_0 and LL_{+1} under a magnetic field $B = 4.0$ T.

in Section 4.2 indicates that a σ^+-polarized light would couple to the transition between LL_{-1} and

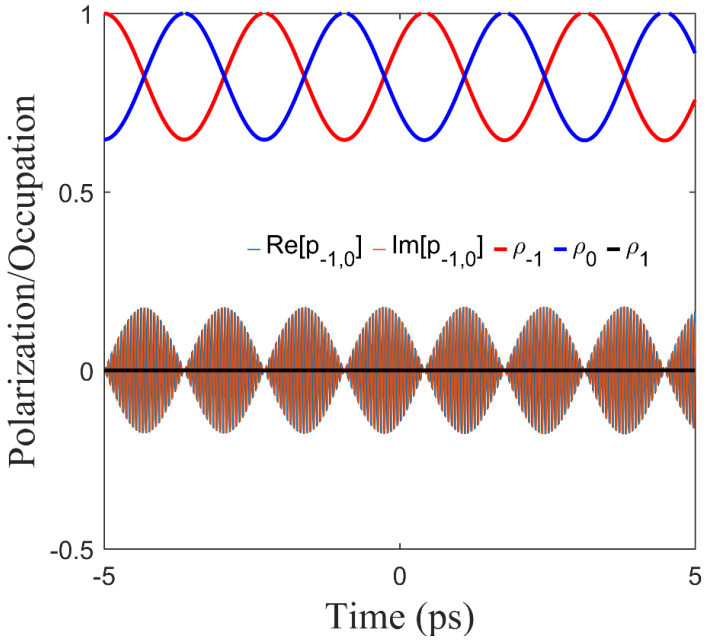

Figure 4.10 Rabi oscillation with a resonant driving field. The transfer of carrier between LL_{-1} and LL_0 is constantly happening under a σ^+-polarized continuous wave. The photon energy is 74.4 meV, which is in resonance with the transition between LL_{-1} and LL_0 under a magnetic field $B = 4.0$ T.

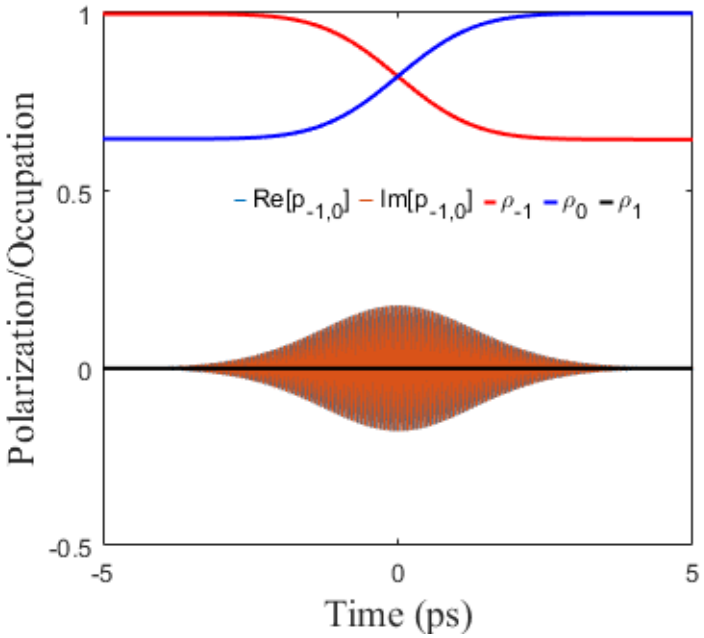

Figure 4.11 Population fluctuation over a π-pulse σ^+-polarized excitation. The photon energy is 74.4 meV, which is in resonance with the transition between LL_{-1} and LL_0 under a magnetic field $B = 4.0$ T. The pump fluence $\epsilon_{pf} = 0.005\ \mu J cm^{-2}$.

LL_0, which is in good agreement with the numerical results that are plotted in Fig. 4.10 where a σ^+-polarized continuous wave is applied.

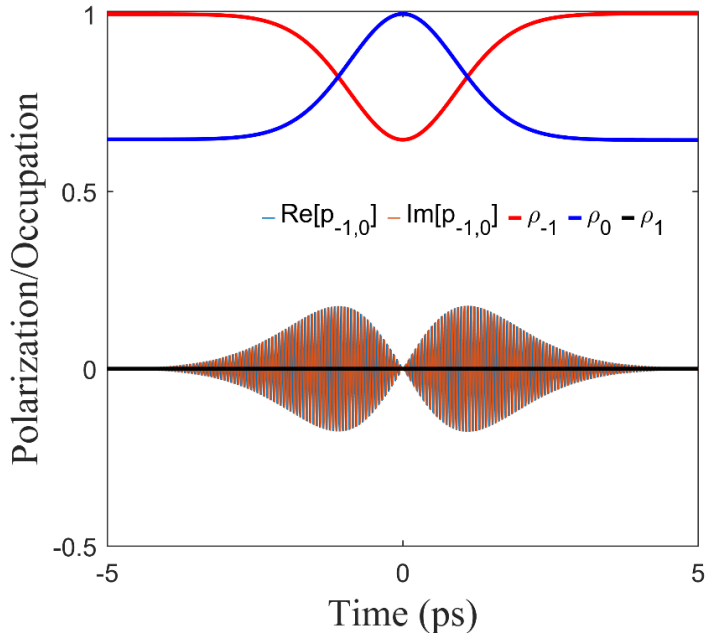

Figure 4.12 Population fluctuation over a 2π-pulse σ^+-polarized excitation. The photon energy is 74.4 meV, which is in resonance with the transition between LL_{-1} and LL_0 under a magnetic field $B = 4.0$ T. The pump fluence $\epsilon_{pf} = 0.02\ \mu J cm^{-2}$.

The carrier evolution under a resonant Gaussian π-pulse with σ^+ polarization is plotted in Fig. 4.11. The pump fluence is set to be $\epsilon_{pf} = 0.005\ \mu Jcm^{-2}$ calculated by Eq. 4.40, which is approximately a π-pulse and induces the population flip between LL_{-1} and LL_0. Using an excitation of larger pump fluence $\epsilon_{pf} = 0.045\ \mu Jcm^{-2}$ induces a 2π-pulse which drives the carriers back to their original energy level after the population flipping as shown in Fig. 4.12.

4.8.2 Bloch equations with finite dephasing

When charge carriers move through graphene, they respond to the local electric field. This response leads to a polarization effect, where the charge carriers become displaced from their equilibrium positions in response to the applied electric field. When impurities or defects such as vacancies, grain boundaries, or dislocations are present in graphene, they introduce random variations in the local electrostatic potential. These variations lead to fluctuations in the electric field experienced by charge carriers. As a result, charge carriers undergo random phase shifts as they interact with these impurity-induced electric field fluctuations. The random phase shifts induced by impurities or defects disrupt the phase coherence of charge carriers. This loss of coherence is referred to as dephasing.

Considering a finite dephasing term of polarization in the optical Bloch equations, Eq. 4.26 and 4.27 are modified as

$$\dot{\rho}_i = -2\sum_l \mathrm{Re}[\Omega_{il} p_{il}], \tag{4.65}$$

$$\dot{p}_{if} = \left(i\Delta\omega_{if} - \gamma_{if}^{imp}\right)p_{if} - \Omega_{if}^{*}\left(\rho_f - \rho_i\right), \tag{4.66}$$

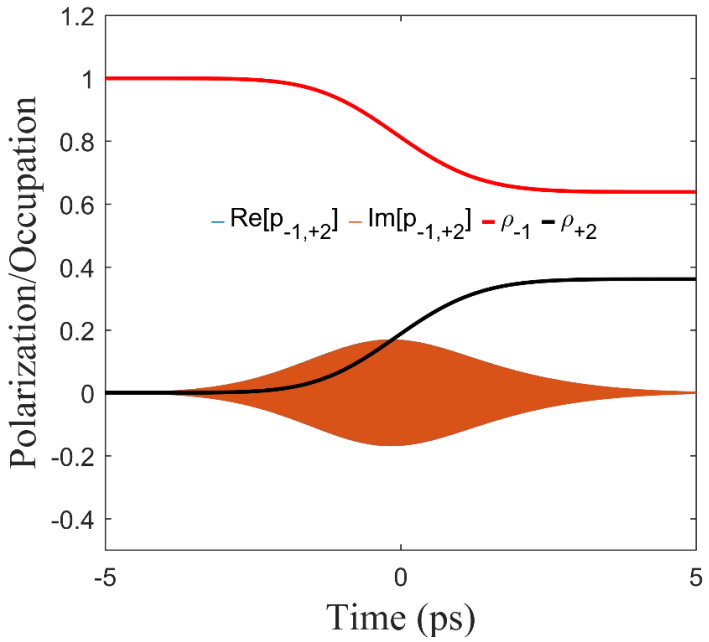

Figure 4.13 Temporal evolution of population and polarization involved in the optical transition from LL_{-1} to LL_{+2} including a finite dephasing with a π-pulse. The photon energy is 179.6 meV, which is in resonance with the transition between LL_{-1} and LL_{+2} under a magnetic field $B = 4.0$ T. The pump fluence $\epsilon_{pf} = 0.029\ \mu J cm^{-2}$.

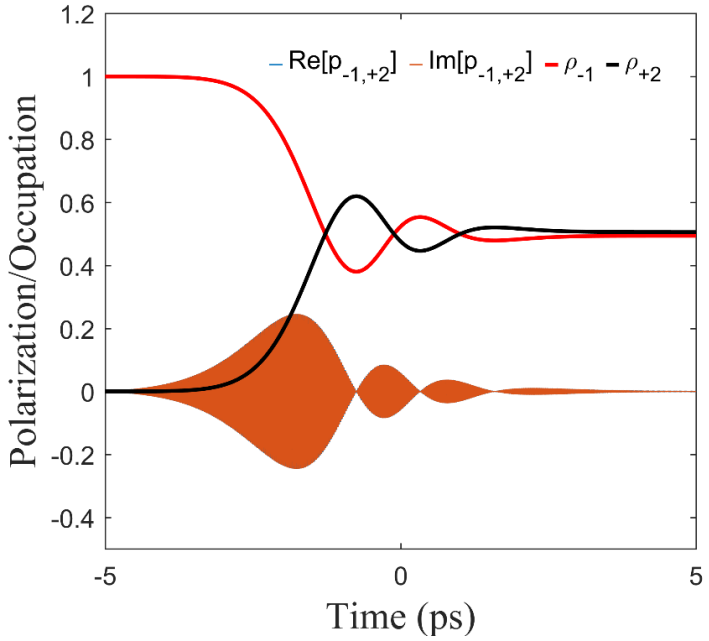

Figure 4.14 Temporal evolution of population and polarization involved in the optical transition from LL_{-1} to LL_{+2} including a finite dephasing with a 4π-pulse. The photon energy is 179.6 meV, which is in resonance with the transition between LL_{-1} and LL_{+2} under a magnetic field $B = 4.0$ T. The pump fluence $\epsilon_{pf} = 0.47\ \mu J cm^{-2}$.

where γ_{if}^{imp} is the impurity-induced dephasing rate and $\hbar\gamma_{if}^{imp}$ can be a few meV. In Eq. 4.48, the

term $-\Omega_{if}^{*}(\rho_f - \rho_i)$ builds up the polarization while $-\gamma_{if}^{imp} p_{if}$ counteracts the optical excitation, thus decreasing the effective pump fluence. In Fig. 4.13, the temporal evolution of population and polarization involved in the optical transition from LL_{-1} to LL_{+2} including a finite dephasing is plotted using a π-pulse. As a contrast, a π-pulse doesn't flip the population of LL_{-1} and LL_{+2}. Even with a 4π-pulse, the pump only induces a transient population inversion and finally levels off LL_{-1} and LL_{+2} at an equal value, as can be seen from Fig. 4.14.

4.8.3 Bloch equations with carrier-carrier scattering

In this section, the Bloch equations will incorporate carrier-carrier scattering. Due to the non-equidistant Landau levels, only the transition that closely matches the optical energy of the pump will be disturbed the most. Assume that carrier-carrier scattering only happens in Landau level 0 and ± 1, the Bloch equations of population and polarization under optical pump of σ^+ polarization can be formulated as

$$
\begin{aligned}
\dot{\rho}_{-1} &= -Re[\Omega_{-1\to 0} p_{-1\to 0}] + S_{-1}^{in}(1-\rho_{-1}) - S_{-1}^{out}\rho_{-1}, \\
\dot{\rho}_{0} &= Re[\Omega_{-1\to 0} p_{-1\to 0}] + 2S_{0}^{in}(1-\rho_{0}) - 2S_{0}^{out}\rho_{0}, \\
\dot{\rho}_{1} &= S_{1}^{in}(1-\rho_{1}) - S_{1}^{out}\rho_{1}, \\
\dot{p}_{-1\to 0} &= (i\Delta\omega_{-1\to 0} - \gamma) p_{-1\to 0} - \Omega_{-1\to 0}^{*}(\rho_0 - \rho_{-1}) \\
&\quad - \left(S_{-1}^{in} + S_{-1}^{out} + S_{0}^{in} + S_{0}^{out}\right) p_{-1\to 0}, \\
\dot{p}_{0\to 1} &= (i\Delta\omega_{0\to 1} - \gamma) p_{0\to 1} - \Omega_{0\to 1}^{*}(\rho_1 - \rho_0) \\
&\quad - \left(S_{0}^{in} + S_{0}^{out} + S_{+1}^{in} + S_{+1}^{out}\right) p_{0\to +1}
\end{aligned}
\tag{4.67}
$$

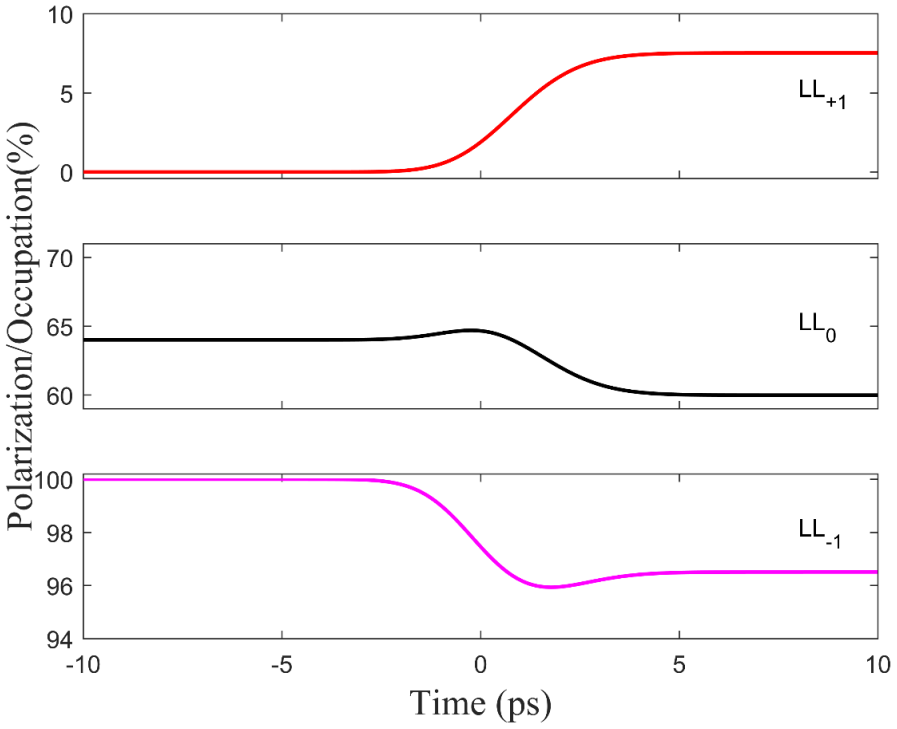

Figure 4.15 The temporal evolution of population of LL_{+1}, LL_0 and LL_{-1} including carrier-carrier scattering machnism. The photon energy of a σ^+-polarized pump is 74 meV, which is in resonance with the transition between LL_{-1} and LL_0 under a magnetic field $B = 4.0$ T. The pump fluence $\epsilon_{pf} = 0.1\ \mu J cm^{-2}$.

A factor of 2 is taken into account for LL_0 in/out-scattering rates since the total carrier concentration stays constant for the three levels and the DOS for each Landau level is the same. The temporal evolution of population in the three involved Landau levels is plotted in Fig. 4.15. After the optical excitation starts, there is a quickly increase of population in LL_0 and depopulation of LL_{-1} because they are ground and excited states of the optically-addressed transition. Meanwhile, a gradual increase of the population is also noticed in LL_{+1}, which has nothing to do directly with the optical pump. However, since there is a $(1-\rho_1)$ dependence in the in-scattering rate and ρ_1 dependence in the out-scattering rate, the net population increase in LL_{+1} is more prominent.

At this moment, the strategy as discussed in Section 3.3.2 will be adopted, namely, the pseudomagnetic field with opposite signs will be assumed for K and K' valleys respectively, without considering the specific non-uniform strain applied on graphene. As a consequence of reversing the sign of magnetic field, the optical selection rules are also reversed. Therefore, with the same polarization of the optical pump, the transition from LL_0 to LL_{+1} will be addressed instead. The corresponding temporal evolution of the population in the three involved Landau levels is also plotted in Fig. 4.16. A direct consequence of reversing the pseudomagnetic field is that the population in the same energy level within different valleys is no longer the same, which is in contrast to that of applying a uniform external magnetic field with the same magnitude to graphene. Although the non-uniform strain field doesn't guarantee a well-defined reciprocal space, the wavenumber of electrons on the same energy level within different valleys is still opposite to each other, giving rise to equal amount of carrier concentration on the same level within different

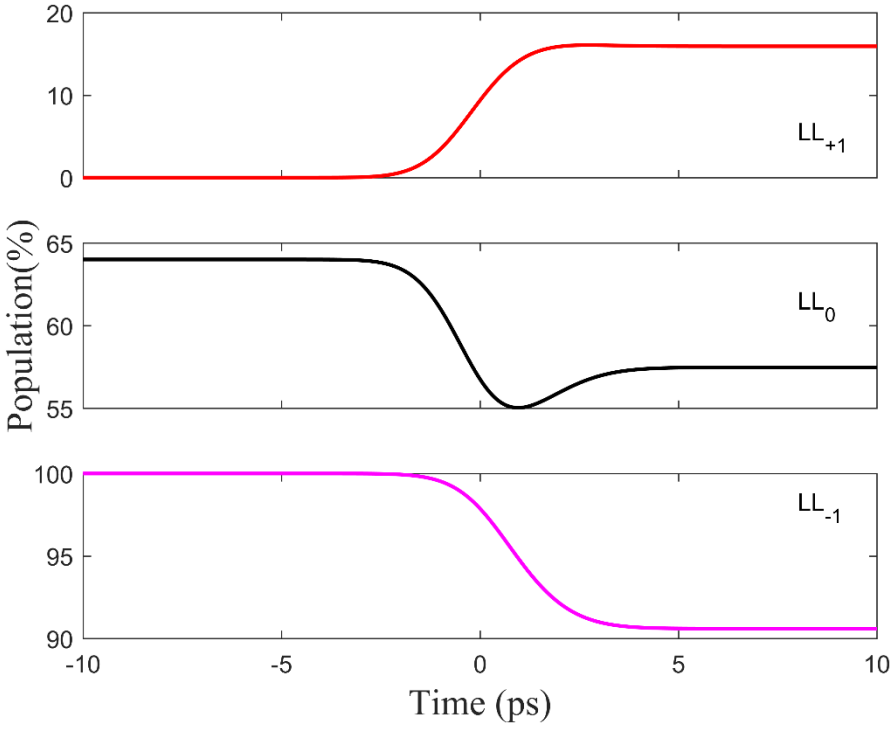

Figure 4.16 The temporal evolution of population of LL_{+1}, LL_0 and LL_{-1} reversing the pseudomagnetic field in the other valley.

valleys, which is bounded by TRS. However, the imbalanced population within the different valleys is a clear sign of broken TRS, resulting in a transient nonreciprocity in graphene. Therefore, we theoretically demonstrate the possibility of realizing nonreciprocity in graphene combing optical pump and non-uniform strain. To notice, this nonreciprocal response is transient under a Gaussian pump since the electron-phonon scattering is not included in this microscopic carrier dynamic model. But the current model is still quite accurate to capture the most prominent features of carrier dynamics happen within the first few picosecond after the pump starts. The incorporation of electron-phonon scattering will eventually bring the system back to its original thermal equilibrium state without further optical injection.

4.9 Chapter conclusions

This chapter has explored the possibility of achieving magnetless nonreciprocity combining optical pump with circular polarization and strain engineering. This attempt carries the assumption made by the last chapter that with applying certain types of non-uniform, pseudomagnetic field with same magnitude and opposite signs can be generated within the two distinct valleys of graphene, leading to Landau-quantized energy levels. However, the transitions corresponding to the same energy levels possesses different chirality. A numerical study of the Bloch equations shows that without considering damping in the population, with a given circular polarization of the optical pump whose energy matches a certain transition, only the transition in one valley will respond and the same transition in the other valley stays unperturbed. Once the carrier-carrier scattering is taken into account, more realistic carrier dynamics show completed different population of the same energy levels within the two valleys, which clearly indicates nonreciprocity happens in graphene. The successful demonstration of nonreciprocity in optical pumped and strained graphene lifts the restriction of using gapped Dirac materials for realization of

nonreciprocity. Further calculations of the Hall conductivity is desired to engineer nonreciprocal responses in graphene using modified Kubo formulism or similar approaches taking into account the explicit scattering mechanisms.

4.10 Chapter references

[1] Goerbig, M. O. "Electronic properties of graphene in a strong magnetic field." *Reviews of Modern Physics* 83.4 (2011): 1193.

[2] Kang, Dong-Ho, et al. "Pseudo-magnetic field-induced slow carrier dynamics in periodically strained graphene." *Nature Communications* 12.1 (2021): 5087.

[3] Wendler, Florian. *Ultrafast carrier dynamics in Landau-quantized graphene*. 2015. Technical University of Berlin, PhD dissertation.

[4] Wendler, Florian, Andreas Knorr, and Ermin Malic. "Ultrafast carrier dynamics in Landau-quantized graphene." *Nanophotonics* 4.3 (2015): 224-249.

[5] Funk, Hannah, et al. "Microscopic view on Landau level broadening mechanisms in graphene." *Physical Review B* 92.20 (2015): 205428.

[6] Malic, Ermin, et al. "Microscopic theory of absorption and ultrafast many-particle kinetics in graphene." *Physical Review B* 84.20 (2011): 205406.

[7] Falkovsky, Leonid Aleksandrovich. "Optical properties of graphene and IV–VI semiconductors." *Physics-Uspekhi* 51.9 (2008): 887.

[8] Vurgaftman, Igor, Matthew P. Lumb, and Jerry R. Meyer. *Bands and Photons in III-V Semiconductor Quantum Structures*. Vol. 25. Oxford University Press, 2020.

[9] Voon, Lok C. Lew Yan. *Electronic and Optical Properties of Semiconductors: A Study Based on the Empirical Tight Binding Model*. Universal-Publishers, 1997.

[10] Sounas, Dimitrios L., and Christophe Caloz. *Novel electromagnetic phenomena in graphene and subsequent microwave devices enabled by multi-scale metamaterials*. IntechOpen, 2012.

[11] Mittendorff, Martin. *Carrier relaxation dynamics in graphene*. Diss. Dresden, Technische Universität Dresden, Diss., 2014, 2015.

[12] Mittendorff, Martin, et al. "Carrier dynamics in Landau-quantized graphene featuring strong Auger scattering." *Nature Physics* 11.1 (2015): 75-81.

[13] Wendler, Florian, Andreas Knorr, and Ermin Malic. "Carrier multiplication in graphene under Landau quantization." *Nature communications* 5.1 (2014): 3703.

[14] Roldán, R., J-N. Fuchs, and M. O. Goerbig. "Collective modes of doped graphene and a standard two-dimensional electron gas in a strong magnetic field: Linear magnetoplasmons versus magnetoexcitons." *Physical Review B* 80.8 (2009): 085408.

[15] Lozovik, Yurii E., and Alexey A. Sokolik. "Influence of Landau level mixing on the properties of elementary excitations in graphene in strong magnetic field." *Nanoscale research letters* 7 (2012): 1-10.

[16] Roldán, R., M. O. Goerbig, and J. N. Fuchs. "The magnetic field particle–hole excitation spectrum in doped graphene and in a standard two-dimensional electron gas." *Semiconductor science and technology* 25.3 (2010): 034005.

[17] Wendler, Florian, and Ermin Malic. "Towards a tunable graphene-based Landau level laser in the terahertz regime." *Scientific Reports* 5.1 (2015): 12646.

5. Fundamental limits of nonreciprocal plasmonic metasurfaces

The previous chapters are mainly focused on conceptualizing a novel magnetless approach to break reciprocity in 2D materials. Based on the different biasing mechanisms, numerous nonreciprocal plasmonic metasurfaces can be constructed. However, the design of quasi-optimal devices is usually quite challenging and require significant computational resources. Given the abundant choice of materials and large degree of freedoms for geometrical shapes and dimensions, it would be highly desirable to determine the optimal response that can be achieved by a metasurface loaded with a specific nonreciprocal material. This chapter is devoted to study and unveil the fundamental bounds of linear, nonreciprocal plasmonic metasurfaces, as those illustrated in Fig. 5.1. These bounds only depend on the nonreciprocal material that compose the devices and can be obtained analytically for some configurations. The proposed approach is

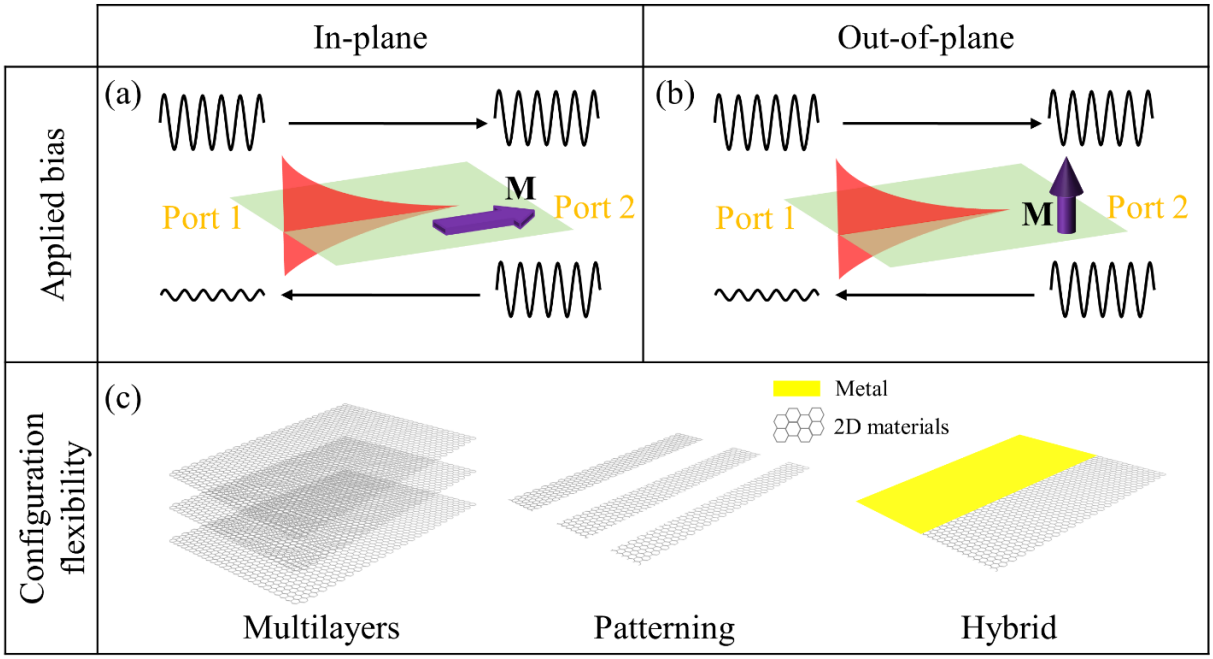

Figure 5.1 Nonreciprocal plasmonic metasurfaces based on 2D materials. The metasurfaces can be biased with an external momentum applied parallel (a) or perpendicular (b) to the structures. (c) Some potential degrees of freedom to construct plasmonic metasurfaces, including the use of multilayers of 2D materials, nanopatterning, and the inclusion of other materials such as metals or dielectrics.

general in the sense that account for different mechanisms to obtain nonreciprocity, including magnetic bias and nonlocality (for instance, obtained using drifting electrons). To this purpose, we first review the isolation equation as initially proposed in Ref. [1] and define a metric to evaluate the performance of nonreciprocal plasmonic metasurfaces in terms of isolation and loss. Then, we apply an effective medium approach (EMA) [2] to relate ultrathin metasurfaces and bulk media, which in turn permit us to obtain the upper bound of the structures in the non-retarded regime. Next, we study two different nonreciprocal plasmonic platforms: drift-biased and magnetically-biased graphene metasurfaces. For each scenario, we derive analytical upper bounds that only depend on graphene's conductivity and then we explore realistic metasurfaces studied in the literature and benchmark their performance against the bounds. Our study reveals that drift-biased hyperbolic metasurfaces have a tremendous potential for nonreciprocal plasmonics in the mid-IR, while magnetically-biased metasurfaces are better suited for the low THz band. More broadly, this approach can readily be applied to assess the performance of plasmonic metasurfaces composed of any nonreciprocal material, including magneto-optical [3] and 2D materials [4],[5], and paves the way to quick development of optimal nonreciprocal devices.

5.1 Isolation inequality

Let us consider a linear two-port network filled with arbitrary materials. Let us also consider that, upon applying any odd physical quantity (biasing), one of the materials inside of network becomes nonreciprocal. To evaluate the performance of the network, we employ the following FoM [1]

$$\gamma_{isol}\left(\underline{S}_A,\underline{S}_B,\boldsymbol{a}_A,\boldsymbol{a}_B\right) \triangleq \frac{\left|\boldsymbol{a}_B{}^T\left(\underline{S}_A-\underline{S}_B{}^T\right)\boldsymbol{a}_A\right|^2}{\boldsymbol{a}_A{}^H\left(\underline{I}-\underline{S}_A{}^H\underline{S}_A\right)\boldsymbol{a}_A\cdot\boldsymbol{a}_B{}^H\left(\underline{I}-\underline{S}_B{}^H\underline{S}_B\right)\boldsymbol{a}_B}, \tag{5.1}$$

where $\underline{S}_{A,B}$ is the scattering matrix of the network, $\boldsymbol{a}_{A,B}$ is a vector containing the excitation waves, $\underline{I}$ is the identity matrix, and the superscript T and H denote transpose and Hermitian transpose operators, respectively. Additionally, the subscripts A and B represent two distinct states of the device that are being considered to evaluate nonreciprocity. Intuitively, Eq. 5.1 provides an idea of the device nonreciprocal response (numerator) versus the power dissipated in these scenarios (denominator), i.e., a trade-off between the isolation and loss. Remarkably, the values of the FoM are delimited by an upper bound dictated only by the intrinsic properties of the nonreciprocal material filling the device. This leads to the following isolation inequality [6]:

$$\gamma_{isol}\left(\underline{S}_A, \underline{S}_B, \boldsymbol{a}_A, \boldsymbol{a}_B\right) \leq \gamma_{max}. \tag{5.2}$$

In the common case that the electric properties of the material (i.e., its permittivity tensor $\underline{\varepsilon}$) enable the nonreciprocal response, the upper bound γ_{max} is the largest eigenvalue of $\left(\underline{\varepsilon}_A^T - \underline{\varepsilon}_A^*\right)^{-1}\left(\underline{\varepsilon}_B^* - \underline{\varepsilon}_B^*\right)^{-1}\left(\underline{\varepsilon}_A - \underline{\varepsilon}_B^T\right)\left(\underline{\varepsilon}_B^* - \underline{\varepsilon}_A^H\right)$ [1]. When the network is used to maximize isolation, the incident waves associated to states A and B can be defined as $\boldsymbol{a}_A = (1 \quad 0)^T$ and $\boldsymbol{a}_B = (0 \quad 1)^T$, i.e., the device is only excited from the left or right port of the two-port network. This allows to simplify the FoM to

$$\gamma_{isol}\left(|S_{12}|, |S_{21}|\right) = \frac{(|S_{21}| - |S_{12}|)^2}{(1 - |S_{21}|^2)(1 - |S_{12}|^2)}, \tag{5.3}$$

where S_{21} and S_{12} are the transmission coefficients from port 1 to 2 and from port 2 to 1, respectively. To better illustrate the tradeoff between isolation and loss, the FoM can be expressed as

$$\gamma_{isol}(I, L) = \frac{L^2(1-I)^2}{(1-L^2)(I^2-L^2)}, \tag{5.4}$$

where $I = |S_{21}|/|S_{12}|$ is the isolation between the network ports, and $L = |S_{21}|$ is associated to the insertion loss assuming $|S_{21}| > |S_{12}|$ and perfect matching. To gain physical insight into this concept, let us consider a set of 2-port networks, all of them loaded with an identical nonreciprocal material and subjected to the same momentum bias. The performance of all networks, no matter how complex they are and what other materials they employ, will be upper bounded by γ_{max}. This bound only depends on the nonreciprocal material employed in the networks and determines the minimum loss that can be attainable in practice to achieve an isolation level I. Then, each specific network will benchmark a different performance γ_{isol} that shows how close its behavior is with respect to the fundamental limit, with $\gamma_{isol} \leq \gamma_{max}$.

In order to apply these bounds to the field of plasmonics, we consider a nonlocal and frequency-dispersive and ultrathin metasurface characterized by a fully populated conductivity tensor [7]-[9]

$$\underline{\sigma}(\omega, \boldsymbol{k}) = \begin{bmatrix} \sigma_{xx}(\omega, \boldsymbol{k}) & \sigma_{xy}(\omega, \boldsymbol{k}) \\ \sigma_{yx}(\omega, \boldsymbol{k}) & \sigma_{yy}(\omega, \boldsymbol{k}) \end{bmatrix}, \tag{5.5}$$

where ω is the angular frequency and $\boldsymbol{k}$ is the wavevector of the supported wave. Nonlocality is associated to the different response that the nonreciprocal material can potentially exhibit as a function of the momentum of the supported waves [7],[10] and, as detailed in further detail below, it is key to describe nonreciprocal systems based on drifting electrons [11],[12]. Using an effective medium approach [13], the metasurface can also be characterized as a thin dielectric layer of thickness d with a nonlocal effective permittivity tensor $\underline{\varepsilon}$,

$$\varepsilon_{zz} = \varepsilon_0, \tag{5.6}$$

$$\varepsilon_{xx\,(yy)}(\omega, \boldsymbol{k}) = 1 - j\sigma_{xx\,(yy)}(\omega, \boldsymbol{k})/(\omega d), \tag{5.7}$$

$$\varepsilon_{xy\,(yx)}(\omega, \boldsymbol{k}) = -j\sigma_{xy\,(yx)}(\omega, \boldsymbol{k})/(\omega d). \tag{5.8}$$

In the non-retarded regime (i.e., $|\boldsymbol{k}| \gg |\boldsymbol{k}_0|$, where $\boldsymbol{k}$ and $\boldsymbol{k}_0$ are the wavevectors of the supported SPPs and free space, respectively), the SPPs fields are strongly confined to the metasurface and exhibit rapidly decaying evanescent fields. In that scenario, the upper bounds of plasmonic metasurfaces can effectively be determined by analyzing the fields inside the effective anisotropic slab and determining their upper bound γ_{max}. In the following, we apply this approach to comprehensively explore two different nonreciprocal plasmonic platform, namely drift- and magnetically- biased graphene, and to analytically derive their fundamental limits as a function of graphene's properties and the applied momentum.

5.2 Application to drift-biased graphene plasmonics

An effective way to achieve broadband nonreciprocal SPPs propagation is by applying drift current to graphene-based metasurfaces [14]-[17]. Since SPPs are collective oscillations of charges interacting with light, their propagation features are strongly affected by DC current. Drifting electrons with a velocity v_d either drag or oppose the SPPs, inducing a Doppler-shifted wavenumber [12],[18]. As a result, SPPs effectively see different media when propagating along and against the drift current, leading to broadband nonreciprocity [19]. Recently, drift-biased graphene plasmonics have been experimentally demonstrated [10],[20] and attracted significant attention for various applications, including nonlinear wave generation [4] and hyperlensing [17].

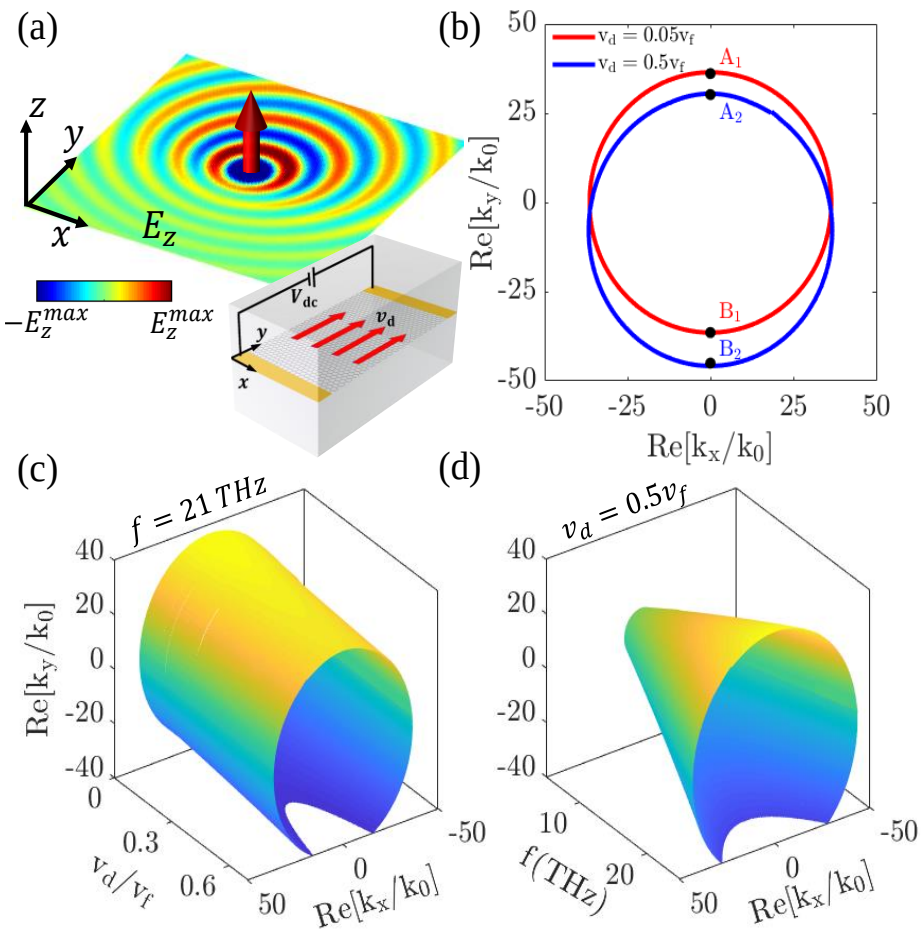

Figure 5.2 Drift-biased graphene as a nonreciprocal plasmonic metasurface. (a) Schematic showing the z-component of electric field excited by a z-oriented dipole (red arrow) located at 100 nm over a drift-biased $(v_d = 0.5\ v_F)$ graphene at 21 THz. Inset shows the device schematic. (b) Isofrequency contour of the states supported by graphene at 21 THz for two different velocities of drifting electrons. (c) and (d) Momentum of the supported states versus drift velocity and frequency, respectively. Other parameters are $\tau = 0.1\ ps$ and $\mu_c = 0.4\ eV$.

A drift-biased graphene platform is schematically shown in the inset of Fig. 5.2(a). Graphene is transferred onto a dielectric substrate (SiC [21],[22]) and two metallic electrodes (yellow bars) are printed to create electrical contact. By applying an external DC voltage across the metals, graphene is longitudinally biased by drifting electrons travelling from one electrode to the other with a velocity $\vec{v}_d = v_d\hat{y}$. Such velocity depends on the distance between the electrodes as well as graphene properties in terms of chemical potential (μ_c) and relaxation time (τ), and it is always

below the Fermi velocity of electrons in graphene ($v_F \approx 10^6$ m/s). In this scenario, graphene becomes nonlocal because its response depends on the momentum of the supported waves. Such response can be modelled using a conductivity tensor $\underline{\sigma} = \begin{pmatrix} \sigma_g & 0; & 0 & \sigma_d \end{pmatrix}$ [12], where σ_g is graphene's conductivity without the drift bias [23] and $\sigma_d(v_d, k_y) = \left[\omega/(\omega - k_y v_d)\right]\sigma_g(\omega - k_y v_d)$, with k_y being the wavevector component along the drift [14]. Nonreciprocity follows because reversing the wave travelling direction effectively means flipping the electron drifting direction, resuling in $\sigma_d(v_d, +k_y) \neq \sigma_d(v_d, -k_y)$. Probably the simpler approach to excite SPPs in this platform is to locate a *z*-oriented dipole in its near-field. We analyze this scenario using a home-made anisotropic Green's function approach developed in Ref. [12]. The z-component of the SPP's electric field excited by a dipole located at 100 nm over the metasurface is shown in Fig 5.2(a). Results show that the dipole excites waves propagating along all directions within the plane. For directions transverse to drifting electrons, i.e., $\pm x$, SPPs show a symmetric field profile. Nonreciprocity appears along the y axis, i.e., along the direction of the applied DC bias. Plasmons traveling along $+y$ are less confined that along other directions and travel longer with little loss. Remarkably, SPPs directed against the current (i.e., $-y$) are very confined and lossy, thus quickly decaying. Fig. 5.2(b) shows the isofrequency contour (IFC) of the waves supported by the platform for two different velocities of the drifting electrons. Results confirm that, as the drift velocity increases, the IFC asymmetry along k_y increases, thus leading to larger nonreciprocal responses. Points A and B in the IFC plots are associated to the wavenumber of the SPPS traveling along and against the current, respectively. Fig. 5.2(c)-(d) completes our analysis by providing a parametric study of the momentum of the supported SPPs versus drift velocity and frequency, confirming that nonreciprocity may appear over a large bandwidth.

To find the fundamental limits of drift-biased graphene-based metasurfaces, we analytically derive the isolation inequality as

$$\frac{L^2(1-I)^2}{(1-L^2)(I^2-L^2)} \leq \frac{\left|\sigma_{yy}(v_d, k_{Ay}) - \sigma_{yy}(v_d, k_{By})\right|^2}{\sigma'_{yy}(v_d, k_{Ay})\sigma'_{yy}(v_d, k_{By})} = \gamma_{max}. \tag{5.9}$$

where the superscript $'$ denotes the real parts of the conductivity component. In Eq. 5.9, the left-hand side is related to the performance of a given plasmonic device in terms of loss and isolation. The right-hand side provides the upper performance (γ_{max}) that can be attained by any metasurface that host drift-biased graphene with certain features (i.e., chemical potential, relaxation time, temperature, and velocity of drifting electrons). Remarkably, only the conductivity term associated to the drift (σ_{yy}) appears in the bound. This is because the system is reciprocal along the x-direction, and thus σ_{xx} does not directly contribute to the system nonreciprocity. Maximum isolation will be obtained between states A and B, i.e., between waves travelling along and against the drifting electrons. We denote the wavenumber of such waves as k_{Ay} and k_{Ay}, respectively. Even though nonreciprocity will also appear for waves propagating toward other directions, their nonreciprocal behavior will be weaker and thus such performance will fall within our bound. In a general scenario, the effective nonlocal σ_{yy} conductivity of the metasurface will strongly depend on the properties of the supported waves, which in turn can be manipulated using metal, patterning, and different geometries [24],[25]. An optical metasurface structure could be designed to exploit the platform at their limits, i.e., when $k_{Ay} \to k_0$ and when $k_{By} \to \infty$. In practice, graphene does not support waves with a confinement beyond $300k_0$ due to intrinsic nonlocal effects [26]-[28], thus a

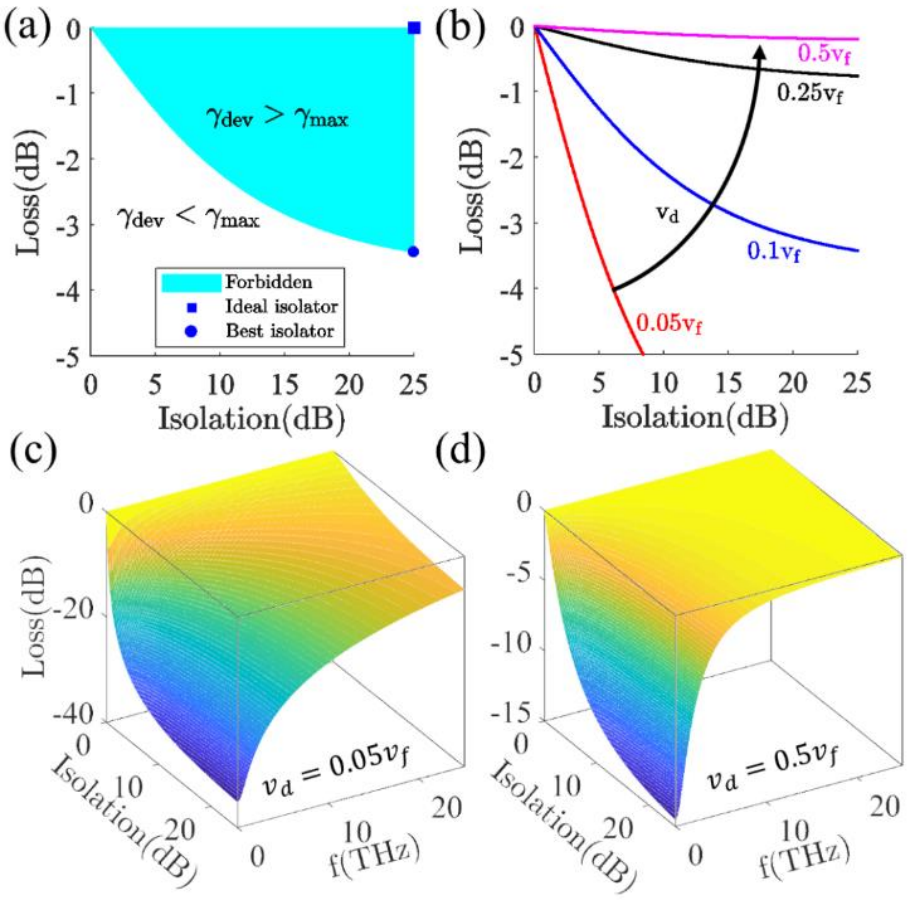

Figure 5.3 Fundamental bounds of drift-biased graphene metasurfaces. (a) Concept of isolation inequality. Any plasmonic device using drift-biased ($v_d = 0.1v_f$) graphene at 21 THz will exhibit a response in terms of loss and isolation within the white area of the panel. Blue area represents device performance that cannot be reached. (b) Isolation inequality for various drift velocities of flowing electrons for a graphene-based metasurface at 21 THz. Panels (c) and (d) show the isolation inequality versus frequency for drift velocities $v_d = 0.05v_f$ and $v_d = 0.5v_f$, respectively. Other parameters are as in Fig. 5.2.

conservative value of $k_{By} \approx 100\ k_0$ is considered here. As a result, $k_{Ay} = k_0$ and $k_{By} = 100\ k_0$ impose the boundaries for the isolation inequality in Eq. 5.9 for an optimal structure.

Fig. 5.3 illustrates the fundamental bounds and optimal device performance obtained by drift-biased graphene-based plasmonic metasurfaces at 21 THz. Panel (a) overviews the isolation-loss plot employed to benchmark the device performance: blue area denotes the forbidden region, associated to a performance that surpass our bound, and white area denotes a performance that can be obtained by realistic metasurfaces. The dark blue circle marks the best performance that can be

obtained with a material. This study is extended in Fig. 5.3(b) for different velocities of the drifting electrons. Results suggest that significant isolation levels, over 25 dB, can be obtained with minimal loss (<1 dB) and moderate drift-bias. The fundamental limits (isolation/loss) of this type of metasurfaces are parametrically explored in Fig. 5.3(c)-(d) for two different drift velocities versus frequency. Results confirm that this type of devices have the potential to exhibit an excellent performance over a broad frequency range. It should be stressed this platform exhibit better performance as frequency increases, and thus it is better suited to operate in the mid-IR band than at low THz frequencies. Additionally, it can be observed that isolation/loss trade-offs significantly improve as the velocity of the drifting electrons increases. The challenge now is to design quasi-optimal plasmonic metasurfaces able to benchmark close to these bounds. In the following, we explore and benchmark the performance of two different platforms: a graphene-sheet employed as a 1D transmission line, a configuration described elsewhere [29],[30] to construct plasmonic devices such as switches or filters, and isotropic and hyperbolic drift-biased metasurfaces [10],[20], [36] excited by a dipole source.

To gain a better understanding of the bounds of drift-biased graphene, we develop a transmission line (TL) [29],[30] composed of three sections of graphene in which only the center one is drift-biased (see Fig. 5.4). This allows to further isolate the response of drift-biased graphene with respect to the excitation. We model this structure in COMSOL Multiphysics [31]. To this purpose, we calculate the drift-biased conductivity of graphene with wavenumbers along and against the drift electrons, and we used them to construct two simulation models: one associated to forward SPP propagation (along the drift) and other for backward SPP propagation (against the drift). We treat the side regions of the structure as ports, and characterize them using lossless, unbiased, graphene. The z-components of the electric field for SPPs travelling in such TL system

are depicted in Fig. 5.4(a). For forward propagation ($+y$ direction, top panel), SPPs travels through the drift-biased section of graphene without significant changes. However, waves propagating against drifting electrons ($-y$ direction, bottom panel) undergo a change in their wavelength together with very significant damping. We quantified this result by calculating the S_{21} and S_{12} coefficients of the system using TL theory [32], which are in good agreement with those found using COMSOL simulations. Fig. 5.4(b)-(d) report a performance study varying the length of the center graphene section of the structure ℓ from 0.3 to 1 μm. As expected, larger sections provide

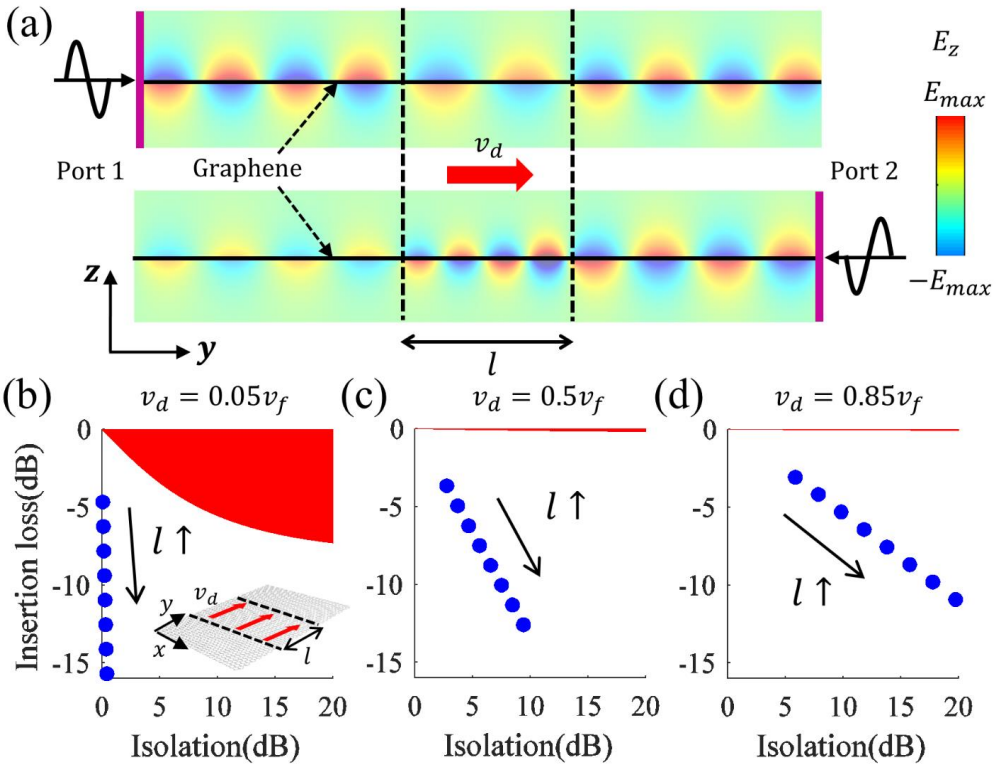

Figure 5.4 Drift-biased graphene as a 1D plasmonic isolator. (a) Numerical simulations in COMSOL Multiphysics. The structure is composed of two plasmonic lossless ports made of pristine graphene and one central graphene region of length $\ell = 0.3\mu m$ that has been drift-biased along the direction indicated by the red arrow ($v_d = 0.5v_f$). Results show SPPs propagation along forward (top) and backward (bottom) directions. (b)-(d) Device performance (loss/isolation) for various drift-velocities at 21 THz (blue dots). The length of the drifted section increases from 0.3 μm to 1 μm in steps of 0.1 μm. Cyan regions show the performance bound provided by the isolation inequality. Other parameters are as in Fig. 5.2.

larger isolation and loss. Increasing the drift-bias further increases the isolation while reducing the loss on the system, leading a trade-off between length and bias to achieve desired responses. However, the performance exhibited by this platform is in all cases well below the upper limits offered by drift-biased graphene. Therefore, we conclude that this platform is far from ideal to achieve quasi optimal nonreciprocal responses.

A realistic approach to excite drift-biased graphene-based plasmonic metasurfaces is to use a dipole located in the near field of the structure. This can be implemented in practice using scanning-type scanning near-field optical microscopy (s-SNOM) by shining laser on a probe tip located above the metasurface [33]-[35]. The tip gets polarized and behaves as a dipole, scattering evanescent fields that couple to the metasurface in the form of SPPs. Here, we explore this excitation approach using a home-made Green's function approach [12] and evaluate its performance and fundamental limits for two specific drift-biased platforms, namely a graphene sheet and a hyperbolic metasurfaces made of graphene ribbons [36].

Fig. 5.5(a) shows the Poynting vector of SPPs excited by a z-directed dipole located 35 nm over a drift-biased graphene sheet for two different drift-velocities ($v_d = 0.5v_F$ and $v_d = 0.85v_F$). Here, drifting electrons are traveling in the $+y$ direction. We focus on nonreciprocity between the dipole located at $\vec{r}_0'$ and an observer point located at $\vec{r}_0$. In this context, isolation is defined as the ratio of the squared modulus of electric fields at source/observation pairs (i.e., $|E(\vec{r}_0, \vec{r}_0')/E(\vec{r}_0', \vec{r}_0)|^2$ [12]) and loss as $\mathrm{Im}(\mathrm{k_y})$. Fig. 5.5(c)-(d) evaluate the performance of this platform along the y-axis (i.e., where maximum isolation occurs) when the distance between source and observation increases from 0.3 to 1 μm with steps of 0.1 μm. Results show a trend similar to the one the found in Fig. 5.4: increasing the drift bias leads to large isolation and lower loss within a somewhat limited range. It should be noted that losses are reduced in this scenario. We attribute

such response to the lack of port sections compared to the TL case, and to the overall better matching between the fields radiated by the dipole and graphene. Still, despite these improvements,

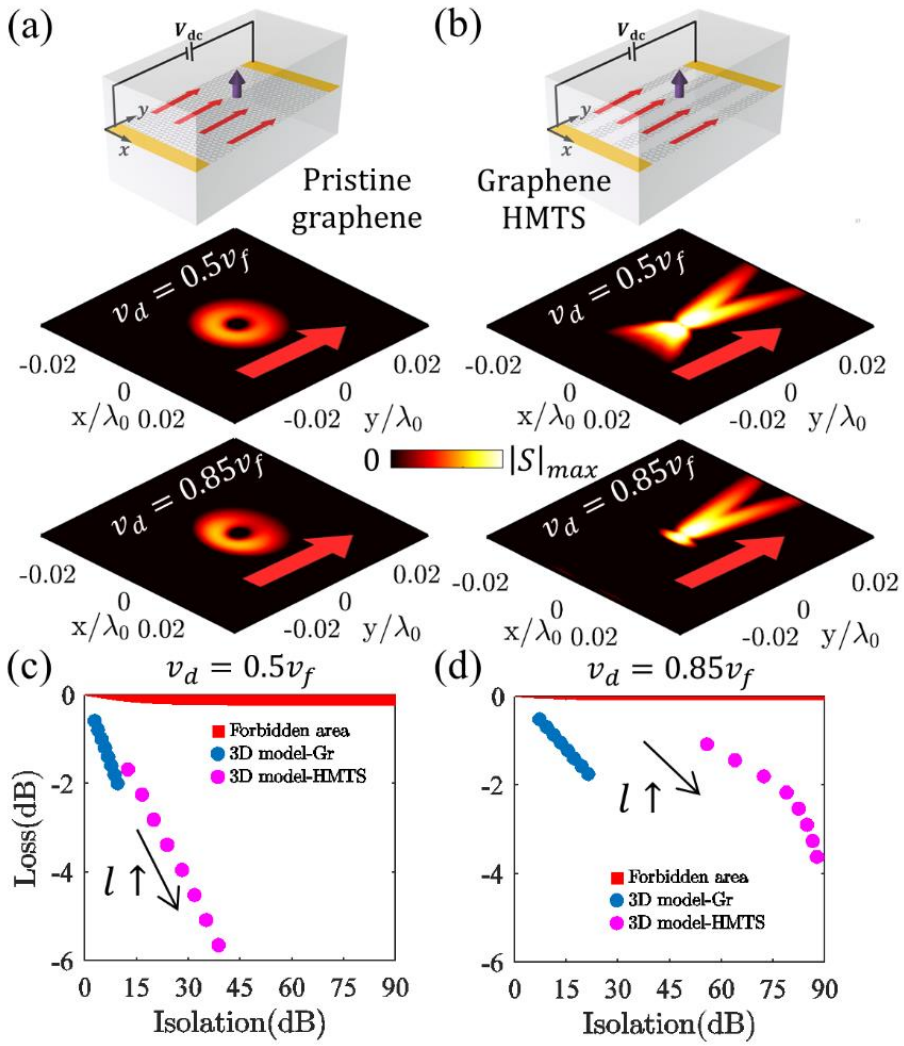

Figure 5.5 Electromagnetic response of drift-biased graphene-metasurfaces excited by a z-directed dipole located $z_0 = 35$ nm. Poynting vector (magnitude) of SPPs excited over a drift-biased graphene sheet (a) and a drift-biased hyperbolic metasurface based on an array of graphene ribbons (b). The width and periodicity of the ribbons is set to W=25 nm and L=50 nm, respectively. Results are plotted for two different drift-velocities: $v_d = 0.5v_f$ (central row) and $v_d = 0.85v_f$ (bottom row). Red arrows show the direction of the flowing electrons. (c) Performance in terms of loss and isolation of the metasurfaces shown above for two different drift-velocities, $v_d = 0.5v_f$ (left) and $v_d = 0.85v_f$ (right). The length of the drifted metasurfaces increases from $0.3\ \mu m$ to $1\ \mu m$ in steps of $0.1\ \mu m$. Cyan regions show the performance bound provided by the isolation inequality. Other parameters are as in Fig. 5.2.

the performance of the platform is far from reaching the fundamental limits offered by drift-biased graphene.

5.4 Application to magnetically-baised graphene plasmonics

Even though many works have explored the interaction of magnetically-biased graphene metasurfaces with plane waves, aiming to construct Faraday rotators [37]-[39] and isolators [40], such structures can also be applied for nonreciprocal plasmonics. For instance, edge-modes propagating on graphene ribbons are nonreciprocal when the structure is combined with metals [41]. However, it is still unclear how optimal such devices are. In general, the vast degrees of freedom to design magnetically-biased graphene metasurfaces make it very challenging to determine if the performance of specific devices is close to the fundamental bounds offered by the material. This usually leads to redundant and time-consuming efforts to marginally increase the device performance by increasing its complexity.

Let us consider a thin arbitrary metasurface that is somehow loaded with magnetically-biased graphene characterized by a conductivity tensor $\underline{\sigma} = (\sigma_d \;\; \sigma_H; \; -\sigma_H \;\; \sigma_d)$, where σ_d and σ_H correspond to graphene's direct and Hall conductivities component. They can be determined using the Kubo formalism [23]. The isolation inequality that determines the fundamental limits of this platform can be analytically derived as

$$\frac{L^2(1-I)^2}{(1-L^2)(I^2-L^2)} \leq \frac{\sigma_H''^2(B_0)\left[\sigma_H'^2(B_0)+\sigma_H''^2(B_0)\right]}{\left[\sigma_d'^2(B_0)-\sigma_H''^2(B_0)\right]^2} = \gamma_{max}, \tag{5.10}$$

where the superscripts $'$ and $''$ denote the real and imaginary parts of the conductivity components, respectively, and B_0 is the magnetic field applied in the direction perpendicular to structure. Similarly to the case studied above, the left-hand side of Eq. 5.10 is related to the performance

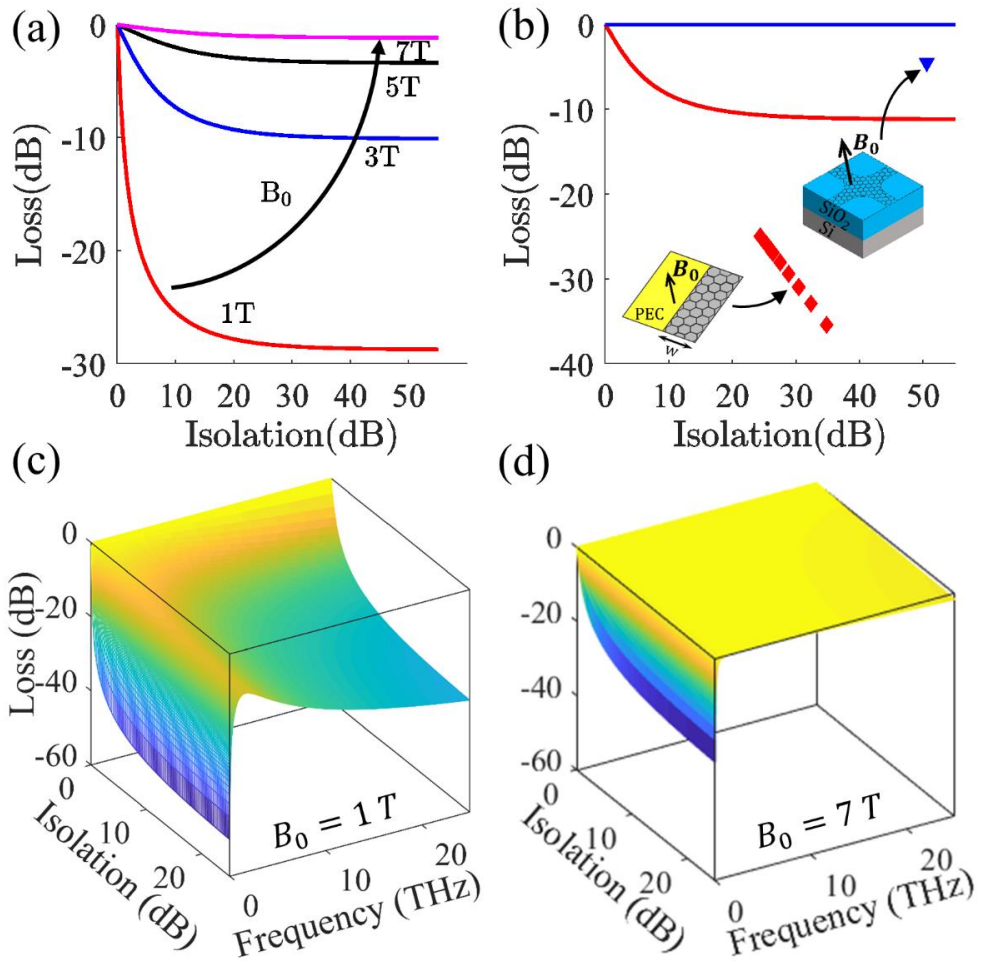

Figure 5.6 Upper bounds of magnetically-biased graphene metasurfaces. (a) Upper bounds for various magnetic field values applied on a given graphene sample at 21 THz. (b) Performance analysis of devices studied in the literature, including nonreciprocal edge modes (red diamonds [41]) and a circulator (blue triangle [42]), versus their upper bounds (solid lines). Insets illustrate the devices schematic. (c)-(d) show the isolation inequality versus frequency for applied magnetic fields $B_0 = 1$ T and $B_0 = 7$ T, respectively. Other parameters are as in Fig. 5.3.

(isolation/loss) of a specific plasmonic device whereas the right-hand side provides the upper performance (γ_{max}). Nonreciprocity is here governed by the Hall conductivity of graphene, and the bound reduces to zero in case that the metasurfaces are not magnetically biased, i.e., $\sigma_H \to 0$ forces that $\gamma_{max} \to 0$.

Fig. 5.6(a) shows the upper bounds (isolation/loss) of magnetically-biased graphene-based metasurfaces at 21 THz versus the applied magnetic field. Results show that large isolation may

be achieved with bias as little as 1 T but at the expense of significant loss. Upper performances are significantly improved when larger magnetic bias values are applied. Note that the graphene parameters employed in this panel are identical to those employed in Fig. 5.3 (b), which allows us to directly compare the performance of drift- and magnetically- biased plasmonic metasurfaces. Fig. 5.6(b) benchmarks the response of nonreciprocal platforms explored in the literature against the fundamental limits obtained using Eq. 5.10. Specifically, red data is associated to a nonreciprocal plasmonic system composed of a graphene ribbon that is short-circuited on one edge with a metal plane [41] (see inset). In the system, the ribbon has a width of 100 μm, $B_0 = 1$ T, frequency is set to 2 THz, and graphene's chemical potential and relaxation time are set to 0.37 eV and 0.1 ps, respectively. Nonreciprocal edge plasmons appears on the graphene edge that interfaces with air. The response of the platform is explored changing the length of the graphene ribbon from 0.3 μm to 1 μm with a step of 0.1 μm (red diamonds). Even though the system provides large isolation, it exhibits quite significant loss and benchmarks quite far from the fundamental limits of the material. The other platform considered here is related to the magnetically-biased graphene circulator described in Ref. [42]. It is composed of a cross-shaped graphene pattern (see inset) printed on top of a SiO_2/Si substrate and operates at 3.4 THz. The applied bias is set to $B_0 = 1.5$ T and graphene's chemical potential and relaxation time are set to 0.15 eV and 0.9 ps, respectively. The blue triangle marker displays the performance of the device, which provides significant isolation (~ 50 dB) and moderate loss (~ 5 dB). Even though such performance is remarkable, there is still plenty of room to improve it and bringer close to the upper bounds offered by the magnetically-biased graphene employed in the system.

Fig. 5.6(c)-(d) further explores the fundamental limits of magnetically-biased graphene as a function of frequency for two magnetic bias, $B_0 = 1$ T and $B_0 = 7$ T. Results show that high

performance in terms of isolation/loss can be obtained in the THz band (roughly from ~1 to ~ 5 THz) using moderate bias fields. As frequency increases, the performance significantly degrades, and high isolation is always associated with large loss. Further enhancing the magnetic field to $B_0 = 7$ T allows to construct metasurfaces with excellent trade off in terms of isolation and loss over a large frequency band.

5.5 Conclusions

In conclusion, we have explored the fundamental limits of nonreciprocal metasurfaces that guide surface waves. Remarkably, these limits are only related to the properties of the nonreciprocal material employed within the device and do not depend on the presence of other materials such as metals or dielectrics or on geometrical considerations. Without loss of generality, we focused on two types of nonreciprocal plasmonic platforms, i.e., drift- and magnetically- biased graphene metasurfaces, and we analytically derived their fundamental bounds. In the case of drift-biased devices, we explored 1D devices excited by surface plasmons using both transmission line theory and full-wave numerical simulations (COMSOL Multiphysics). Additionally, we investigated isotropic and hyperbolic drift-biased metasurfaces excited by electrical dipoles located in the near field of the device – a configuration that mimics s-SNOM microscopy. Our results show that most devices operate relatively far from their upper bounds, and thus their performance can be significantly improved. One important exception is the case of drift-biased hyperbolic metasurfaces, which exhibit an outstanding performance at frequencies close to the mid infrared band. Overall, drift-biased graphene plasmonics is an emerging and promising broadband technology compatible with integrated circuits. In the case of magnetically-biased graphene metasurfaces, we evaluated the performance of several devices studied in the literature – namely an isolator based on nonreciprocal edge modes and a circulator based on patterned graphene – and

benchmarked their response against the upper bounds. Even though these devices exhibit very interesting responses, they all operate relatively far from the upper bound and thus their performance can be further improved. Additionally, our bounds revealed that magnetically-biased graphene metasurfaces are well-suited (in terms of isolation/loss trade-offs) to operate in the low terahertz band. Recently, circular dichroism has been demonstrated to be an efficient tool to break reciprocity in 2D materials due to the optically-driven non-degenerate valleys [43]-[45]. As another nonreciprocal plasmonic platform and armed with a similar optical conductivity tensor to that of magnetically-biased graphene, optically-driven 2D materials can also be evaluated though our bounds.

Moving beyond, our bounds can be applied to explore the fundamental limits of many other nonreciprocal plasmonic metasurfaces, including those based on magneto-optic materials [46] and 2D materials such as transition metal dichalcogenide monolayers [47]. We envision that the bounds derived here will be useful in the development of quasi-optimal nonreciprocal metasurfaces employed in areas such as communication, sensing, imaging, and nonlinear optics, among many others.

5.6 Chapter references

[1] Schaug-Pettersen, T., and A. Tonning. "On the optimum performance of variable and nonreciprocal networks." *IRE Transactions on Circuit Theory* 6.2 (1959): 150-158.

[2] Vakil, Ashkan, and Nader Engheta. "Transformation optics using graphene." *Science* 332.6035 (2011): 1291-1294.

[3] Zhao, Dan, et al. "Tunable On-Chip Terahertz Isolator Based on Nonreciprocal Transverse Edge Spin State of Asymmetric Magneto-Plasmonic Waveguide." *Laser & Photonics Reviews* 17.2 (2023): 2200509.

[4] Hassani Gangaraj, S. Ali, et al. "Enhanced nonlinear optical effects in drift-biased nonreciprocal graphene plasmonics." *ACS Photonics* 10.11 (2023): 3858-3865.

[5] Hassani Gangaraj, S. Ali, et al. "Enhanced nonlinear optical effects in drift-biased nonreciprocal graphene plasmonics." *ACS Photonics* 10.11 (2023): 3858-3865.

[6] Tamagnone, Michele, et al. "Fundamental limits and near-optimal design of graphene modulators and non-reciprocal devices." *Nature photonics* 8.7 (2014): 556-563.

[7] Hanson, George W. "Dyadic Green's functions for an anisotropic, non-local model of biased graphene." *IEEE Transactions on antennas and propagation* 56.3 (2008): 747-757.

[8] Lovat, Giampiero, et al. "Non-local models and effects in graphene nanointerconnects." *2013 International Symposium on Electromagnetic Compatibility*. IEEE, 2013.

[9] Correas-Serrano, D., et al. "Black phosphorus plasmonics: anisotropic elliptical propagation and nonlocality-induced canalization." *Journal of Optics* 18.10 (2016): 104006.

[10] Zhao, Wenyu, et al. "Efficient Fizeau drag from Dirac electrons in monolayer graphene." *Nature* 594.7864 (2021): 517-521.

[11] Morgado, Tiago A., and Mário G. Silveirinha. "Directional dependence of the plasmonic gain and nonreciprocity in drift-current biased graphene." *Nanophotonics* 11.21 (2022): 4929-4936.

[12] Correas-Serrano, D., and J. S. Gomez-Diaz. "Nonreciprocal and collimated surface plasmons in drift-biased graphene metasurfaces." *Physical Review B* 100.8 (2019): 081410.

[13] Chang, You-Chia, et al. "Realization of mid-infrared graphene hyperbolic metamaterials." *Nature communications* 7.1 (2016): 10568.

[14] Morgado, Tiago A., and Mário G. Silveirinha. "Drift-induced unidirectional graphene plasmons." *ACS photonics* 5.11 (2018): 4253-4258.

[15] Morgado, Tiago A., and Mário G. Silveirinha. "Drift-induced Nonreciprocal Graphene Plasmonics." *2019 PhotonIcs & Electromagnetics Research Symposium-Spring (PIERS-Spring)*. IEEE, 2019.

[16] Hassani Gangaraj, S. Ali, and Francesco Monticone. "Drifting electrons: Nonreciprocal plasmonics and thermal photonics." *ACS photonics* 9.3 (2022): 806-819.

[17] Paul, N. K., and J. S. Gomez-Diaz. "Broadband and unidirectional plasmonic hyperlensing in drift-biased graphene." *Applied Physics Letters* 118.9 (2021).

[18] Morgado, Tiago A., and Mário G. Silveirinha. "Negative Landau damping in bilayer graphene." *Physical review letters* 119.13 (2017): 133901.

[19] Morgado, Tiago A., and Mário G. Silveirinha. "Nonlocal effects and enhanced nonreciprocity in current-driven graphene systems." *Physical Review B* 102.7 (2020): 075102.

[20] Dong, Yinan, et al. "Fizeau drag in graphene plasmonics." *Nature* 594.7864 (2021): 513-516.

[21] Navajas, David, et al. "Addressing the Impact of Surface Roughness on Epsilon-Near-Zero Silicon Carbide Substrates." *ACS photonics* 10.9 (2023): 3105-3114.

[22] Pérez-Escudero, José M., et al. "Silicon carbide as a material-based high-impedance surface for enhanced absorption within ultra-thin metallic films." *Optics Express* 28.21 (2020): 31624-31636.

[23] Hanson, George W. "Dyadic Green's functions and guided surface waves for a surface conductivity model of graphene." *Journal of Applied Physics* 103.6 (2008).

[24] Li, Guixin, Shuang Zhang, and Thomas Zentgraf. "Nonlinear photonic metasurfaces." *Nature Reviews Materials* 2.5 (2017): 1-14.

[25] Meinzer, Nina, William L. Barnes, and Ian R. Hooper. "Plasmonic meta-atoms and metasurfaces." *Nature photonics* 8.12 (2014): 889-898.

[26] Correas-Serrano, Diego, et al. "Spatially dispersive graphene single and parallel plate waveguides: Analysis and circuit model." *IEEE Transactions on Microwave Theory and Techniques* 61.12 (2013): 4333-4344.

[27] Lovat, Giampiero, et al. "Semiclassical spatially dispersive intraband conductivity tensor and quantum capacitance of graphene." *Physical Review B* 87.11 (2013): 115429.

[28] Correas-Serrano, D., et al. "Nonlocal response of hyperbolic metasurfaces." *Optics Express* 23.23 (2015): 29434-29448.

[29] Gómez-Díaz, Juan-Sebastian, and Julien Perruisseau-Carrier. "Graphene-based plasmonic switches at near infrared frequencies." *Optics express* 21.13 (2013): 15490-15504.

[30] Correas-Serrano, Diego, et al. "Graphene-based plasmonic tunable low-pass filters in the terahertz band." *IEEE Transactions on Nanotechnology* 13.6 (2014): 1145-1153.

[31] "COMSOL Multiphysics Reference Manual, version 6.0", COMSOL, Inc, www.comsol.com .

[32] Pozar, David M. *Microwave engineering*. John wiley & sons, 2011.

[33] Gerber, Justin A., et al. "Phase-resolved surface plasmon interferometry of graphene." *Physical review letters* 113.5 (2014): 055502.

[34] Alonso-González, Pablo, et al. "Acoustic terahertz graphene plasmons revealed by photocurrent nanoscopy." *Nature nanotechnology* 12.1 (2017): 31-35.

[35] Chen, Jianing, et al. "Optical nano-imaging of gate-tunable graphene plasmons." *Nature* 487.7405 (2012): 77-81.

[36] Gomez-Diaz, J. S., and Andrea Alu. "Flatland optics with hyperbolic metasurfaces." *ACS Photonics* 3.12 (2016): 2211-2224.

[37] Crassee, Iris, et al. "Giant Faraday rotation in single-and multilayer graphene." *Nature Physics* 7.1 (2011): 48-51.

[38] Poumirol, Jean-Marie, et al. "Electrically controlled terahertz magneto-optical phenomena in continuous and patterned graphene." *Nature communications* 8.1 (2017): 14626.

[39] Tamagnone, Michele, et al. "Magnetoplasmonic enhancement of Faraday rotation in patterned graphene metasurfaces." *Physical Review B* 97.24 (2018): 241410.

[40] Tamagnone, Michele, et al. "Near optimal graphene terahertz non-reciprocal isolator." *Nature communications* 7.1 (2016): 11216.

[41] Sounas, Dimitrios L., and Christophe Caloz. "Edge surface modes in magnetically biased chemically doped graphene strips." *Applied Physics Letters* 99.23 (2011): 231902.

[42] Dmitriev, Victor, and Samara L. Matos da Silva. "Ultra wideband THz graphene four-port circulators." *Microwave and Optical Technology Letters* 62.1 (2020): 112-117.

[43] Schaibley, John R., et al. "Valleytronics in 2D materials." *Nature Reviews Materials* 1.11 (2016): 1-15.

[44] Cao, Ting, et al. "Valley-selective circular dichroism of monolayer molybdenum disulphide." *Nature communications* 3.1 (2012): 887.

[45] Yin, Jianbo, et al. "Tunable and giant valley-selective Hall effect in gapped bilayer graphene." *Science* 375.6587 (2022): 1398-1402.

[46] Zayets, Vadym, et al. "Optical isolator utilizing surface plasmons." *Materials* 5.5 (2012): 857-871.

[47] Klein, Matthew, et al. "2D semiconductor nonlinear plasmonic modulators." *Nature communications* 10.1 (2019): 3264.

6. Conclusions

In this thesis, I have proposed a novel approach to achieve magnetless nonreciprocity in graphene combining the utilization of both optical pump and strain engineering. I specifically reviewed the method to calculate the Hall conductivity of graphene under circularly polarized light, the optical conductivity under uniform strain fields and ways to generate uniform pseudomagnetic fields using non-uniform strain fields. The process to incorporate optical pump and strain fields into the Bloch equations is derived in detail. The second part of this thesis has dealt with finding the fundamental limits of nonreciprocal plasmonic metasurfaces. I have specifically benchmarked several platforms including drift current- and magnetically- baised graphene under their corresponding bounds and demonstrated that the drift-biased hyperbolic graphene metasurface is a superior platform as compared to the normal drift-biased graphene metasurface. The key findings of each chapters are briefly summarized below:

In Chapter 2, I have reviewed the formulism to calculate the optical conductivity for pristine graphene, graphene under magnetic field and optical pump. I have then calculated the optical conductivity of gapped graphene when it is optically pumped with circularly-polarized waves and demonstrate the current efforts towards achieving nonreciprocity at THz and IR frequencies.

In Chapter 3, I have applied the same tight-binding approach on graphene under uniform strain fields. I have calculated the optical conductivity of graphene under different types of strain and magnitude. Results show that the diagonal conductivity terms change differently among four types of strain, but the net Hall conductivity always vanishes. The critical point is that the uniform strain exerted on graphene does not break reciprocity. When it moves to non-uniform strain, there can be numerous types of strategy to generate pseudomagnetic field in the two non-degenerate valleys of graphene and within the methods I have reviewed the maximum pseudomagnetic can

come to close ~100 Teslas. Then, I have proposed strategies to unleash large non-reciprocal response in graphene combining strain engineering and external magnetic fields or optical pumps.

In Chapter 4, I have used the knowledge gained from Chapter 2 and 3 and to propose a new method to realize magnet-free nonreciprocity in graphene combining the use of strain engineering and CP light pump. I have fully reviewed the formalism and algorithms that are required to evaluate the carrier dynamics and population on discrete energy levels under the influence of external electromagnetic fields while taking into account the relaxation due to Coulomb scattering. The effect of non-uniform strain is incorporated into the Bloch equation by assuming a reasonable pseudomagnetic field with opposite signs in the two valleys of graphene with the insight we have gained from Chapter 3. The results show the population imbalance in the two non-degenerate valleys in graphene which indicates the broken reciprocity. Successful development and validation of these innovative concepts will lead to a new generation of integrated isolators and devices for non-reciprocal wave steering and manipulation compatible with existing plasmonic and photonic technology.

In Chapter 5, I have explored the fundamental limits of nonreciprocal metasurfaces that guide surface waves. Remarkably, these limits are only related to the properties of the nonreciprocal material employed within the device and do not depend on the presence of other materials such as metals or dielectrics or on geometrical considerations. Without loss of generality, we focused on two types of nonreciprocal plasmonic platforms, i.e., drift- and magnetically- biased graphene metasurfaces, and we analytically derived their fundamental bounds. Our results show that most devices operate relatively far from their upper bounds, and thus their performance can be significantly improved. One important exception is the case of drift-biased hyperbolic graphene metasurfaces, which exhibit an outstanding performance at frequencies close to the mid infrared

band. Overall, drift-biased graphene plasmonics is an emerging and promising broadband technology compatible with integrated circuits.

The theoretical framework we have built can be employed in evaluating a broader range of nonreciprocal metasurfaces not limited to those based on traditional magneto-optic materials [1] but also what has recently become very popular, like optically-pumped transition metal dichalcogenide monolayers [2]. The foundational limits derived in this work have the potential to advance the development of near-optimal nonreciprocal metasurfaces, which are utilized in various fields including communication, sensing, imaging, and nonlinear optics, among others.

Chapter references

[1] Zayets, Vadym, et al. "Optical isolator utilizing surface plasmons." *Materials* 5.5 (2012): 857-871.

[2] Klein, Matthew, et al. "2D semiconductor nonlinear plasmonic modulators." *Nature communications* 10.1 (2019): 3264.